Hasselt University
Institute for Materials Research
Diepenbeek, Belgium

Development and study of diamond architectures for biosensing applications

by

Grieten Lars

Promotor: Prof. Dr. P. Wagner
Co-promotor: Prof. Dr. L. Michiels

This thesis is submitted for the degree of Doctor in de Wetenschappen
2012

universiteit hasselt
INSTITUUT VOOR
MATERIAALONDERZOEK

Chairman:	Prof. Dr. J. Manca Dean Faculty of Science UHasselt
Supervisor:	Prof. Dr. P. Wagner UHasselt
Co-supervisors:	Prof. Dr. L. Michiels UHasselt
Members of the jury:	M. Ameloot UHasselt XXXXXXXXXXXXXX XXXXXXXXXXXXXX

Contents

Abbreviations

Ab	Antibody
Ag	Antigen
Al	Aluminum
Au	Gold
Bp	Base pair
CRP	C-Reactive Protein
CNF	Carbon nanoflakes
CNT	Carbon nanotubes
CNW	Carbon nanowalls
CVD	Chemical vapor deposition
CV	Cyclic Voltammetry
Da	Dalton or g/mol
DNA	Deoxyribonucleic acid
DND	Detonation nanodiamonds
EDC	1-ethyl-3-(3-dimethylaminopropyl)-carbodiimide
EIS	Electrochemical Impedance Spectroscopy
ELISA	Enzyme linked immunosorbent assay
$\triangle E_p$	Peak separation
H-NCD	Hydrogen terminated nanocrystalline diamond
HOPG	Highly oriented pyrolytic graphite
IgG	Immunoglobulin G
i_{PA}	Anodic peak
i_{PC}	Cathodic peak

LMW	Low molecular weight molecules
MES	2-[N-morpholino]-ethanesulphonic acid
MWPECVD	Micro wave plasma enhanced chemical vapor deposition
MES	2-(N-morpholino)ethanesulfonic acid
NCD	Nanocrystalline diamond
NCD:H	Hydrogen terminated nanocrystalline diamond
NCD:O	Oxygen terminated nanocrystalline diamond
OWRK	Owens Wendt Raeble and Kaeble
PBS	Phosphate Buffer Saline solution
Pd	Palladium
Pt	Platinum
RIA	Radio immunoassay
SAM	Self-assembled monolayer
SE	Surface energy
SFE	Surface Free Energy
SNP	Single nucleotide polymorphism
ssDNA	Single-stranded deoxyribonucleic acid
Ti	Titanium
TRIS	tris(hydroxymethyl)aminomethane
UDD	Ultra dispersed diamonds
XPS	X-ray Photoelectron Spectroscopy
Symbols: γ	Surface energy
γ_{sg}	solid/gas surface energy
γ_{sl}	solid/liquid surface energy
γ_{lg}	liquid/gas surface energy

Chapter 1

Introduction and background

1.1 With 3000 publications a year, and still growing, biosensors cannot be ignored

Back in the 50's, when TV's only had black and white screens, science took its leap forward. Watson and Crick unraveled the structure of the DNA helix, polio was cured, NASA was founded and Leland Clark discovered the Clark electrode which allowed real-time oxygen monitoring in patients [1]. All of these discoveries were the inspiration and driving engine for new technologies. Nobody ever suspected in the beginning years of semiconductors and the first electronic devices, that they would also play an important role in the everyday human life. Now, electronics are available everywhere, from power and logic devices for communications, to computers for work, entertainment and safety. When electronics become more accessible, they can provide the backbone for healthcare applications for everyday by everyone [2].

Up till now, silicon is the material that gets all the glory. However, the limits of the material have already been reached, and new material systems are needed to provide suitable platforms for power electronics or biochemistry. For these reasons, science is seeking for new materials, which would open novel possibilities and would model new standards. Among the new materials currently under study, diamond is certainly one of the most exotic and hopeful resources. When "non-science" people ask: "What is your research topic?", and I say: "I try to develop biosensors on diamond!", their eyes start to sparkle like real diamonds and they do not understand why diamond? Diamond possesses unique properties, which have attracted the interest of both women and scientists. Research in diamond spreads from mechanics (with tool coating) through electronics (with micro-electromechanical- and electronics devices) to biochemistry/biosensing (with electrochemical and biochemical sensors). Again, when the ’non-science’ people ask: How do you get the diamond? and I say "well, you can grow it in a microwave", they are again puzzled by the idea.

For electronic applications, the use of synthetic diamond is not completely established and does not yet match the requirements needed, but for electro chemistry it is gaining field everyday! To make a contribution to the science for diamond applications in healthcare, we focus in this dissertation on the combination of synthetic diamond with components of the human immune system to develop and understand the possibilities for a diamond based biosensor platform for cardiovascular risk assessment markers.

1.2 Biosensors

A biosensor is defined as a device incorporating a biological **recognition component** such as an antibody (Ab), a receptor protein, an enzyme, a cell, single stranded DNA or even tissue, connected to a **transducing element**, which translates binding/recognition events between the analyte and the recognition element into a **signal** that is proportional to the concentration of the **analyte** being sensed (Figure 1.1) [3, 4].
The class of biosensors that is most growing involves the affinity-based biosensors, which are defined as devices incorporating biological receptor molecules that can reversibly detect receptor-ligand interactions with a high differential selectivity and in a non-destructive fashion. Only biosensors based on a bio-affinity element such as an antibody, a receptor pro-

tein, a DNA molecule and since recent aptamers are covered by this description [3, 5]. The most popular and standardized sensing system is the enzyme linked immunosorbent assays (ELISA). These biosensors are employed within healthcare, environmental, food and drug testing. These assays are often complex, require multicomponents and multistep assay configurations. The new generation biosensors have the potential to make assays that are inherently complex and time-consuming, more rapid, versatile, cost-effective and accessible for a wide range of applications. As mentioned before there are a number of structural and design features necessary that determine the typical characteristic of a certain biosensor. These properties are shown in Table 1.1.

Table 1.1: Overview of the main characteristics of a biosensor.

Structural/design considerations	Various types
Assay format	Direct vs indirect, Assay time, Reversibility
Bio-affinity element	Natural or synthetic receptors
Transducer and read-out	Optical, electrical, Gravimetric,...
Analyte	Proteins, Low molecular weight molecules (LMW), Deoxyribonucleic acid (DNA),...

In this work we have chosen for a direct assay with natural receptors, antibodies, immobilized on a nanocrystalline diamond transducer that allows an optical and electronical readout. The target of interest is a cardiovascular risk assesment protein: C-reactive protein (CRP). In the following sections we will discuss each element of the immunosensor of interest in this thesis.

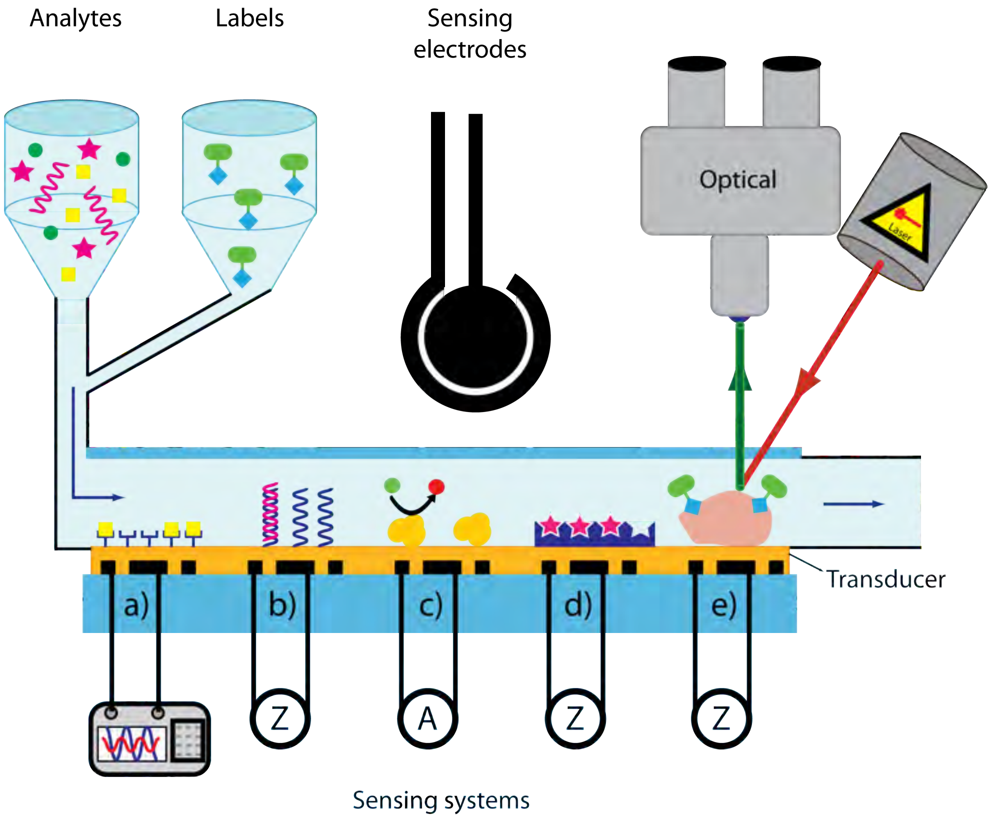

Figure 1.1: Cartoon of a typical biosensing principle. A biosensor detects analytes, this can be done by different receptors such as (a) antibodies, (b) DNA, (c) enzymes, (d) molecular imprinted polymers, (e) cells. The read-out technique is most of the time electrical (impedimetric, amperometric,...) or optical (microscopy, colorimetry,...) and the signal is allowed to transfer via a transducer layer. (Image contribution to Cahier Mens 2.0)

1.3 Analyte

A broad variety of substances exist that require analysis to diagnose/assess a certain patient/product/situation. Food- and environmental agencies and authorities are interested in low molecular weight molecules such as histamine (canned fish decay), herbicides, pesticides, drugs (caffeine, tetrahydrocannabinol (Cannabis), benzoylmethylecgonine (cocaine), etc...). Gene and forensic research require rapid assessment and screening of DNA/RNA. Healthcare is more interested in certain protein markers in patients samples. Current techniques require at least half a day to detect and quantify the concentration. Of course time is a luxury physicians do not have, thus rapid screening is key and essential to proper diagnosis. The analyte of interest in this research is C-reactive protein (CRP). The structure, properties, phylogeny and incidence will be discussed in the following sections.

1.3.1 C-Reactive Protein

C-reactive protein was discovered in 1930 by Tillet and Francis. They found the presence of a certain protein in patients who responded to the C polysaccharide of pneumococcus. It was only afterwards they realized that CRP was not a foreign secreted protein, but was synthesized in hepatic cells [6, 7].

1.3.2 Structure and phylogeny

The CRP gene is located on the first chromosome (1q21-q23). The human CRP molecule (115 kDa) (Dalton is g/mol) is composed out of five identical non-glycosylated polypeptide subunits (±23 kDa), each containing 206 amino acid residues. It belongs to the pentraxin family of calcium-dependent ligand-binding plasma proteins. The protomers are non-covalently associated in an annular configuration with cyclic pentameric symmetry (see Figure 1.2).

1.3.3 (Patho)physiology

C-reactive protein belongs to the acute phase proteins. They develop in a wide range of acute and chronic inflammatory conditions. During in-

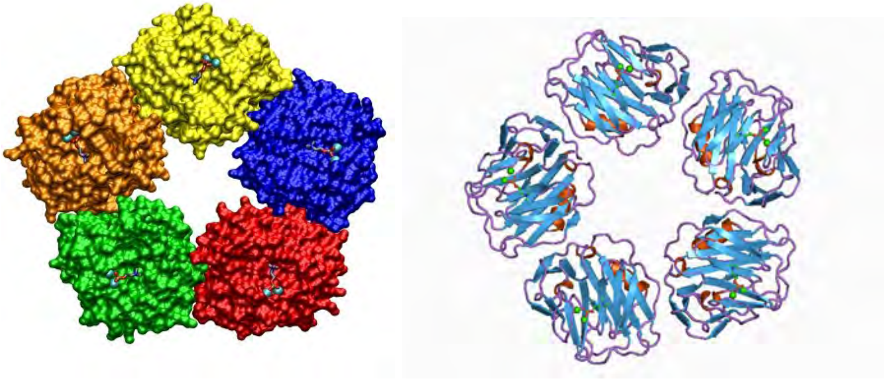
(a) (b)

Figure 1.2: (a) Space filling model of a CRP protein and (b) the same structure shown in a ribbon diagram (source of (a) and (b): [8]).

flammation, various cytokines are secreted, amongst which IL-6, which triggers CRP synthesis in hepatic cells [9, 7]. In the acute phase, CRP increases rapidly of the acute insult (within 2 hours), reaching a peak in 48 hours. Such a rapid increase of CRP occur when inflammation, infection, trauma and tissue necrosis, malignancies, and autoimmune disorders arise. Because there is a large number of disparate conditions that can increase CRP production, an elevated CRP level does not diagnose a specific disease but only provides support for the presence of an inflammatory disease [6].

Plasma CRP is produced only by hepatocytes. The hepatic synthesis starts very rapidly after a single stimulus, serum concentrations rising above 5 μg/ml by about 6 hours and peaking around 48 hours. The plasma half-life of CRP is about 19 hours and is constant under all conditions of health and disease, so that the sole determinant of circulating CRP concentration is the synthesis rate, which thus directly reflects the intensity of the pathological process(es) stimulating CRP production.

1.3.4 CRP and cardiovascular disease

There is a prognostic association between increased CRP production and outcome after acute myocardial infarction [10] and in acute coronary syndromes. In the mid 1990’s research revealed that the presence of CRP in plasma became an indicator for future atherothrombotic events, including coronary events, stroke, and progression of peripheral arterial disease [11, 12, 13]. These findings triggered widespread interest, especially because clinical use of CRP measurements had been largely ignored for about 30 years. However, CRP values can never be diagnostic on their own and can only be interpreted at the bedside, in full knowledge of all other clinical and pathological results. CRP is also an interesting parameter for continuous monitoring next to blood pressure and heart rate. Other acute-phase proteins include protease inhibitors and coagulation, complement, and transport proteins. However, the only molecule that displays sensitivity, response speed, and dynamic range comparable to those of CRP is serum amyloid A protein. In healthy young adult volunteer blood donors, the median concentration for CRP is 0.8 μg/ml, the 90th centile is 3.0 μg/ml, and the 99th centile is 10 μg/ml (depending on the age) [14]. In case of mild inflammation the concentration increases up to 10-40 μg/ml, during active inflammationm it raises up to 40-200 μg/ml, whilst during severe inflammation, levels can reach up to 500 μg/ml [12, 13].

1.4 Recognition layer

The classification of a biosensor is based on the receptor layer which is chosen. The layer may consist of enzymes, antibodies, nucleic acids, synthetic receptors or living organisms such as cells. These receptors bind with great affinity and specificity to their analyte as is shown in Figure 1.1.

1.4.1 Immunosensors senses with antibodies

The human body is able to produce more than 10^8 distinct antibodies. These range over specific classes and subclasses. The immunoglobulins have 5 members in their superfamily i.e. Immunoglobulin G (IgG), IgA, IgM, IgD, IgE with each member specified according to their heavy chain type [15]. Within the subclass of IgG there are very similar heavy chain constant region amino acid sequences with only small variations. Another aspect of antibodies is their mono- or polyclonal nature which is briefly discussed in Table 1.2. Further we will only focus on the IgG's because it is the most relevant to this work.

ImmunoglobulinG consist of hundreds of individual amino acids arranged in a highly ordered sequence. These polypeptides are produced by the immune system cells (B-lymphocytes) when exposed to an antigenic substance. Antibodies contain in their structure 2 binding sites for a specific molecular structure of the antigen. Each binding site interacts in a highly specific way with its unique antigen. The interaction is based on electrostatic forces, hydrogen bonding, hydrophobic and Van der Waals interactions. This feature is the key to many immuno-chemical techniques and thus also to immunosensors. The advantage of antibodies is that they can be synthesized against a broad range of antigens, ranging from large macromolecular proteins to small, low molecular weight molecules [15, 16, 17]. In addition, antibodies have homogeneity in their structure, which allows standardization of procedures such as immobilization of the receptor molecules onto the biosensor surface.

However, antibodies also have their drawbacks and limitations. The production and screening of Ab's is time consuming and expensive. Also the detection of an antigen withholds no intrinsic catalytic activity that could amplify a signal (such as with enzymes), this means that a single antibody can detect only up to two antigens (Ag's). Because antibodies are biological structures that undergo a very specific protein folding that results in 'the quaternary structure'. This makes them very susceptible for small environmental changes that could lead to (partially) loss of their specific folding pattern and therefore resulting in the loss of their unique binding capabilities. Such changes can be due to slight alterations in temperature, ionic concentration, pH, solvent,... . Finally, the strong interaction of the Ab-Ag complex limits its use since it makes the regeneration of sensor systems troublesome [18].

Table 1.2: Overview of the main differences between mono- and polyclonal antibodies.

Polyclonal	Monoclonal
Inexpensive	Expensive
Immunization synthesis	Single cell line synthesis
Short synthesis time	Long synthesis time
Multiple epitopes of antigen	One epitope of antigen

1.4.2 Structure of antibodies and antibody fragments

Antibodies are glycoproteins with a molecular mass of about 150.000 Da consisting of 2 identical heavy (H) and two identical light (L) chains, linked together by disulfide bonds. Actually each chain of an antibody can be divided into domains. The amino-terminal domains of the heavy and the light chains are highly variable (the F_V region in Figure 1.3 (a)). Thus, the light chain consists of one variable domain (V_L and one carboxyl-terminal constant domain (C_L), and the heavy chain consists of one variable (V_H) and three or four constant domains ($C_{1,2,3}$). Together, the variable domains form the antigen binding sites.

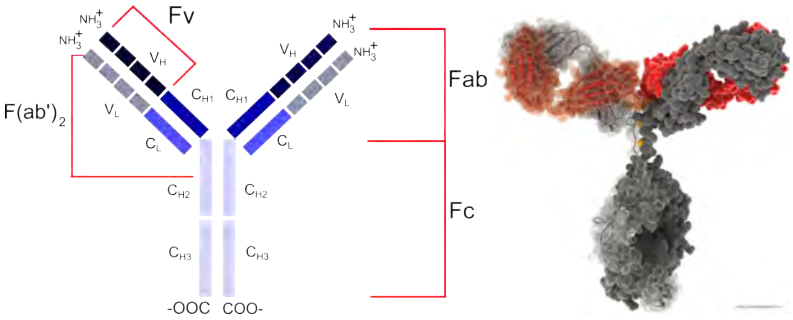

(a) (b)

Figure 1.3: (a) Schematic representation of an IgG protein and the possible fragments that can be used as bio-affinity elements to devise immunosensors. (b) Space filling/ribbon diagram of the IgG molecule. (Source (b): [19])

Besides full size antibodies, other affinity binding parts can exist. Four other types of antigen-binding antibody fragments are also interesting as bio-affinity elements for immunosensors: the F(ab')$_2$ fragment, the Fab', Fab and single-chain Fv fragment.

1.4.3 Antigen-antibody systems used in this thesis

The choice of the antibody-antigen system for immunosensor development is mainly determined by the actual application of the sensor. In this work a monoclonal mouse anti CRP antibody was used for the detection of the CRP antigen with the application in the field of healthcare diagnostics. Besides the anti-CRP antibody other antibodies were used for characterization. A polyclonal Goat anti-mouse antibody labeled with an Alexa-488 (or 555) fluorophore served as a fluorescent tracer. For impedance sensing also a colloidal-gold (5 or 40 nm) labeled antibody was used.

1.5 Transducer

Synthetic diamond is used as a transducer material for the immunosensor. This is not only a good material which allows optical measurements but can also be used in electrochemical measurements when it is doped. The following sections will give a brief overview in the world of diamond and its possibilities.

1.5.1 Diamond: just carbon

Carbon (C) is the backbone of all organic material. It has three isotopes that occur naturally: C^{12}, C^{13}, and the radioactive C^{14}. The carbon atom has 6 electrons which can be placed in its atomic orbitals. The main bonding types of carbon are sp^2 or sp^3 hybridization. When carbon binds to only three neighboring atoms it forms the sp^2 bonds which consist of three σ bonds in a plane distributed evenly with 120° angles between them and a π bond which is delocalised and can switch as a double bond between the three existing σ-bonds. The diamond unit cell consists of sp^3 hybridized carbon atoms. In this case carbon binds to four neighboring atoms. The four orbitals of one carbon atom take as much space as possible which results in the formation of a tetrahedron. Each orbital points towards one corner of the tetrahedron and the positive carbon core is placed in the center.

Carbon can appear in various allotropes (Figure 1.4). More than half we encounter nearly every day! The most widely spread allotrope is graphite (b) which can be found in pencils and electric motor brushes. (a), (b) and (c) are the crystal lattice structures of diamond, graphite which is a stacked layer of graphene sheets, and lonsdaleite (hexagonal diamond) respectively. Graphene at the moment is one of the newest emerging allotropes of diamond that make high ranking journals and breaking science topics [22]. The fullerenes, (d), (e) , (f) and (h) were discovered some

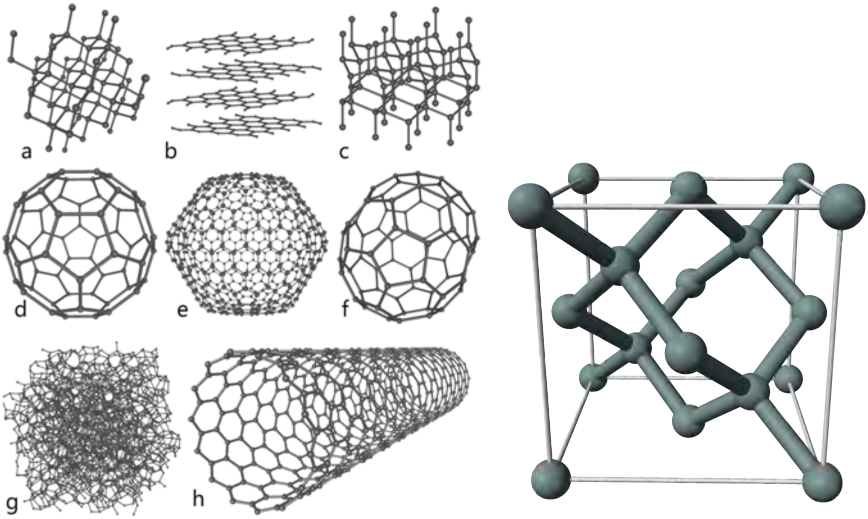

(a) (b)

Figure 1.4: (a) Eight allotropes of carbon. a. diamond b. graphite, composed of graphene sheets, c. lonsdaleite, d. C_{60}, e. C_{540}, f. C_{70}, g. armorphous carbon, h. single walled carbon nanotube [20]. (b) A diamond unit cell of the sp^3 carbon atoms [21]

.

longer time ago. All these interesting carbon materials have led to many new advances in electronics and nano-science.

In contrast to all other carbon allotropes, diamond is the only allotrope where all carbon atoms are fully hybridized so all bonds form tetrahedral structures around the sp^3 carbon. This leads to the diamond crystal structure which is a double face-centred cubic (FCC) lattice with rigid σ bonds

Table 1.3: The superiorty of diamond.

Material property	Value
Young’s Modulus	1050 GPa
Hardness (Mohs’ scale)	10
Thermal conductivity	> 2000 W/(m·K)
Chemical inertness in air	> 5000°C

which partly explains some of the remarkable properties of diamond (Table 1.3). The cubic unit cell of diamond is shown in Figure 1.4 (b) [23].

1.5.2 Chemical vapor deposited diamond materials

Most natural diamonds are formed at high-pressure high-temperature conditions, typically at depths of 140 to 190 km in the Earth's mantle. Their formation takes billions of years. There is also a synthetic way to mimic this: the high-pressure-high-temperature (HPHT) technique. This yields in the purest form of synthetic diamond but it is not used in this work. An alternative, invented by the back than called Soviets, is to work on low pressure by growing diamond from a vapor phase. This technique is called chemical vapor deposition (CVD) and can be found in Figure 1.5 as metastable CVD diamond.

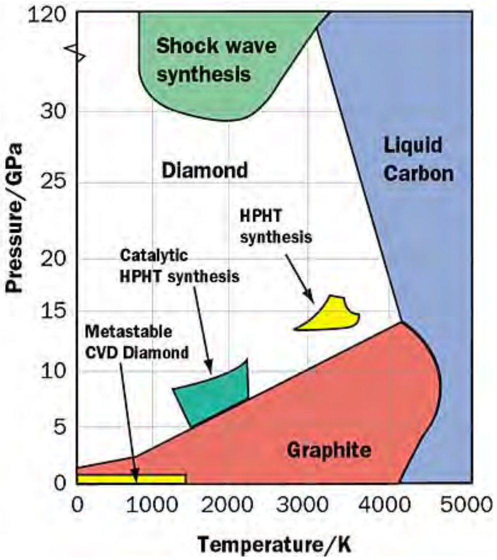

Figure 1.5: Overview of carbon phases possible with certain pressure versus temperature relation (source: [24]).

For CVD three components are required: a substrate, a seed layer and a growing mechanism. The substrate is a very important parameter because it serves as the carrier to provide stability for the brittle diamond film. It can be Silicon (Si), Silicondioxide (SiOx) or a metal such as Titanium (Ti), Tungsten (W), PlatinumIridium (PtIr), etc. In order to grow

diamond it is necessary that the substrate temperature is at elevated temperatures (typically above 500°C). This requires matching of the temperature expansion coefficients of the substrate and the diamond layer to avoid any cracking of the film upon temperature changes during and after growth. Also the substrate must be capable to hold on to the adhered detonation nanodiamonds (DND), also called ultra-dispersed diamonds (UDD) that serve as a seed layer. The UDD can be added by mechanical abrasion [25], ultrasonic particle treatment [26, 27], bias enhanced nucleation [28, 29], and nano-particle seeding of UDD powder immersed in water or alcohol. When a substrate is immersed in this colloidal suspension the diamond particles adhere to the surface by Van der Waals forces forming a layer of roughly 5 nm particles with a seeding density $\pm 10^{11}$ seed/cm^2 [30, 31].
The seeded surface provides a point of origin for diamond growth. This is done in a microwave with a carbon containing process gas (typically methane CH_4) under low pressures (± 30-200 mbar) and increased temperatures (700 ± 200°C). As mentioned before, these conditions give rise to the metastable growth phase. A side effect of this growth condition is the continuous formation of sp^2 graphite which must be selectively and continuously etched (because graphite is the most favorable phase of carbon with the lowest energy). Therefore, besides methane, also hydrogen gas (H_2) needs to be added to the gas phase to promote the graphite etching. From this it makes sense that when there is more hydrogen during growth, the quality of the diamond improves because there is more sp^2 etching resulting in a diamond with a high sp^3 content with respect to sp^2 (for instance a C/H-ratio of 0.5% results in higher quality diamond than a C/H ratio of 5%).

The diamond used in this work was grown in a Microwave Enhanced Plasma Chemical Vapor Deposition (MWEPCVD) ASTEX reactor in which the gasphase was activated by a microwave plasma [32]. Other activation mechanisms such as Hot Filament (HF) reactors can coat larger surfaces (more uniformity during growth) whilst CVD is the prize winner of all the techniques which can grow on medium surfaces (ideally 2" wafers) with a relative fast growth speed (6 ± 5 nm/min) resulting in very pure diamond films [31]. The microwaves, operating at 2.45 GHz ignite the gases into a plasma that causes diamond to grow from the seeds in a columnar way by a reaction of atomic hydrogen with methane which in turn react with the diamond seeds at the surface. When diamond is doped, impurities are incorporated by adding an extra gas to the mixture. For boron incorporation, Trimethylborane (TMB) gas is used in various concentrations to achieve different doping levels ranging from semi-conductive to metallic properties. In Figure 1.6 a schematic representation of the growth mechanism is shown. The final result (shown in Figure 1.7) is a closed polycrystalline diamond film in which diamond crystallites are interconnected by grain boundaries. The cross section from panel (b) shows the columnar orientation of the crystallites.

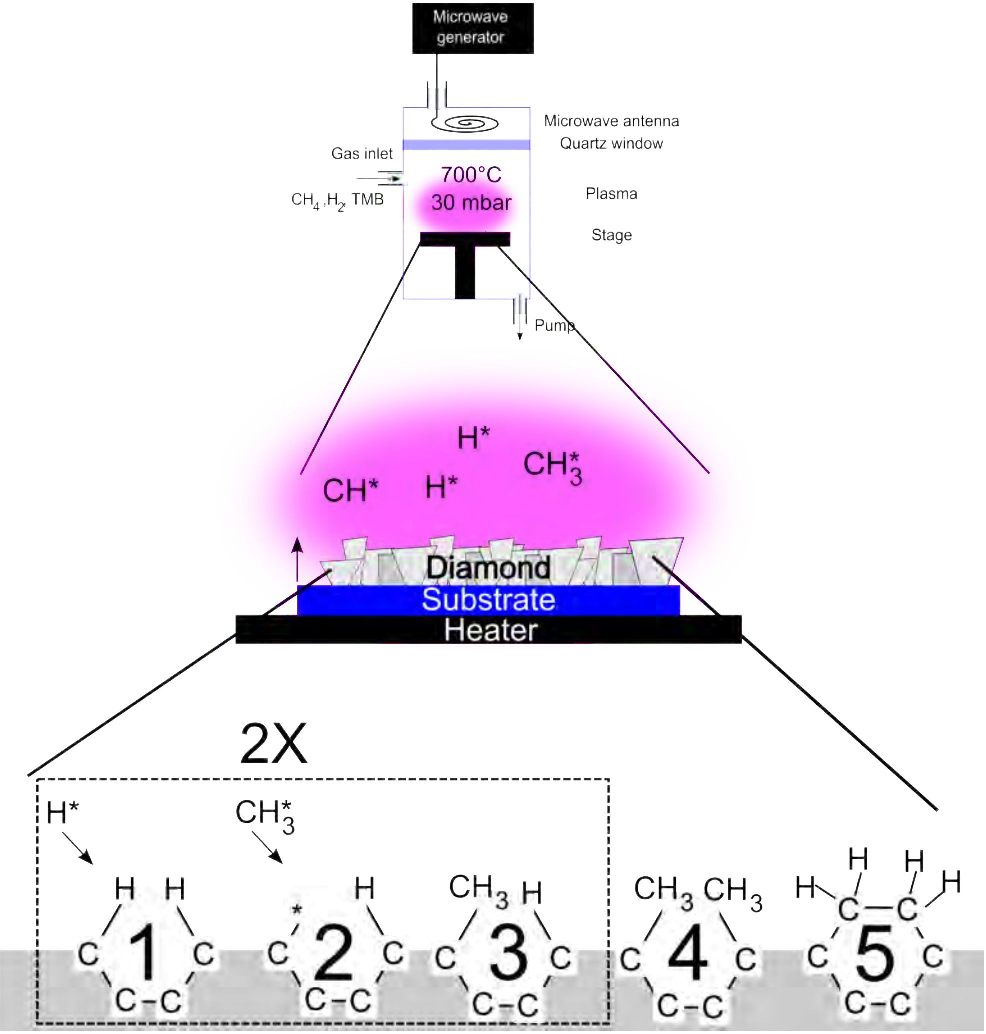

Figure 1.6: Schematic representation of the diamond growth in a MWEPCVD reactor with the role of CH_3 as growth species.

These deposited diamonds are widely available and exist in various types. The most common forms are monocrystalline, polycrystalline, nanocrystalline and ultrananocrystalline diamond.

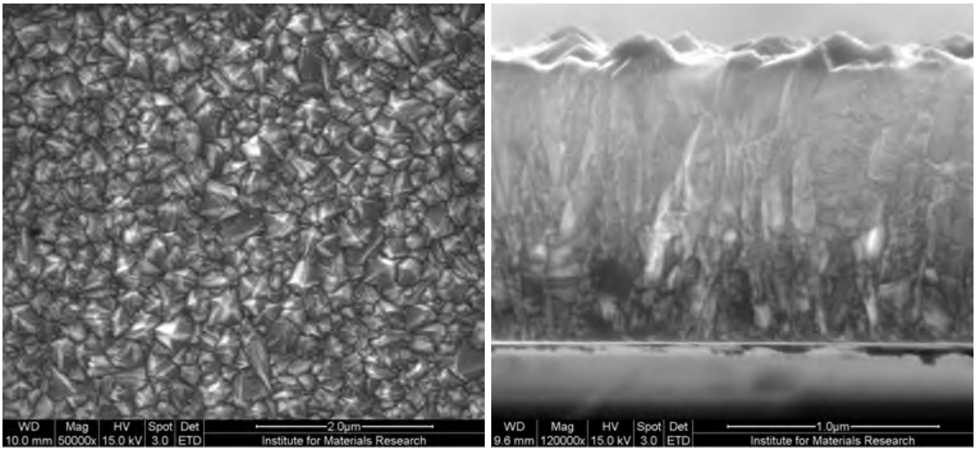

(a) (b)

Figure 1.7: SEM recording of nanocrystalline diamond: (a) top-view (b) cross-section of a freestanding diamond film by breaking a sample and accidental delamination. The columnar structure of the diamond film can clearly be seen).

The different properties of these diamond specimens enable different applications, i.e. monocrystalline diamond is not necessarily the best option for all applications. Several parameters can be used to identify the suitability of the diamond material depending on the application. Among them, surface morphology, electrical conductivity, capability of device fabrication, substrate nature, dimensions, electrochemical properties (influenced by the sp^2/sp^3 ratio), possibility of surface conductivity (surface termination), cost, etc [33].. In the following sections the most relevant properties of different diamond species are briefly discussed

Monocrystalline diamond (MCD)

Monocrystalline diamond, especially when polished are ideal for micro- or nanopatterning, and for the study of structural properties of organic monolayers because extreme small roughnesses up to 0.13 nm can be obtained.

Monocrystalline diamond also exerts the lowest sp^2 content of all diamond materials, which results in its excellent electrochemical performance such as large electrochemical potential window and low background current [34]. Besides the cost, the main disadvantages of single-crystalline diamond are the small size (typically 5 x 5 mm^2) and the limited availability for high boron doping which makes it difficult to handle for biosensing applications.

Microcrystalline diamond (μCD)

Either intrinsic or highly boron doped (B-doped) μCD films are available on large substrates or as freestanding films. 500 nm and larger is the accepted grain size threshold to determine μCD. Due to its polycrystalline nature, and depending on the thickness, as-grown μCD films exhibit a very high surface roughness ($\sim$ μm) which hampers their use for those applications in which micro-/nano-patterning is important. Polishing is possible albeit a higher cost. Due to the availability of metal-like B-doped diamond films, and together with relatively low sp^2 content (mostly located at the grain boundaries), this material is widely used commercially for electrochemical applications.

Nanocrystalline diamond (NCD)

Nanocrystalline diamond thin films have grain sizes below 500 nm. As mentioned before they can be grown on different substrates, mainly quartz and silicon. It was shown that NCD can be B-doped very efficiently, so that metal-like films can be obtained [35], thus paving the way for several electrochemical applications [36, 37]. Compared to μCD the surface roughness is much lower (in the order of 10 to 20 nm). Compared to MCD and μCD there is a larger amount of sp^2-bonded carbon present in the grain boundaries which not favors superb electrochemical properties [38]. Because of the low surface roughness and its relatively good electrochemical properties as compared with other carbon-based materials, B-NCD electrodes are very promising for bio-electrochemical applications [39].

Ultrananocrystalline diamond (UNCD)

Ultrananocrystalline diamond films arise from an Argon-rich plasma and have grain sizes below 10 nm [40]. UNCD films, with a roughness down to 5 to 10 nm, are available on standard substrates like Si and quartz, as well as on metals. UNCD films are expected to have the largest sp^2/sp^3 ratio of all the diamond materials discussed here, thus influencing the electrochemical properties largely because the grain boundary content makes up of 10% of the film. Just as NCD, UNCD films have clear advantages compared with other carbon-related materials: UNCD-electrodes still exhibit a larger electrochemical potential window and lower background electrochemical current than do electrodes such as highly oriented pyrolytic graphene (HOPG).

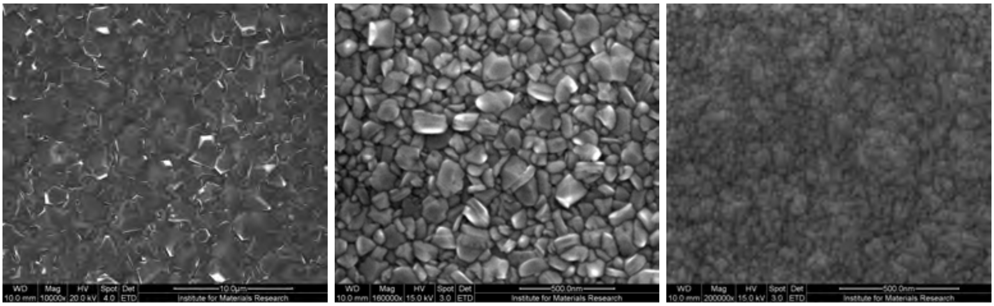

(a) (b) (c)

Figure 1.8: SEM recording of (a) μ-crystqlline diamond, (b) nanocrystalline diamond and (c) ultrananocrystalline diamond. (note the scale bar).

1.5.3 Doping of diamond

The four valance band electrons involved in bond formation cause pure diamond to be an insulator with a bandgap, E_{BG}, of 5.47 eV. The large band gap originates from the small size in carbon atoms causing the spatial overlap between molecular orbitals of adjacent C atoms to be relatively large. This causes a large band gap between the valence band (VB) and the conduction band (CB). To decrease this band gap it is possible to perform in situ doping during CVD growth. The doping can be done by introducing low concentrations of either phosphorus (group V, electron

conduction) or boron (group III, hole conduction).
The gap induced by the boron serves as an acceptor that gives rise to a hole, or missing electron. The hole acts as a positive charge that can move through the crystal [41]. In this thesis all the work has been done on p-type diamond doped with boron in a concentration range from 800 to 9000 ppm TMB during the growth phase.

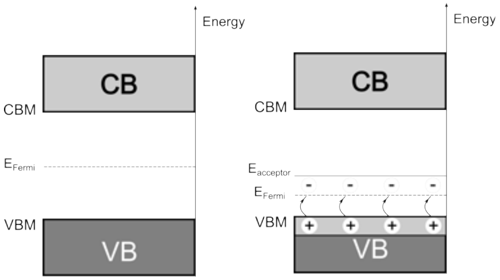

Figure 1.9: Schematic band energy diagrams for bulk diamond that is undoped (a) or p-type doped (at T > 0K) (source: [41]).

1.5.4 The surface of diamond

At the end of the bulk, there is a new interface with another material possible such as a metal, another semiconductor or even the air or liquid. At this interface the diamond lattice stops and has unsaturated bonds that dangle in *'free space'* (dangling bonds). These can be put to use for chemical treatment to (bio-) functionalize the surface. The surface of diamond is completely dependent on the bulk properties meaning that the diamond crystals facing the interface have certain crystal orientations (100, 110, 111). Depending on which orientation, a different amount of dangling bonds is available per crystal. Also the roughness plays a important role because an increased roughness causes the surface area to increase and therefore also the availability of additional dangling bonds. The occupation of dangling bonds by other atoms/molecules is dependent on the sterical hindrance that arises from two neighboring dangling bonds, indicating that a perfect coverage of the surface by chemical modification is not possible. For diamond surfaces a lot of research has been performed. The chemical modifications can range from elemental changes (such as oxygen, hydrogen or fluorine) but also larger molecules can be tethered for specific bio-functionalization [42, 43].

Hydrogenated diamond

At the end of the CVD growth the diamond is in contact with the H-plasma causing the dangling bonds to be saturated with monovalent hydrogen. The hydrogenated surface is very stable and results in a hydrophobic layer with high surface free energies. The hydrogen termination can always be regenerated by re-exposure of the diamond to a hydrogen plasma. In addition the $C^{\delta-}$ - $H^{\delta+}$ dipoles at the surface cause upward band bending in a thin, near-surface layer inside the diamond, together with the adsorption of a thin atmospheric water layer that is essential for the p-type surface conductivity [44, 45].

Oxidized diamond

By exposing the diamond surface to an oxygen plasma, ultraviolet induced ozone (uv-ozone) or wet chemical acid treatments an oxidized diamond surface is achieved. The surface has a variation of oxygen groups such as ketones (=O), hydroxyl (C-O-H), carboxyl (O=C-O-H) and/or ether (C-O-C) groups. These groups have a high polar character and cause the diamond to become very hydrophilic. Since oxygen has a higher electron affinity than carbon, the surface dipoles on oxidized diamond are oriented opposite as compared to H-termination: $C^{\delta+}$ – $O^{\delta-}$. This results in a downward band bending [46]. The conduction band minimum (CBM) is below the vacuum level, corresponding to a positive electron affinity. Consequently, oxidized diamond is not surface conductive, even if the same adsorbed species are present as on H-terminated diamond.

1.5.5 The diamond liquid interface

Figure 1.10 represents the hydrogenated surface of a metallic-like B-doped diamond and single crystal diamond in an aqueous solution. The H-termination is known to induce a negative electron affinity, with a value of -1.3 eV measured in vacuum [45]. The presence of water molecules screening the C-H surface dipole is expected to reduce the value of the electron affinity (χ) towards less negative values. Therefore an approximation of $\chi \sim$ - 1.0 eV is used. The metallic nature of the B-doped NCD (B-NCD) is represented by the position of the Fermi energy (E_F), which is below the valence band maximum (at 4.45 eV assuming χ = -1.0 eV). Under these conditions, the

B-doped diamond electrode can be described as a normal metal electrode. It is important to consider the following reactions because when immersed in an aqueous solution, the Fermi level of H-terminated diamond is in thermodynamic equilibrium with the electrochemical potential determined by these redox reactions [44, 47, 48].

$$O_2 + 2H_2O + 4e^- \longleftrightarrow 4OH^- \tag{1.1}$$

and

$$H_2 + H_2O \longleftrightarrow H_3O^+ + e^- \tag{1.2}$$

The band diagram in case of a single crystal H-terminated surface has several differences as compared to the B-NCD electrode. The H-termination of the diamond surface induces the same negative electron affinity, χ = -1.0 eV, which fixes the value of the valence band maximum at the same position, 4.45 eV. In the case of the metallic-like BNCD, the Fermi level lies below the valence band maximum as a result of the very high doping level. However, in the case of the undoped H terminated single crystal in an aqueous electrolye, the position of the Fermi level at the surface can be determined by the electrochemical potential energy of a redox reaction occurring in the solution assuming thermodynamic equilibrium, and the electrochemical potential determined by the reference electrode. Thus, an accumulation of holes is induced at the diamond surface. With the Fermi level within the valence band, the surface conductive diamond electrode behaves like a metal electrode.

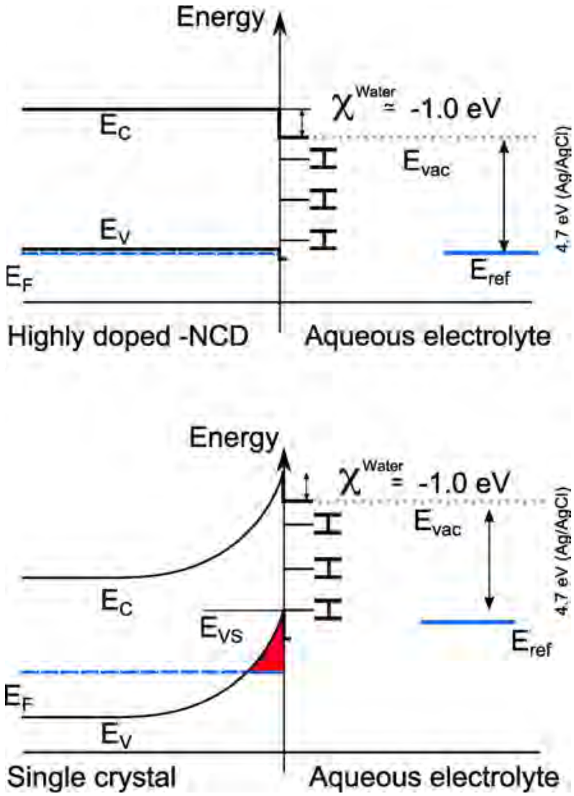

Figure 1.10: Schematic representation of the energy band diagram of the interface between an aqueous electrolyte and H-terminated (a) B-NCD and (b) a single crystal diamond. Both cases show negative electron affinity as a result of the C - H surface dipole.

Besides the band bending an additional effect is observed when diamond, or any other electrode, is immersed in an electrolyte. Here the transformation from electronic to ionic conduction occurs.

Electrostatic interactions between the ions in the solution and the electrode surface result in a charge density at the electrode surface that arise from either an excess or deficiency of electrons, here electron transfer is the key process whereby the electrode exchanges charges with the arriving ions or ionizes neutral substances. Without electron transfer there is no chemical electrode reaction, no direct electrode- and Faradaic current.

As soon as the electrode is wetted a double layer is formed to keep the interface neutral by a redistribution of ions close to the surface to balance the charges (Figure 1.11). In all the interfaces there is a non-uniform distribution of charges. First, there was the Helmholtz model which stated that the double layer is a molecular capacitor, where one plate is represented by the charges in the electrode and the other plate by equal counter-ions in the electrolyte. The charge separation is small (± 0.5 nm) so the capacitance is enormous. Yet, this model is only valid for rather high concentrations of electrolyte solutions. However, this simple model states that the double layer is depleted of charges, but the transition is not this abrupt and Gouy-Chapman took the exchange of counter ions between the double layer and the bulk solution due to thermal motion into account. Both Coulomb forces and thermal motion influence the equilibrium distribution of counter ions in their model for the diffuse double layer. The assumptions for this theory state that the surface charge is continuous and uniform and secondly the ions in the solution are point charges. Finally, both models were combined by Stern who takes the finite size of ions and their binding properties at the surface, into account. In this way the best approximation for the electrode/electrolyte interpretation was made. The Stern modified Gouy-Chapman diffuse double layer model states that ions have a finite size, so they cannot approach the surface closer than a few nm. Also he stated that it is possible that ions are specifically adsorbed at the electrode and this layer has become known as the Stern layer which has a stern potential (ψ_s). Therefore, the potential will drop linearly over the *molecular condenser* (i.e. the supposed Helmholtz plane). Subsequently the potential will then decrease exponentially through the diffuse layer (ψ_d) in which the zeta potential (ζ) is reached at the Debye length κ^{-1}. A scheme to clarify this is shown in Figure 1.11. To comprehend these theories in a simplified way we state that the Stern modification is essentially a combination of the Helmholtz and Gouy-Chapman models. It assumes a 'plane of closest approach' where a portion of the excess ions reside and attaches to a Gouy-Chapman type 'diffuse layer'. The combined result is that the concentration of counter ions is the highest near the solid surface and decreases as the distance from the surface increases, whereas the concentration of determining ions change in the opposite manner. Such inhomogeneous distributions of ions in the proximity of the solid surface lead to the formation of so-called double layer structure described above. In this thesis we use the Stern model for double layer approximations.

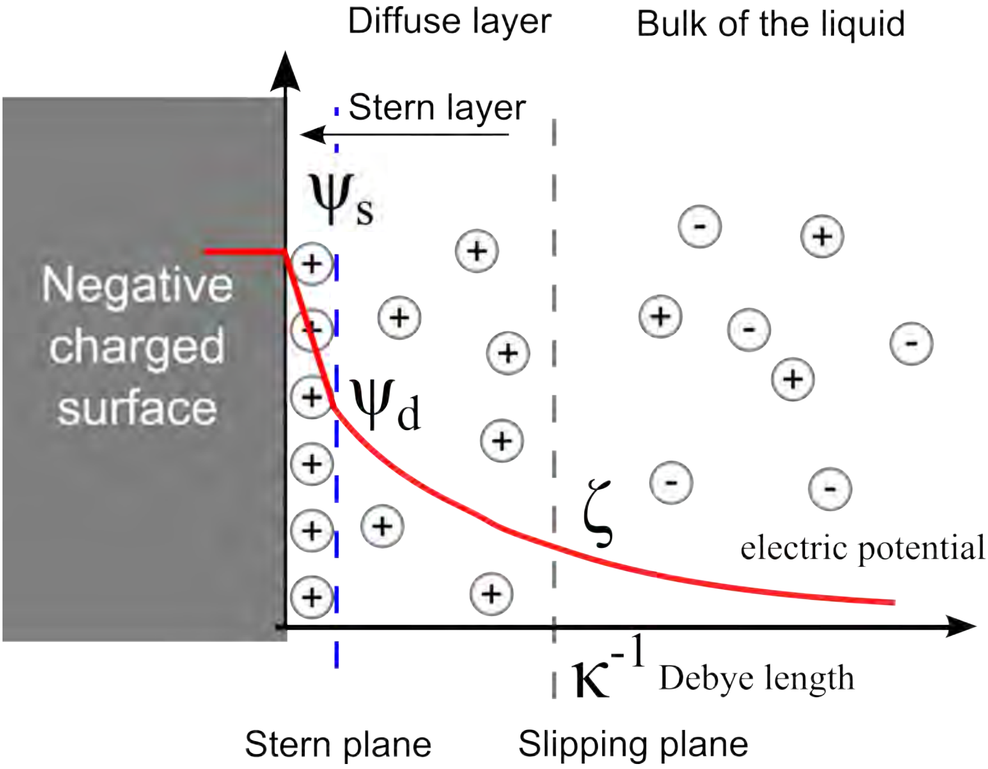

Figure 1.11: Schematic model of the double layer formed at an electrode immersed in an electrolyte. Different layers and planes can be distinguished depending on the behavior of the ions.

The thickness of the Gouy-layer is defined by the Debye screening length, which can be calculated by:

$$\lambda_D = \sqrt{\frac{2N_A e^2 I}{\epsilon_r \epsilon_0 k_B T}} \tag{1.3}$$

with the ionic strength

$$I = \sum_i z_i^2 c_i \tag{1.4}$$

With N_A Avogadro's constant, e is the elementary charge, ϵ_0 is the permittivity of the vacuum and k_b is Boltzman's constant. T is the absolute temperature and ϵ_r is the relative permittivity. The number to use for ϵ_r, where mostly ϵ_r=78 is assumed at room temperature for aqueous electrolytes, is not always clear since the relative permittivity in a region of hindered mobility decreases. z is the charge carried by the i^{th} specimen and c is the concentration. With physiological salt concentration (150 mM) the double layer thickness is less than a nanometer (0.84 nm), but it can reach up to more than a micrometer for distilled water.

1.6 What kind of immunosensors exist?

In Section 1.1 we have shown that biosensors became an independent research branch on the junction of different disciplines. In the following Table 1.4 an overview is given of some recent immunosensors. As the name implies, immunosensors use antibodies as a recognition element against a large variety of analytes (heavy and low molecular weight molecules). Also the transducer element, which is in this thesis diamond, can vary a lot with most commonly gold serving as electrode. The read-out technique and the detection limit are also widespread depending on the research. The literature is overwhelmed with other types of sensors that do not use antibodies but instead have DNA, cells, aptamers, imprinted polymers etc. We will not discuss any of these because it would bring us out of focus regarding the immunosensors.

1.7 State of the art CRP detection systems

In Table 1.4 we focussed on the antibody based recognition element. In Table 1.5, the variety of sensors that are directed against the C-Reactive Protein are summarized, as this is the target molecule in this project.

Table 1.4: Literary overview of a variety of immunosensors up to date.

Analyte	Electrode/transducer	read-out	detection range	Reference
Casein	Gold-nanoparticles	Cyclic voltammetry (CV)	10^{-7} to 10^{-5} mg/ml	[49]
anti-biotin IgG	Gold-nanoparticles	CV	5 to 500 ng/ml	[50]
α-fetoprotein	Gold-nanoparticles	CV	1.25 to 200 ng/ml	[51]
PFHP-2	Nano-/microparticles	CV	31 ng/ml	[52]
BMP-7	Quantumdots	Fluorescence	1 ng/ml	[53]
CFP-10	Gold	Surface plasmon resonance	100 ng/ml to 1μg/ml	[54]
Benzopyrene	Gold	InfraRed	5μM	[**?**]
P24 antigen (HIV)	Carbon nanotubes	Amperometric	0.01 to 60 ng/ml	[55]
Atrazine	**XXXXX**	Amperometric	XXXX	[56]
H-IgG	Graphene	Electrochemical	0.1 to 100 ng/ml	[57]
Myoglobin	Gold	Impedance	10 ng to 650 ng/ml	[58]
ABA	Gold	Impedance	0.5 to 5 ng/ml	[59]
Azidothymidine	Diamond	Amperometric	/	[60]
CA-125 (cancer)	Gold	SPR	50 nmol/ml	[61]
Troponin-I	Gold	SPR	1-160 μg/ml	[62]
Tetrodotoxin	Gold	SPR	/	[63]
Cortisol	Gold	SPR	10μg/l	[64]
Influenza A	Gold	Quartz Crystal Microbalance (QCM)	10^3 pfu/ml	[65]
Dioxin	Gold	QCM	0.1 to 0.01 ng/ml	[66]

Table 1.5: Literary overview current CRP detection methods

Label-free?	Electrode/transducer	Read-out	Detection range	Reference
Fe-Nanoparticle	CNT	Amperometric	0.16 μg/l	[67]
Competitive assay	Gold	D-QCM	1 ng/ml to 10μg/ml	[68]
Cystein tag	Gold	Field effect	2 to 20 μg/ml	[69]
Magnetic beads	Gold	Aptamers/SELEX	12.5 μg to 10 mg/l	[**?**]
Secondary Ab	Gold	SPR	2 to 5 μg/ml	[70]
Secondary Ab	Dendrimers	Optical	0.1 to 100 ng/ml	[71]
Secondary Ab	/	immunochromatographic	0.5 to 20 μg/ml	[72]
?		Automated system RXL analyzer	1 to 60 μg/ml	[73]
Magnetic nanoparticle	/	Optical	1.2 to 310 μg/ml	[74]
Yes!	Diamond	Impedance spectroscopy	10 nM to 1 μM	[75]
Chemical reaction	/	Turbidimetry	1.7 μg/ml	[76]
Chemical reaction	/	Nephalometry	1 to 400 μg/ml	[**?**]

1.8 Aim and focus of this work

In this work we focused on different aspects of the biosensor. The main goal was to realize a label-free electrochemical immunosensing platform on diamond films for the detection of cardiac markers. The platform was a boron doped nano-crystalline diamond film on which immunoglobulins were immobilized. In the following points a brief summary is given of the aims proposed in this work:

1. In chapter 3 the characterization and optimization of the morpho-electrochochemical properties of diamond films serving as electrodes were studied. Here different growth conditions were compared and an optimum was determined. In addition, we also studied the coating of metal electrodes with high quality microcrystalline diamond to improve the electrochemical properties. The main characterization techniques used here were impedance spectroscopy and cyclic voltammetry.

2. Chapter 4 deals with the understanding of biofunctionalization of the diamond surface. Different surface terminations have different effects on protein behavior, and in turn also on the electrochemical response. In addition there is also the need for various functionalization routes to tether biomolecules on the diamond surface.

3. Chapter 5 discusses the immunosensing of proteins. Here buffer solutions and human serum samples were spiked with CRP and the detection was monitored label free with impedance spectroscopy. Additionally we tried different optimization efforts to improve the signal intensity .

4. The final goal, discussed in chapter 6, was to miniaturize diamond electrodes for micro-array applications. Here the construction and interfacing is shown. We also show a secondary route to create diamond structures with high throughput and great accuracy. Finally, we show some proof of principle measurements on protein adsorption and DNA denaturation.

Chapter 2

Materials and Methods

This chapter gives an overview of the standardized protocols and materials used in the following chapters. The techniques that are performed on individual basis are discussed in more extent whilst the techiques operated by experts are briefly summarized. Experiments that were done with different approaches will therefore be described in the corresponding chapters.

2.1 Physiological solutions and chemicals

Phosphate buffered saline Nearly all measurements or sample preparations were performed in physiological buffer solutions. The standardized buffer was phosphate buffered saline which is an aqueous-based salt solution. The buffer helped to maintain a constant pH. The osmolarity and ion concentrations of the solution usually match those of the human body (isotonic). The recipe for a 10 × PBS solution was: 1.29 M NaCl, 0.05 M $N\alpha_2HPO_4 \cdot 2\,H_2O$, 0.015 M KH_2PO_4, pH 7.4). Next the stock was sterilized by autoclaving (20 min, 121°C) and afterwards stored in a refrigerated environment (4°). Concentrated stock solutions may precipitate when cooled and should be kept at room temperature until the precipitate has completely dissolved before use. The stock was diluted to 1 × PBS with MilliQ water (ddH2O) (Sartorius, Diegem, Belgium). After aliquots were made of 1 × PBS, the pH was re-adjusted to 7.4.

CRP buffer The purchased antigen, C-reactive protein, was dissolved in CRP buffer. This consisted of 20 mM tris(hydroxymethyl)aminomethane (TRIS) -buffer at pH 8, containing 0.28 M NaCl, 0.09% NaN_3 and 5 mM $CaCl_2$).

MES buffer When DNA was used, instead of proteins, the supporting buffer was always 2-(N-morpholino)ethanesulfonic acid-buffer (MES) at pH 6.2 (Sigma, Bornem, Belgium). MES buffers ensures optimal coupling conditions when used with the carbodiimide procedure.

EDC/NHS Covalent coupling of biomolecules was done by the conventional EDC/NHS protocol. EDC or 1-Ethyl-3-[3-dimethylaminopropyl] carbodiimide hydrochloride is a zero-length crosslinking agent used to couple carboxyl groups to primary amines (amide bond). EDC reacts with a carboxyl to form an amine-reactive O-acylisourea intermediate. If this intermediate does not encounter an amine, it will hydrolyze and regenerate the carboxyl group. In the presence of N-hydroxysulfosucciminimide (Sulfo-NHS), EDC can be used to convert carboxyl groups to amine-reactive Sulfo-NHS esters.

Sodium chloride/sodium citrate (SSC) and Sodium dodecyl sulfate (SDS) Washing steps after DNA coupling was performed in SSC/SDS buffer. The SSC consists of 3 M NaCl together with 0.3 M citrate $C_6H_8O_7 \cdot 3Na$ at pH 7.5. SDS is an anionic surfactant with amphiphilic properties. The total buffer was composed of 2 × SSC buffer + 0.5 % SDS and the washing took 2 hours at 60°C.

'The diamond cleaning juice' Diamond cleaning and diamond oxidation have a different meaning regarding biosensor substrates. The wet-chemical oxidation of diamond was done in an aggressive cocktail of sulfuric acid (H_2SO_4) and potassium hydroxide (KOH) at 180°C for 2 hours (or more). After this boiling step the samples were 3 times washed thoroughly with deionized water under thermal (120°C, 5 min) and ultrasonic agitation for 5 min (US). However this harsh treatment is not good (even worse when done frequently) for the health of the diamond film, especially regarding microstructures discussed later. Therefore the standard cleaning of diamond was done as follows: The samples were washed with acetone (15 min, US) in case there were some silverpaint (eutectic) remainders. Next a washing step in Norvanol (15 min, US) followed by a short acid dip which was a less concentrated mixture as described above (5 min, 180°). If necessary piranha etch could be used to remove any organic residues. It consisted of a 3:1 mixture of sulfuric acid H_2SO_4 and hydrogen peroxide H_2O_2. Because the mixture is a strong oxidizer, it will remove most organic matter, and it will also hydroxylate most surfaces (adds -OH groups), making them extremely hydrophilic (water compatible). To remove desorbed metal ions a 'base piranha' was used by mixing ammonium hydroxide NH_4OH with hydrogen peroxide (3:1).

2.2 Biological materials

Primary antibody The pirmary antibody was an affinity purified monoclonal immunoglobulin G (IgG) synthesized in a mouse host against the human target (CRP) (Scipac, Kent, UK). The stock solution has a final concentration of 20 μM and was stored in small aliquots to avoid excessive freeze thaw cycles. Storage was always at -18°. The IgG's have a molecular weight of 150 kDa with an iso-electric point between pH 6.2 and 6.4.

Secundary antibody To visualize the primary antibody, a secondary goat-anti mouse antibody with an Alexa-488 or -555 label was used (Sigma, Bornem, Belgium). The affinity was chosen in such a way that an immunological recognition between the primary and secondary antibody could take place. A single labeled antibody has an average of 6 Alexa dye molecules bound to its quaternary structure. XPS quantification was done with a goat-anti-mouse antibody labeled with a Bodipy FL fluorescent dye (invitrogen, Gent, Belgium).

Bovine Serum Albumin Lysophylized Bovine Serum Albumin (BSA) was used as a blocking layer. The dried powder was diluted in 1× PBS to a final concentration of 6 w%. Blocking of the immunosensor was done overnight at 4°C or 2 hours at room temperature (22.5°C). The molecular weight is 66.7 kDa and the iso-electric point is around pH 4.7.

C-reactive protein (CRP) C-Reactive Protein was bought in its pentamer form from Scipac (Kent, UK). The proteins were stored at 4°C in a TRIS buffer and were >96% purified.

8bp single stranded probe DNA Characterization of different functionalized diamond surfaces was done by DNA strands with an 8 basepair (bp) sequence (5'-CCC CTG CA-3'). At the 5' end there was a 6 carbons spacer followed by the functional group -NH_2 or -COOH. At the 3' end there is a fluorescent dye molecule (Alexa-488) (Eurogentec, Luik, Belgium).

2.3 Characterization techniques

2.3.1 Contact angle goniometry (CA)

Wetting behavior and surface free energies (SFE) of diamond films are of special importance for biosensor-research. To probe these properties contact angle goniometry is used. Here, a droplet of test liquid is dropped on a surface and the resulting contact angle between the tangent to the fluid curvature and the tangent to the surface of the solid support (also called the 'baseline') is measured (see Figure 2.1). The wetting behavior of the surface depends on the adhesive and cohesive forces between the liquid and the surface. Adhesive forces between a liquid and a solid cause a drop to spread across the surface. Cohesive forces within the liquid cause the drop to ball up and avoid contact with the surface [77]. When a drop of liquid is brought in contact with a surface, three phases come into contact: the liquid of the test fluid (L), the gases and vapor constituting the ambient air (V), and the solid of the sample surface (S) under study. The drop will contract or expand to minimize or maximize its contact area, depending on which is energetically favorable. Young derived an equation which makes a relation between a certain contact angle (θ) of a droplet on a surface and the accompanying surface energy (SE):

$$\gamma_{sv} = \gamma_{sl} + \gamma_{lv} cos\theta \tag{2.1}$$

Where the three coefficients γ are the surface energies at the solid/gas (γ_{sg}), solid/liquid (γ_{sl}) and liquid/gas (γ_{lg}) interfaces, respectively. SE is expressed in J/m^2 or N/m. In order to calculate the γ_{sg}, when knowing the γ_{lg} and missing the value of γ_{sl} different techniques can be employed like the combining rule of Girifalco-Good-Fowkes-Young, the Zisman critical wetting tension, Owens-Wendt-Rabel-Kaelble (OWRK) geometric mean, the Wu harmonic mean and the acid-base theory of Lewis.

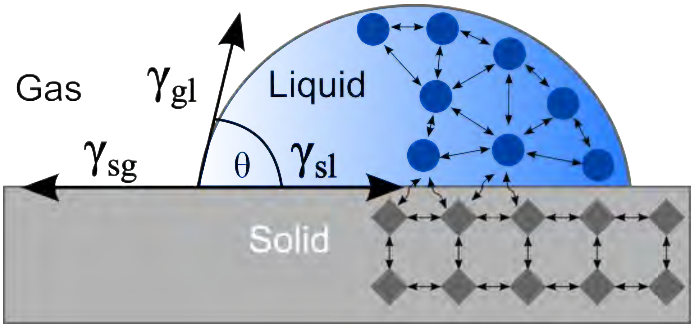

Figure 2.1: A cartoon of the droplet/gas/solid interface. The surface energies and contact angle are represented as θ for the CA, γ_{lg} for the liquid/gas interface, γ_{sg} for the solid/gas interface and γ_{ls} for the liquid/solid interface.

Surface free energy (SFE) values can be extracted from contact angle measurements by the OWRK method. They described that the surface energy of any solid or liquid phase can be split up into two components: A dispersive γ^D and a polar γ^P part.

$$\gamma = \gamma^D + \gamma^P \tag{2.2}$$

The γ^D results from non-polar interactions of molecules, e.g. induced dipole-dipole interactions and the γ^P depends of polar groups interactions e.g. hydrogen bonding and dipole-dipole interactions. This means that the liquid and the solid can also be split up:

$$\gamma_s = \gamma_s^D + \gamma_s^P \tag{2.3}$$
$$\gamma_l = \gamma_l^D + \gamma_l^P \tag{2.4}$$

Only the polar parts of the liquid can interact with polar parts of the solid and vice versa for the disperse components the following formula is obtained:

$$\gamma_{sg} = \gamma_{sl} + \gamma_{lg} - 2(\sqrt{\gamma_{sg}^D \cdot \gamma_{lg}^D} + \sqrt{\gamma_{sg}^P \cdot \gamma_{lg}^P}) \tag{2.5}$$

When Eq. 2.1, 2.3, 2.4 and 2.6 are combined a linear equation is obtained by the OWRK theory.

$$\frac{\gamma_{lg}(1+cos\theta)}{2\sqrt{\gamma_{lg}^{D}}} = \sqrt{\gamma_{sg}^{D}} \cdot \sqrt{\frac{\gamma_{lg}^{P}}{\gamma_{lg}^{D}}} + \sqrt{\gamma_{sg}^{D}} \tag{2.6}$$

Test liquids have known γ_{lg}, γ_{lg}^{D} and γ_{lg}^{P}, the contact angle can be measured and the SFE can be interpolated by plotting the $\frac{\gamma_{lg}(1+cos\theta)}{2\sqrt{\gamma_{lg}^{D}}}$ versus the $\sqrt{\frac{\gamma_{lg}^{P}}{\gamma_{lg}^{D}}}$. In Figure 2.2 an example is shown of such a plot and the intercept and slope of the regression line can be extracted.
The square of the slope results in the polar component $\sqrt{\gamma_{sg}^{D}}$ and the intercept gives the disperse component, $\sqrt{\gamma_{sg}^{D}}$ of the surface. The sum of these parameters results in the total surface free energy.

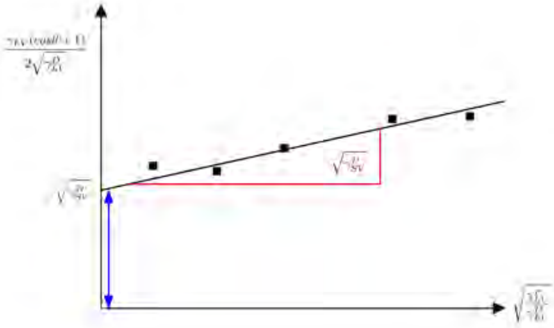

Figure 2.2: An illustration of the use of the 'OWRK' method in determining the surface energy.

Contact angles were measured with a dataphysics OCA 15+ goniometer. Contour ellipse fitting of the droplets was done by the SCA 1.0 software for obtaining the mean values. The droplet size was 1 μl dispensed at 1 μl/sec for all experiments. When dropping a liquid on a surface, fluid settling and evaporation should be left out to obtain the best approach to the correct contact angle. Therefore, an extrapolation of the recorded curve is done. Fitting with a linear and extracting the intercept is the generalized value for the most correct contact angle. In Figure 2.3 an example is given with the obtained, correct, contact angle from the intercept ”102.36°”.

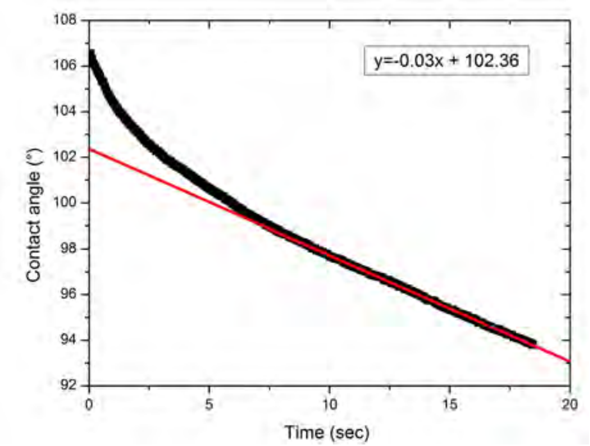

Figure 2.3: An example of how to deduce the mean contact angle from time resolved sessile drop measurements.

2.3.2 Optical microscopy (OM)

Optical characterization of all the diamond substrates were performed weekly to investigate the macro/microscopic quality of the diamond films or synthesized structures. The optical microscope that has been used in this work is an inverted Axiovert 40MAT microscope from ZEISS, equipped with 5×, 10×, 20×, 50× and 100× objectives. A dual light source setup allows transmission and reflection measurements. With respect to the structures of interest either a Dark field, Bright field or dichroic mirror was used.

2.3.3 Atomic Force Microscopy (AFM)

Atomic Force Microscopy (AFM) is a local scanning probe microscopy method. A sharp AFM tip (± 10nm radius) scans over a sample surface to generate high lateral resolution profiles in a localized area. The atomic interactions between the tip and the surface also cause shifts in phase and amplitude providing not only topographical but also morphological (density, hardness) information. The best mode for scanning diamond films is the tapping mode in which intermittent contact is between the AFM tip and the surface, other modes such as contact and non-contact are not very applicable with these films.

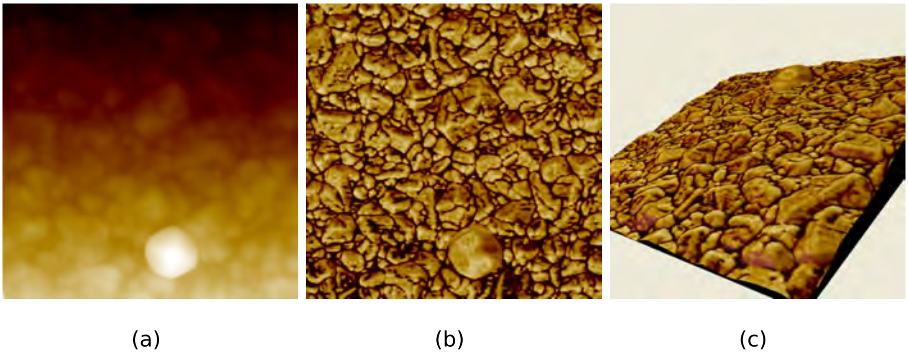
(a) (b) (c)

Figure 2.4: Typical output of an AFM measurement. The topography (a) provides height information, the phase (b) shows dampening of different material properties and (c) is the phase on topography that provides a realistic 3D image of the surface. Amplitude result is not shown.

In Figure 2.4 (b) an example of a typical height, phase and phase on topography image is shown of a NCD surface (The amplitude plot is not shown). AFM measurements in this work were performed with a Veeco Multimode microscope combined with a Nanoscope IIIa controller from Veeco Digital Instruments. Images were recorded in tapping mode. Measurements were performed by Dr. H. Yin.

2.3.4 Scanning Electron Microscopy (SEM)

SEM is a broad area scanning electron microscopy technique compared to AFM. The SEM has a significantly improved spatial resolution compared to light microscopy due to the use of electrons, which have smaller wavelengths than photons. Another great advantage is the higher depth of focus, making it especially suitable for studying surfaces with high roughnesses such as an unpolished titanium electrode shown in Figure 2.5 (a) Recordings in this thesis were made on a field emission gun environmental scanning electron microscope (FEG-ESEM) FEI Quanta 200F FEG-SEM (FEI Europe, Eindhoven, The Netherlands) equipped with energy-dispersive x-ray (EDX) and an electron backscatter diffraction (EBSD) detection. The

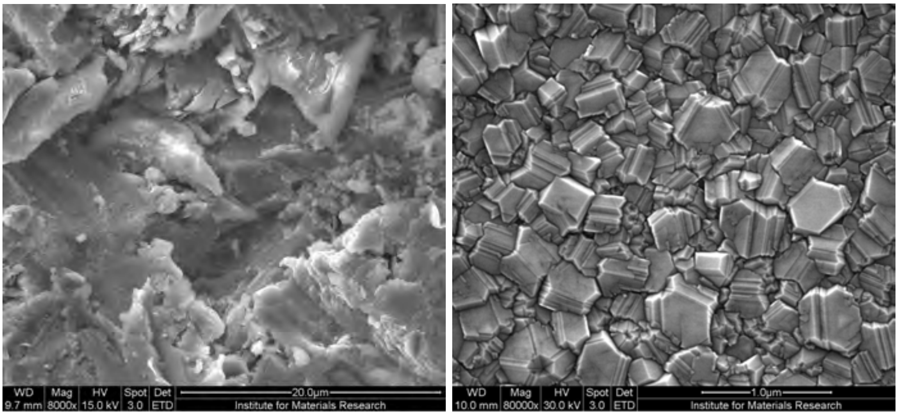

(a) (b)

Figure 2.5: Examples of a SEM recording on a rough titanium surface (a) and a typical ’smooth’ NCD surface.

EDX add-on makes use of x-rays (generated by the electron beam) that allows element fingerprinting. The samples have to be conductive in order to observe them by SEM. If not, the examined surface will be charged with electrons and eventually this charge will cause drift of the electron bundle. This could cause additional problems when using photoresists for e-beam lithography. Typical recordings vary between magnifications of 10 to 200.000 times yielding in a maximum resolution of 5-10 nm. In this thesis, SEM is applied to obtain topographic information based on secondary electrons (an example of a SEM recording of a NCD surface is shown in Figure 2.5 (b)). Recordings were always made by Dr. J. D’Haen and B. Ruttens.

2.3.5 X-ray photoelectron spectroscopy

X-ray photoelectron spectroscopy (XPS) is a (semi)quantitative, surface sensitive, technique that provides information about elemental composition, chemical- and electronic state. XPS is based on the photoelectric effect, meaning that electrons are emitted from the surface by incident X-ray photons. The kinetic energy of these escaped photoelectrons were measured by an electron energy analyzer. Each and single element has its characteristic binding energy that allow fingerprinting of the surface. The amount of detected electrons is counted for each specific energy value of the measured spectrum. The XPS device was a 5600 LS electron spectrometer from Physical Electronics (Chanhassen, MN, USA). X-rays were monochromatic (1486.6 eV), and produced by an AlK$_\alpha$ source. XPS measurements were performed by Prof. Dr. H.-G. Boyen and Drs. M. Saitner.

2.4 Biological Characterization techniques

2.4.1 Covalent DNA coupling

The coupling of DNA was already a well established technique, it could even be used as a benchmark technique to identify the presence of certain chemical groups at a surface. The carbodiimide coupling technique forms an amide bond between a carboxyl (-COOH) and amine (-NH_2) group (Figure 2.6). If a short DNA strand with for instance 8 basepairs is used with on the 5' end a carboxyl or amine group and on the 3' a fluorescent label. Than it is possible to couple such DNA strands to either an amine or carboxy terminated surface respectively. The fluorescent label in combination with (confocal) fluorescence microscopy not only provides evidence **if** the DNA is on the surface but also provides a qualitative view that allows intensity comparison up to a certain extent.

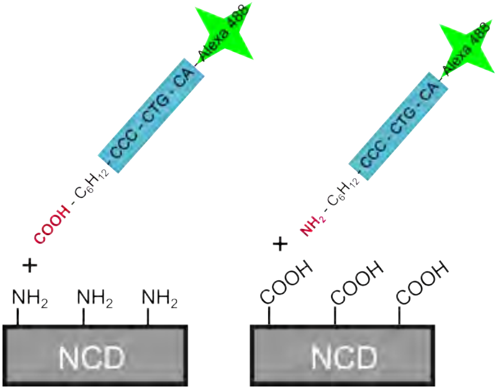

Figure 2.6: DNA coupling used as a benchmark technique for optical characterization (fluorescent label Alexa 488). Via the carbodiimide pathway it is possible to create an amide bonds. 2 different possibilities are shown with either the amine or carboxyl group on the DNA strand.

2.4.2 Confocal fluorescence microscopy

Fluorescence is a relaxation process of an excited molecular singlet state through the emission of a photon [78]. To explain fluorescence, a Jablonski diagram can be used (Figure 2.7 (a)) [79]. If a fluorescent active molecule absorbs a photon with a specific energy, it is excited from the singlet electronic ground state S_0 to an excited electronic state, e.g. S_1, and a certain vibrational substate. The excited state is unstable and the molecule relaxes back to the ground state via radiative and non-radiative processes. The emitted photon has a longer wavelength (smaller energy) than the absorbed photon, due to the vibrational relaxation it undergoes. The difference between the adsorption and the emission peak of such a fluorescent molecule is a red shit, also called the Stokes shift.

Fluorescing molecules contain delocalized electrons that readily switch between the molecular energy states. Therefore, they are most often aromatic or conjugated molecules. Some molecules are auto-fluorescent and can be used as such in fluorescence-based techniques, while others are

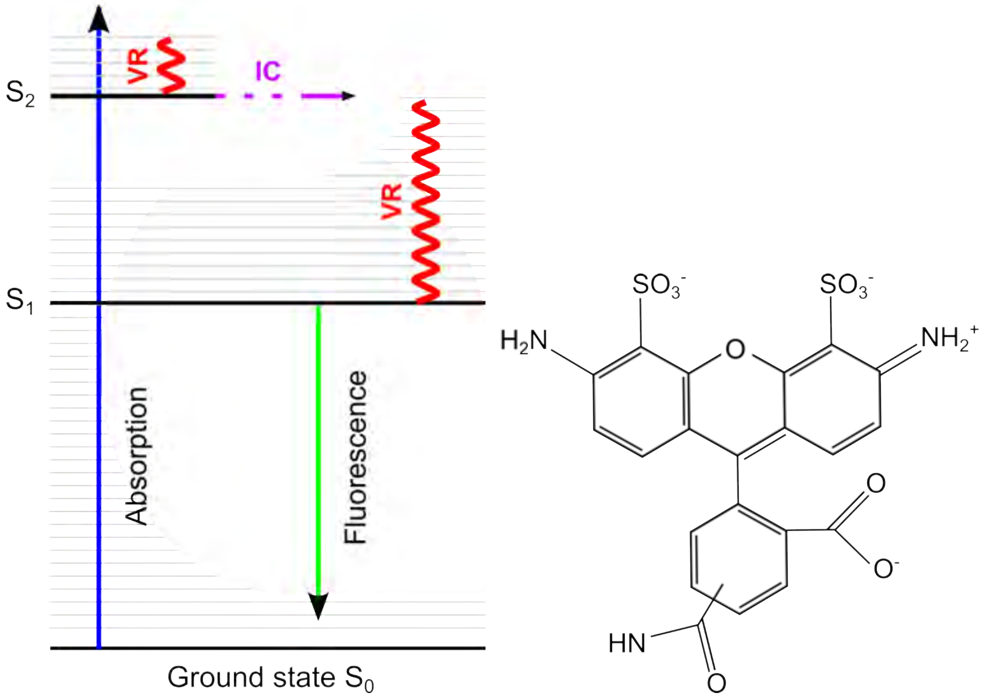

(a) (b)

Figure 2.7: (a) Fluorescence principle according to the simplified Jablonski diagram with VR the vibrational relaxation and IC the intersystem crossing (non-radiative) in (b) the molecular structure of the Alexa 488 fluorphore.

labeled with a fluorescent dye in order to be able to detect them. The aforementioned Stokes shift is a very convenient property of fluorescence because it allows fluorescence-based techniques to differentiate between excitation light and emission light. The molecular structure of the fluorescent molecule of interest, Alexa-488, is shown in Figure 2.7(b).

For fluorescence measurements the samples of interest were mounted on an adapted microscope slide and placed on the stage of a Zeiss LSM 510 meta confocal microscope (Jena, Germany). Confocal microscopy offers major advantages over conventional wide-field fluorescence microscopy. It eliminates/reduces the background information from above the focal plane. This allows a high signal to noise ratio and creates high-quality fluorescent images. The detection pinhole blocks most of the light that is not coming from the focal plane. This leads to sharper images compared to traditional fluorescence microscopy (Figure 2.8) and allows one to obtain images at various z-axis planes (i.e. a z-stack) of the sample.

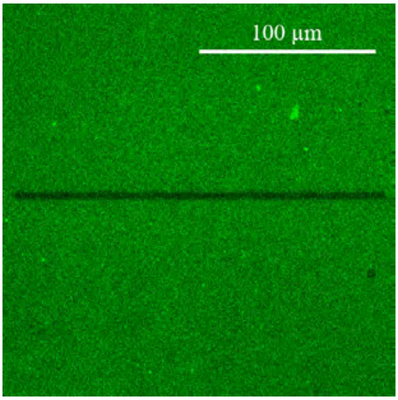

Figure 2.8: An example of a typical confocal image of a surface covered with fluorescent labeled biomolecules, the black line is a bleach line which proves fluorescence and provides a useful tool for normalization.

In Figure 2.9 a schematic representation is shown of the confocal setup. This CFM is equipped with a 30 mW air cooled argon ion laser, which was set at 45% of its maximum power (this corresponds to a tube current of 5.7 A). The fluorescent labeled molecules were excited with the 488 nm line of this laser (selected by a 488 10 nm interference-based laser cleanup filter, Omega Optical, Brattleboro, VT, USA) under the control of an AOTF. After passing a 0.6 neutral density filter (25% transmittance), the excitation light was directed to the sample via a dichroic mirror (DIC) (HFT 488) and a Zeiss EC Plan-Neofluar 10x/NA objective. The DIC separates the light mixture by reflecting the laser light and only allowing the emitted fluorescence light to go through.

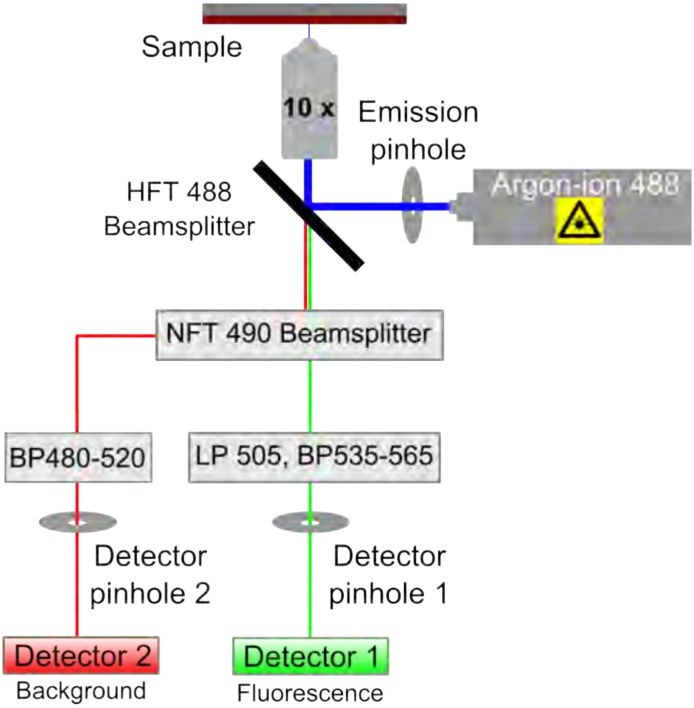

Figure 2.9: Schematic representation of the confocal fluorescence microscopy. Note the microscope is inverted so the sample faces downward.

The fluorescence collected by the objective was transmitted through the DIC and through a LP505, BP535-565 or BP500-520 nm emission filter to a photomultiplier tube. 2 detectors were used, one for the fluorescent signal and another to image the background by recording the reflection. Images were collected using the AIM Zeiss software. The zoom factor was set to 1 or 4 resulting in 920 × 920 μm^2 and 220 × 220 μm^2 images respectively. Photomultiplier gain and signal amplification were adapted in order to have a sufficiently high signal. All images were recorded at 10% of the acousto-optic tunable filters (AOTF) transmission (±30 μW at the sample position) to avoid bleaching during the acquisition. For bleaching, a rectangular ROI was defined. The bleaching was performed by 10 scans of the region of interest (ROI) with the AOTF transmission set to 100%. Out-of-plane fluorescence was reduced as much as possible by setting the detection pinhole to 1 airy unit (90 μm diameter). If fluorescence was quantized it was always using the same measurement parameters and the signal was normalized versus the bleached line. The brightness of the resulting image pixels corresponds to the relative intensity of detected fluorescence light. Slower scans yield a better signal to noise ratio (S/N ratio), which in turn leads to a better contrast.

2.4.3 Enzyme Linked Immunosorbent Asasy (ELISA)

ELISA, also known as an enzyme assay, is a biochemical diagnostic technique mainly used in immunology to detect the presence of an antibody or antigen in a sample. It also requires biofunctional activity of the receptors. Typically an ELISA is performed in a 96 well polystyrene plate. For diamond application an adapted ELISA protocol was developed. First, capture antibodies were adsorbed (20 nM) at 37°C for 2 hours. Next they were blocked overnight with 6w% BSA in 1 × PBS at 4°. After 2 × washing the CRP target analyte was added, this in various concentrations. The mixture was left allow complex formation between the capture antibodies and the pentameric CRP protein. Up to this point the procedure was label-free. ELISA is based on a colorimetric reaction so a secondary antibody labeled with an alkaline phosphatase (AP) was added. This 2^{nd}-Ab-AP was added to reach a concentration of 70 nM and incubated for an hour. The AP creates an amplification system based on NADPH. This substance is transformed by AP to NADH, which is the substrate for a secondary enzymatic redox cycle. Diaphorase oxidizes NADH to NAD+ while reducing a tetrazolium salt to an intensely colored formazan dye. Subsequently, while ethanol is oxidized by alcohol dehydrogenase, NAD+ is again reduced to NADH, driving the cyclic behavior of the amplification reaction. After several minutes, the reaction liquid was removed from the surface of the NCD samples with a micropipette, and transferred into the wells of a microtiter plate. This microtiter plate was subsequently placed inside an ELISA reader, and the absorption of the colored product was measured at 405 nm.

2.5 Electrochemical techniques

2.5.1 Electrochemical Impedance Spectroscopy (EIS)

The complex impedance spectroscopy (IS) was first applied in the field of electrical engineering in the early 1880's [80] because it allows studying of electro(chemical) properties of materials. There are 2 main categories of impedance spectroscopy : Electrochemical IS (EIS) and everything else! EIS involves measurements and analysis of materials in which ionic conduction strongly predominates. Examples of such materials are solid and liquid electrolytes, fused salts, ionically conducting glasses and polymers, and non-stoichiometric ionically bonded single crystals, where conduction can involve motion of ion vacancies and interstitials. The remaining category of IS applies to dielectric materials: solid or liquid non-conductors whose electrical characteristics involve bipolar rotation, and to materials with predominantly electronic conduction.

In this thesis EIS is used for thorough characterization of electrode materials. Another important, and major employment of EIS is the label-free readout of biosensors which is the main topic of this dissertation. The advantages of EIS far surpasses the drawbacks. EIS allows careful signal analysis via a non-destructive way about 'black-box' systems containing resistors, capacitors and (hopefully no) inductors. Also the technique is straightforward, fast, easy to miniaturize, it allows real-time information and can be applied in almost any sensor application. A minor drawback is the signal interpretation, i.e. the smallest molecular events that occurs at

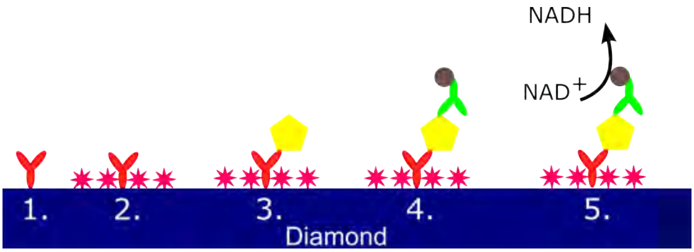

Figure 2.10: Schematic representation of an ELISA amplification assay on diamond. In 1. the primary receptor is added, 2. is BSA blocking, 3. is the addition of the antigen, 4. the secondary antibody and 5. the conversion of NADH to NAD+ followed by the color reaction.

an interface can cause changes in an impedance spectrum. Therefore, it is of key importance to understand the basic principles of the technique and the electrode behavior. There is also need for sensor optimizations before conclusions can be made. Also one should always keep in mind that no two systems are the same, and that EIS is sensitive to even the smallest changes [81].

The power of time resolved impedance with the careful modeling of the spectra at certain intervals can reveal and explain the events that take place at the electrode/sensor interface. EIS can be used in simple liquid cells with a 2 electrode configuration which represent the working and counter electrode. This setup allows easiness of implementation for sensor applications. However, as soon as there are charge transfers (faradaic currents) occuring it is of great importance that there should be an additional reference electrode (Silver/SilverChloride (Ag/AgCl), Standard Hydrogen Electrode (SHE) or Calomel electrode) for proper signal acquisition and interpretation. It is also important to use noble electrode materials (such as gold or platina) to avoid any Galvani potentials. When two electrodes are submerged in an electrolyte, electrons will flow from the metal with a lower work function to the metal with the higher work function until an equilibrium is reached. This effect could cause an offset to the impedance signal that leads to misinterpretation of data.

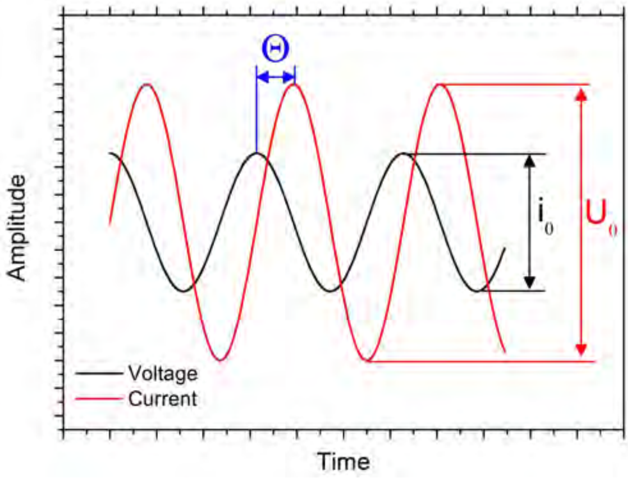

Figure 2.11: Voltage and current signals from an impedance measurement with a difference in amplitude and phase shift.

As mentioned before, a small alternating sinusoidal voltage U_0 of a given frequency and amplitude is applied to a system and the response current I_0 is monitored (Figure 2.11). The resulting current through the system is measured as a function of time, and the phase shift θ relative to the input signal is determined. This procedure is repeated at different frequencies, and the impedance |Z| can than in accordance with Ohms law be calculated as:

$$Z = \left(\frac{U_0}{I_0}\right) \tag{2.7}$$

The excitation signal, expressed as a function of time, has the form:

$$U_{(t)} = U_0 sin\omega t = U_0 e^{j(\omega t)} \tag{2.8}$$

With U_t the potential at time t, U_0 is the amplitude of the signal, and ω is the radial frequency. The relationship between radial frequency (ω) (expressed in radians/second) and frequency (expressed in Hz) is:

$$\omega = 2\pi f \tag{2.9}$$

In a linear system, the response signal, I_t is shifted in phase (θ) and has a different amplitude, I_0

$$I_{(t)} = I_0 sin\omega t = I_0 e^{j(\omega t+\theta)} \tag{2.10}$$

As mentioned in Eq. 2.7, Ohms law allows to calculate the impedance of the system as:

$$Z(\omega) = \frac{U_t}{I_t} = \frac{U_0 sin(\omega t)}{I_0 sin(\omega t+\theta)} = Z_0 \frac{sin(\omega t)}{sin(\omega t+\theta)} \tag{2.11}$$

The impedance is therefore expressed in terms of a magnitude, Z_0, and a phase shift, θ.
By using Eulers formula:

$$exp(j\theta) = \cos\theta + jsin\theta \tag{2.12}$$

It is possible to express the impedance as a complex function. The potential is described as:

$$U_t = U_0 exp(j\omega t) \tag{2.13}$$

and the current response as:

$$I_t = I_0 exp(j\omega t - \theta) \tag{2.14}$$

The impedance is then represented as a complex number:

$$Z(\omega) = \frac{U}{I} = Z_0 exp(j\theta) = Z_0(cos\theta + j\ sin\theta) \tag{2.15}$$

The impedance thus consists of a real part and an imaginary part where the real part is:

$$Re(Z) = Z = |Z|cos\theta \tag{2.16}$$

And the imaginary part is:

$$Im(Z) = Z = |Z|sin\theta \tag{2.17}$$

There are different ways to represent an impedance plot depending on the property of interest. The most common ways are the Bode and Nyquist plot. Besides those also the complex capacitance (C'/C"), complex admittance and the Cole-Cole plot exist. The Bode plot represents 2 graphs with the according frequency dependence. Here the phase (θ) and $\log_{10}$ of the modulus (|Z|) are plotted against the $\log_{10}$ of the frequency (Figure 2.12 (a)). From Eq. 2.16 and Eq. 2.17 can be seen that Z(ω) is composed of a real and imaginary part. When the real part is plotted (x-axis) against the negative of the imaginary part (y-axis) a Nyquist plot is obtained, shown in Figure 2.12 (b). Each point in the Nyquist plot is the impedance at a fixed frequency. For the electrochemical impedance spectroscopy data, where impedance usually decreases as frequency increases, low frequency data are on the right side of the plot and higher frequencies are on the left. The data can be represented as a vector of length |Z| and the angle between this vector and the x-axis is θ.

The impedance spectra in the previous Figure show a frequency dependent behavior. Depending on the frequency we focus on a different fraction of the biosensor.

The measured spectra can be fitted with an equivalent circuit consisting of the following components: resistors (R), capacitors (C), constant phase elements (Q,n) in case of non-ideal capacitors, inductors (L) and a diffusion limited resistance 'the Warburg' component (W). These elements and their impedance contribution are presented in Table 2.1. The chosen model must have physical meaning to the system [82]. The fitting

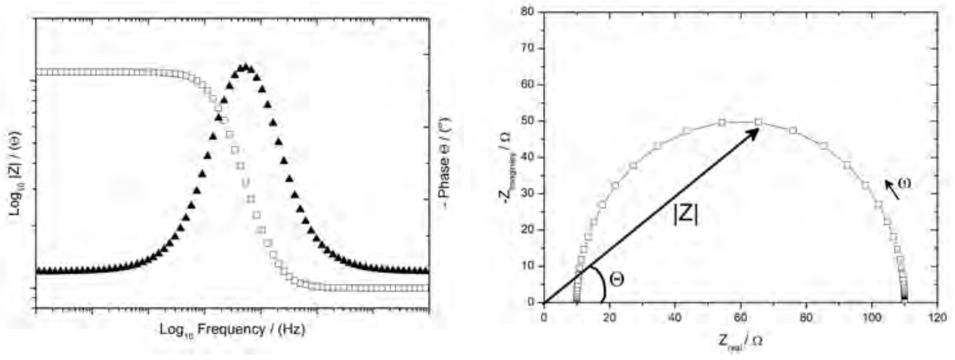

(a) (b)

Figure 2.12: (a) Typical Bode plot for a Randles cell, R(QR), with the modulus (|Z|) and phase (θ) plotted versus the frequency. (b) Nyquist plot of a typical R(QR) model. The length of the vector is modulus and the angle with the real-axis is the phase shift. Note that ω=2πf

was done by ZSimpWin V 3.21 (Princeton Applied Research, Tennessee, USA) which was based on an iterative least square fitting of the spectra using the chi-square (χ^2) for the entire model and the percent error values for each circuit component to determine the fit of a given model to the experimental data. The quality of the fit is determined by the χ^2 which represents the goodness of fit. According to literature a χ^2 of $< 10^{-3}$ is acceptable for a given model. However, many circuits can be fitted resulting in good χ^2's, but this doesn't mean that they are of application within the concept. Also, the addition of an extra component to the model can only be accepted if the χ^2 drops with one order of magnitude (Boukamp Theorem). The algorithm shown in Table 2.2 shows the calculation of the χ^2.

The spectra shown in Figure 2.12 are from a typical Randles cell shown in Figure 2.13 (b).The Randles cell consists of a series resistance (electrode, wiring, solution, . . .), R_s, a double layer capacitor, C_{dl}, and a charge transfer, polarization or double layer resistance, (R_{ct}, R_{pol},R_{dl}). The physical idea behind this theoretical model is the formation of a double layer at the (diamond) electrode/electrolyte interface as described in section 1.5.5. It is clear that if molecular events take place at this interface the double layer properties will change and will therefore cause changes in the

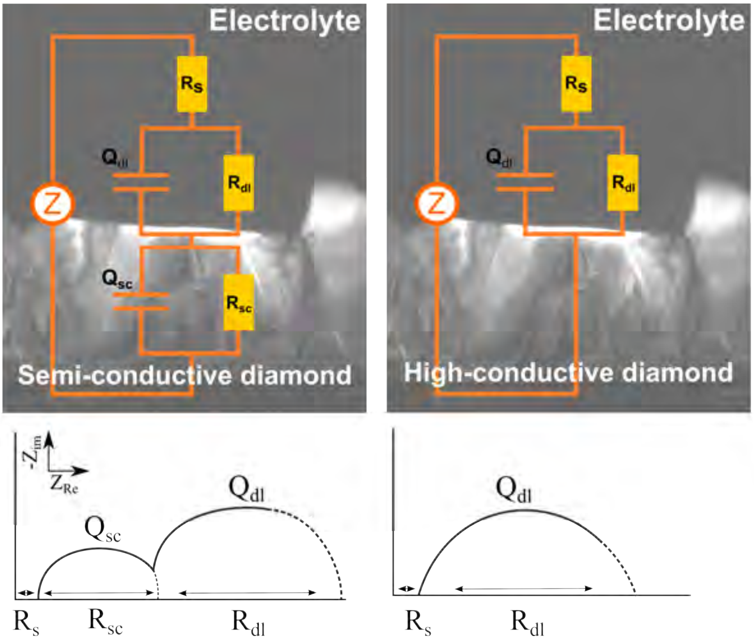

Figure 2.13: Cartoon of the equivalent circuit obtained on semiconducting diamond (cross-section) immersed in an electrolyte solution. With R_s the electrolyte resistance, Q_{dl} the double layer capacitance, R_{dl} the charge transfer, polarization or adsorption resistance at the interface, Q_{sc} the space charge capacitance and R_{sc} the space charge resistance.

impedance. In the case of diamond the Randles cell is only of application for highly doped diamond films in contact with an electrolyte. When semi-conductive diamond electrodes are used, an additional segment (QR) is added (shown in In Figure 2.13 (a)) to compensate for the band bending in the diamond film. Note, the band-bending is not influenced by morphological changes, as the double layer, but is sensitive to charges (see section 1.5.5).

Table 2.1: Components for equivalent circuit fitting

Component	Impedance	Info
R	Z_R	Resistor
L	$Z_L = j\omega L$	Inductor
C	$Z_C = (j\omega C)^{-1}$	Capacitor
Q	$Z_{CPE} = {Q_0}^{-1} (j\omega)^{-n}$	Constant phase element
W	$Z_W = {Y_0}^{-1}(j\omega)^{-0.5}$	Warburg component

.

Table 2.2: Equivalent modelling algorithm

Datapoints and parameters

1. Experimental data point (frequency, Z_{real}, Z_{imag} [ω_i, a_i, b_i]
2. Parameters associated with model,$\bar{p}$=(p_1, p_2,...,p_m)
3. Calculated point (ω_i, Z'(ω_i:$\bar{p}$), Z''(ω_i:$\bar{p}$))
4. Weighing factors[ω_i, W'_r, W''_r]

Application of statistics

The distance between experimental and calculated points,

$d_i^2 = (a_i - Z'(\omega_i:\bar{p}))^2 + (b_i - Z''(\omega_i:\bar{p}))^2$

The goodness of fit to model:

$\chi^2 = \sum_{i=1}^{n} \frac{(a_i - Z'(\omega_i:\bar{p}))^2 + (b_i - Z''(\omega_i:\bar{p}))^2}{\sigma_i^2}$, where n is the number of datapoints.

Weighting options:

Unity weighting, σ_i=f

Modulus weighting, $\sigma_i = \sqrt{a_i^2 + b_i^2}$

2.5.2 Cyclic voltammetry

Cyclic voltammetry (CV) is a potentiodynamic electrochemical measurement. A typical experimental setup consists of the following electrodes: a reference- (RE), working- (WE) and counter electrode (CE) (See Figure 2.14 (a)). In a CV the potential at the WE is ramped linearly versus the reference electrode, and the current is measured between the working and the counter electrode. The WE serves as the surface at which the electrochemical reaction takes place. It is of utmost importance that the electrode area has a controlled surface area for interpreting and comparing CV results. In any case it is best that the electrodes are inert conductive materials such as gold, platinum, etc. The supporting electrolyte needs to have an adequate conductivity for allowing charge transport to observe any electrochemical phenomena. The most common reference electrodes are the Saturated Calomel Electrode (SCE), the Normal Hydrogen Electrode (NHE) and the Silver/Silver Chloride (Ag/AgCl) electrodes. The Silver/Silver Chloride electrode (Ag/AgCl) can be easily miniaturized which makes it the most favorite electrode for integration in sensor systems. The actual recording of the i/V curves is done by cycling the voltage in function of time with a certain scanspeed. The resulting current is measured and also plotted in function the corresponding voltage. Which means, that when a redox-active species (such as $K_3Fe(CN)_6{}^{+3/+4}$) is used, a reversible electron transfer process should occur. If the a succesfull reversible cycle has taken place, a typical *'duck'* like figure should arise as shown in Figure 2.15. Normally cyclic voltammetry is used to study the electrochemical properties of an analyte in solution, but if a known analyte is used it can also be a characterization technique for different electrodes.

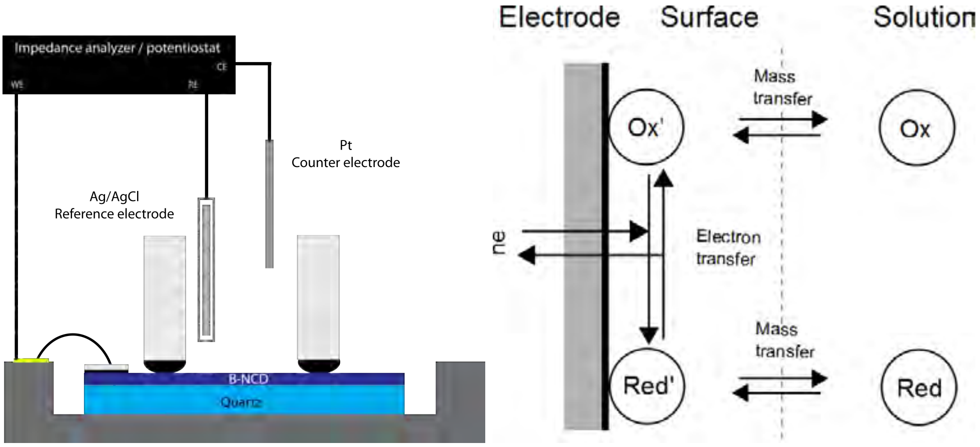

(a) (b)

Figure 2.14: In (a) a schematic representation is shown of a cyclic voltammetry setup and in (b) the principle of mass and electron transfer between the redox species.

The $K_3Fe(CN)_6{}^{+3/+4}$) redox couple is a single electron transfer reaction mechanism between the oxidized (O) and reduced (R) state.

$$O + e^- \xrightarrow{k_{red}} R \tag{2.18}$$

$$R \xrightarrow{k_{ox}} O + e^- \tag{2.19}$$

The current flowing in either the reductive or oxidative steps can be predicted using the following expressions:

$$i_O = FAk_{ox}c_R \tag{2.20}$$

$$i_R = -FAk_{ox}c_O \tag{2.21}$$

For the reduction reaction the current i_R is related to the electrode area A, the surface concentration of the reactant C_O, the rate constant for the electron transfer k_{red} and Faraday's constant F. This is similar for the oxidation. By definition the reductive current is negative and the oxidative is positive. The total electrolysis is not only dependent on the rate constant but also on the mass transport that is dominated by diffusion (Figure 2.14 (b)). The current that originates from the redox reactions can only be maintained if the supply of 'fresh' species from the bulk towards the interface is maintained. So if larger concentrations are used, a larger entropic force is present resulting in a larger diffusion coefficient and therefore also in a larger anodic or cathodic current.

2.6 Diamond growth

Diamond growth was carried out in an ASTeX 6500 series (MPECVD) reactor on an electronic isolating fused silica or conductive Si (100) (1-20 Ω· cm) substrate which was treated with a colloidal suspension of 5 to 10 nm detonation diamond. The temperature was monitored by a Williamson Pro92 dual wavelength pyrometer. Growth was performed in a CH_4/H_2 plasma with methane concentrations between 0.5 to 5%. Doping was induced by trimethyl boron gas ($B(CH_3)_3$) with a 800-7000 ppm boron concentration for all samples. The substrate temperature was 700°C induced by 3500 W of microwave power and a total pressure of 33 hPa. The growth was stopped when the B:NCD layers reached a thickness of 150 - 200 nm and cooling after growth was done under hydrogen. During growth the thickness was monitored by a 20 mW laser based interferometer from Altechna operating at a wavelength of 473 nm. Diamond hydrogenation was done in a H_2 plasma (50 Torr, 800°C, power 4000 W, duration of 1 min)

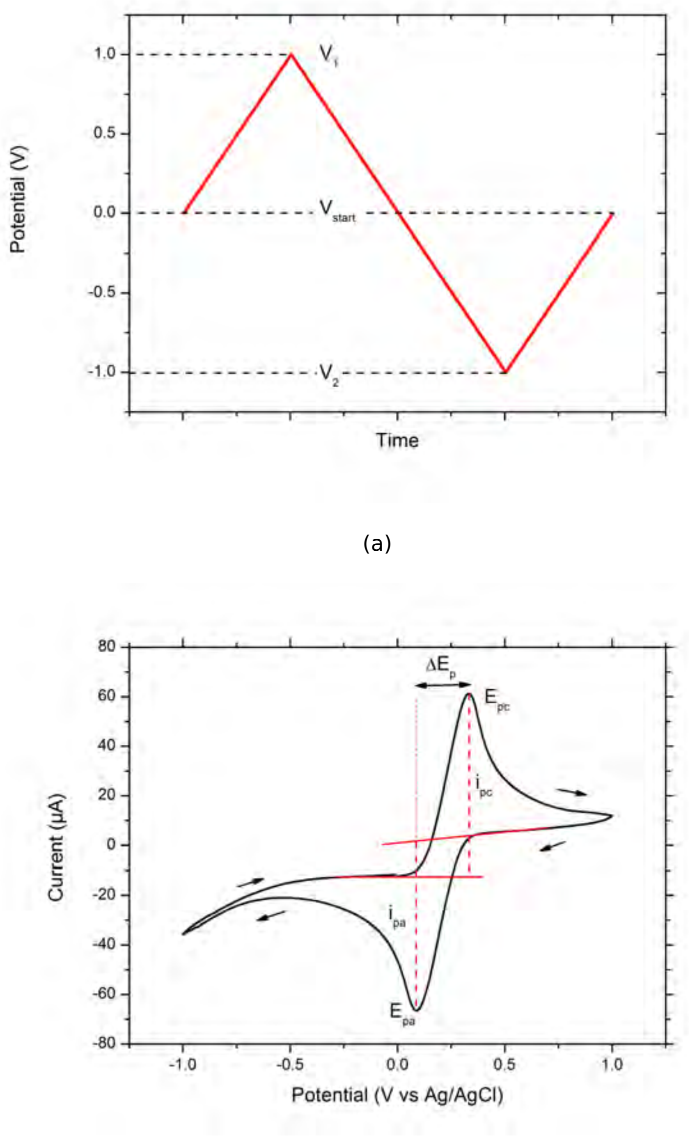

(a)

(b)

Figure 2.15: Working principle of a CV measurement. The potential is swept versus the time (a) and the according current is recorded. (b) shows the typical 'duck-like' voltammogram for a 10 mM (b) shows the typical 'duck-like' voltammogram for a 10 mM $K_3Fe(CN)_6^{+3/+4}$ in 1 × PBS at 25°

Chapter 3

Diamond: an ideal electrode material

3.1 Diamond as an electrode in aqueous solutions

In the following sections the use of diamond as an electrode for electrochemical applications is discussed. First, a brief motivation is given why diamond is interesting and further on improvements are shown of traditional metal electrodes. Pleskov et al introduced in 1987 doped-diamond into electrochemistry [83]. Since then, the largest potential window measured in aqueous solution is up till now attributed to diamond [84, 85].

3.1.1 Diamond compared to other electrodes

In comparison to other electrodes, diamond has by far the most improved electrochemical performance. In cyclic voltammetry it shows a minimal background current, little ionisable or redox active groups on the surface and stable electrode properties which make it an ideal candidate for electrochemical applications. In contrast to diamond, many (metal) electrodes cause early hydrogen and oxygen evolution to kick in, resulting in a small potential window when measuring in aqueous solutions [83]. To further

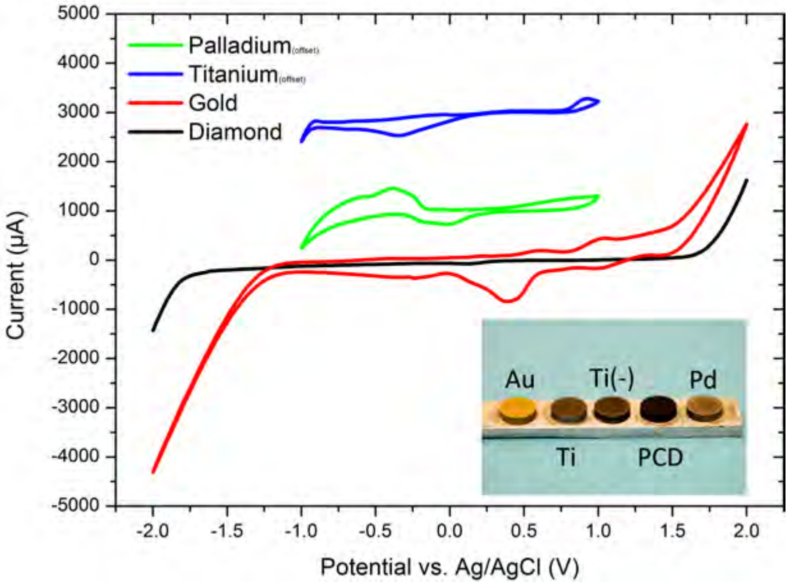

Figure 3.1: Cyclic voltammetric i-E curves of 4 different electrode materials i.e. Palladium, Titanium, Gold and diamond. The Ti(-) reference had a similar behavior as the other Ti electrode and is not shown. The recordings were made in 1 × PBS at pH 7.4 with a scanspeed of 100 mV/s.

clarify this, a comparison was made between different electrode materials (palladium (Pd), titanium (Ti) and gold (Au)). After metal deposition and diamond growth, all of the electrodes were first 1 hour oxidized via uv-ozone and immediately afterwards the i-E curves were recorded in 1 × PBS. The results are shown in Figure 3.1. The palladium (Pd), titanium (Ti), reference titanium (Ti-, no uv-oxidation) and gold (Au) all have multiple large peaks caused by faradaic currents that are intrinsic to the material itself and are therefore detrimental for electrochemical applications. The diamond coated electrode stands out and resulted in a unique, extremely uniform and symmetrical shape. No faradaic currents were observed in the potential window of -1.75 to 1.75 V which is significantly larger and better than the other electrodes proposed here. These results trigger the interest to apply diamond coatings on various electrodes to improve their electrochemical properties.

3.1.2 Coating metal electrodes with diamond improves electrochemical properties

Regarding the drawbacks of metal electrodes shown in Figure 3.1, there is a need to create ideal electrodes for a whole range of applications ranging from in vitro cell studies, nerve stimulation to pacemaker leads. In the scope of these projects the following experiments were done:

- Coating of PlatinumIridium (PtIr) electrodes with B-doped μCD (B-μCD) and monitor their electrochemical behavior for *in vitro* / *in vivo* applications

- Coating of various thin metal wires for applications in cardiac stimulation electrodes

Currently the PtIr electrodes were used for nerve stimulation but they have the potential to become in vivo implants. Of course, there is first need for $in-vitro$ cell culture studies. Here it is important to have a broad potential window without faradaic currents related to the hydrolysis of the aqueous solution nor possible electrode oxidation. When oxygen or hydrogen is formed, the pH shifts to non-physiological conditions causing cell death. Therefore, the PtIr electrodes were measured by EIS and CV before and after diamond coating. In Figure 3.2 (a) a SEM recording is shown of a PtIr mini-electrode coated with a thick, heavily boron doped polycrystalline diamond film (inset). The i-E voltammograms before and after coating are shown in panel (b). It is clear that the bare PtIr electrodes have an improved behavior compared to the other metallic electrodes discussed in Figure 3.1, but still have increasing currents in a large potential window. The diamond coated electrodes behave as expected, with a very low background current (nA) in a larger potential window. From fitting EIS measurements (results not shown) with the typical Randles cell an interface capacitance of 52.1 μF was obtained for the bare electrode and 2.5 μF for the diamond coated electrodes. It was observed in all impedimetric diamond measurements throughout the thesis that diamond electrodes have a typical smaller double layer capacitance compared to metallic electrodes.

The second was the electrochemical study of various wire electrodes coated with diamond for biomedical applications. Here, only the result of a 0.25 mm titanium wire is discussed. Figure 3.2 (c) shows a SEM recording of the wire tip and the inset focusses on the NCD film. Again the i-E curves before and after coating are recorded (panel d). The bare titanium electrode

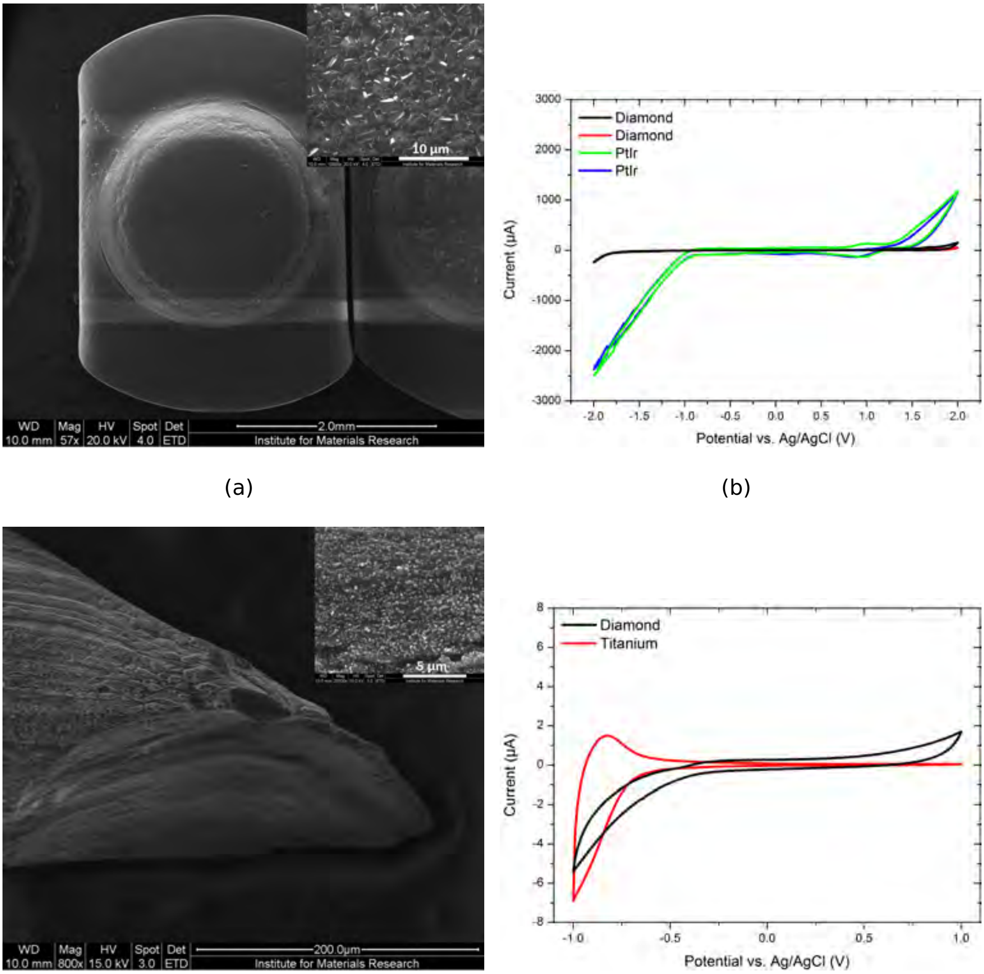

(a) (b)

(c) (d)

Figure 3.2: In (a) a SEM recording of the PtIr microelectrode substrate coated with B-μCD. The inset shows the morphology of the surface. In panel (b) cyclic voltammetric i-E curves are shown of the PtIr electrode before and after coating. Panel (c) a SEM recording of the thin Ti wire electrode, also here the inset focusses on the NCD film. Panel (d) shows cyclic voltammetric i-E curves before and after titanium coating. Recordings were made in 1 × PBS at a scanrate of 100 mV/s.

has a clear cathodic shoulder at -0.9V which disappears completely after diamond coating. EIS spectra (results not shown) revealed that the bare titanium suffered from oxidation and that after coating these adverse effects disappear. Regardless the insulating properties of intrinsic diamond, these electrodes and coatings find their interest in biomedical applications rather than electrochemistry.

3.1.3 Superior diamond electrodes for electrochemical sensing

Here high quality μCD electrodes were grown with a high boron doping (5000 ppm). A SEM recording in Figure 3.3 (a) shows the large diamond grains (> 500nm). When measuring with hydrogenated diamond in aqueous solutions and applying a large potential window (>3V) the surface becomes anodically oxidized. In Figure 3.3 (b) a nice contrast is given between the hydrogenated surface and locally oxidized area. According to literature even electrochemical hydrogenation can be performed in acidic environments [86].

The surface termination and contaminations of diamond electrodes are also important to take into consideration. In Figure 3.4, two different voltammograms are shown with panel (a) recorded in 1 × PBS and panel (b) recorded in 1 × PBS with 10 mM $K_3Fe(CN)_6{}^{-3/-4}$. In both figures there is a comparison made between "as-grown" (hydrogenated) and thoroughly oxidized diamond. In panel (a) the as-grown diamond shows an anodic peak peak around 1.1V resulting from the oxidation of non-diamond carbon impurities at the surface presumably forming a variety of carbon-oxygen functionalities. Also the as-grown result from panel (b) has additional (unwanted) peaks. It is clear that hydrogenated diamond favors the electrode transfer and therefore resulting in larger anodic I_{pa} and cathodic

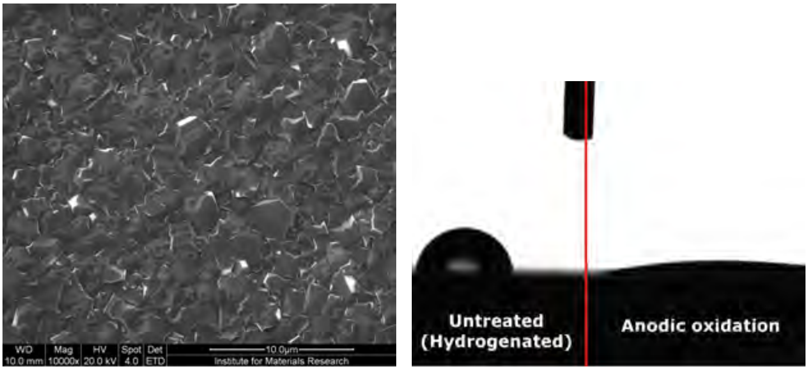

(a) (b)

Figure 3.3: In (a) a SEM recording of a μCD film is shown and in (b) the contact angle of MilliQ water on the same film which is hydrogenated (left) and (locally) anodically oxidized on the right by cyclic voltammetry

currents I_{pc}. After oxidation the anodic peaks from panel (a) disappeared and the voltammogram from panel (b) now only shows a typical single electron transfer voltammogram. The oxidized surface however results in a slightly less favorable electrochemical electrode due to the reduced currents but it has still very stable and reversible voltammograms. From this we learn that it is better to oxidize the diamond prior to use to reduce surface contaminations as much a possible.

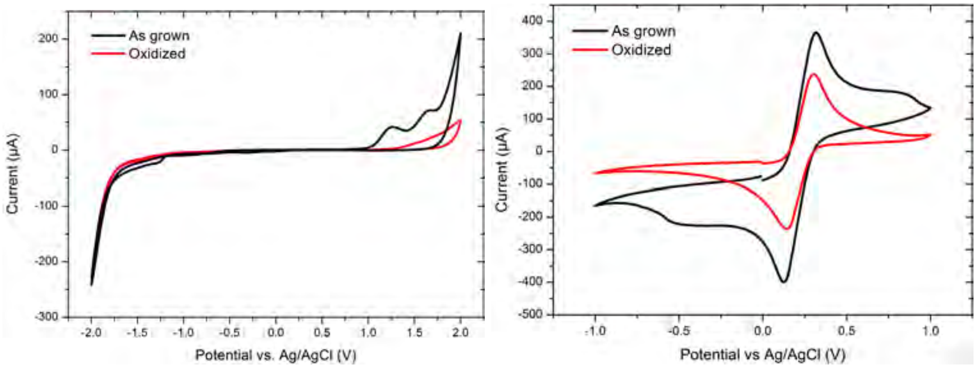

(a) (b)

Figure 3.4: Cyclic voltammetric i-E curves for (a) a high quality diamond recorded in 1 × PBS. In (b) the same diamond film as in (a) but now a $K_3Fe(CN)_6$ redox couple was added. Scan rate 100 mV/s

If not mentioned otherwise the standardized measurement conditions were 1 × PBS with 10 mM $K_3Fe(CN)_6$ as a redox mediator at pH 7.4 at 30°C. The electrochemical behavior of μCD electrodes was further studied by varying the following measurement conditions.

- Concentration of the supporting electrolyte (0.1× to 10×PBS
- Temperature (20 to 40°)
- Concentration redox agent (1 μM to 0.1 M)

By increasing the ionic concentration of the supporting electrolyte (Figure 3.5 (a)) the charge transport originating from the redox species is also improved. Two significant effects can be seen, the first is the increase in anodic (i_{PA}) and cathodic (i_{PC}) peaks and the second is the decrease in peak separation (ΔE_p). Both effects indicate a positive effect on the

charge transfer and electrode kinetics.
A perfect, reversible redox system fulfills the following requirements:

- $\triangle E_p = E_{pc} - E_{pa} = 58/n$ mV
- The peak current ratio = $i_{PA}/i_{PC} = 1$
- The peak current function $i_P/v^{0.5}$ has a linear relation (v = scan rate)

For the high quality diamond films we measured peak current ratio's reaching unity. A linear relation between the anodic and cathodic peak currents in function of the scanrate was observed (Figure 3.5 (b)). Even peak separations up to 80 mV for 10 × PBS were measured. From this we learn that the supporting electrolyte is of utmost importance to improve the electrochemical performances! In literature, CV experiments were done in a wide variety of supporting electrolytes such as LiCl, KCl, H_2SO_4 etc. These result in even better voltammograms, but with the scope of biomedical related applications it is of key importance to understand the behavior of electrodes under physiological conditions and therefore our focus remains on 1×PBS as supporting electrolyte.

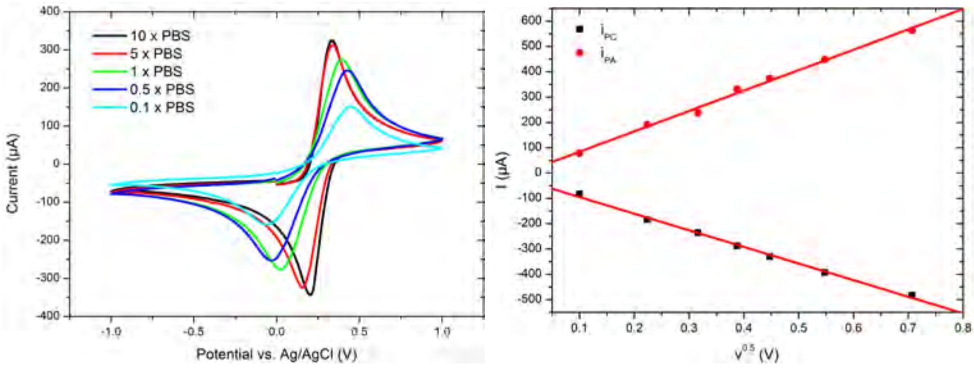

(a) (b)

Figure 3.5: In (a) a dose response curve of the anodic current for various $K_3Fe(CN)_6$ concentrations. (b) shows cyclic voltammetric i-E curves of different temperatures. The supporting electrolyte is 1×PBS with a scanrate of 100 mV/s.

By using various concentrations of the redox couple in 1 × PBS, the currents vary largely and a dose response curve for the i_A is obtained (Figure 3.9 (a)). The limit of detection for this outer shell single electron transfer redox couple $Fe(CN)_6^{-3/-4}$ was found to be in the range of 10 to 100 μM. The effect of increasing the temperature enhances the diffusion, and therefore the transport of fresh redox species to and from the electrode interface increases, resulting in higher anodic and cathodic peak currents (Figure 3.9 (b)).

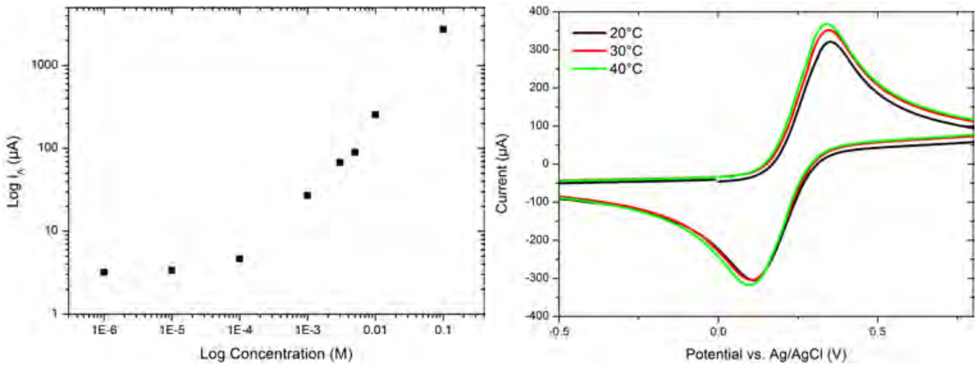

(a) (b)

Figure 3.6: Behavior of the voltammograms with different concentrations of supporting electrolytes (a) and a dose reponse curve for the redox couple concentration (b).

In addition, efforts were made to employ these μCD diamond electrodes for immunosensing using cyclic voltammetry. In Figure 3.7 the i-E curves are shown. The background was recorded in 10 mM $Fe(CN)_6^{-3/-4}$ with 1 × PBS as supporting electrolyte and after a stable signal was obtained, 20 nM antibodies were added. After addition, the anodic and cathodic current dropped together with an increase in ΔE_p. This indicates that the adsorbed antibodies form a blocking layer at the electrode interface which impedes charge transfer across the interface. The increase in ΔE_p is due to deterioration of the rate constant and therefore also loss in good electrode kintectis. After 40 minutes of adsorption, 100 nM antigens, CRP, were added. Hereafter, no additional changes were observed in either the peak currents nor ΔE_p. This indicates that when the entire surface is blocked, the charge transfer and electrode properties were no longer influenced by additional changes on the molecular layer, such as antigen binding.

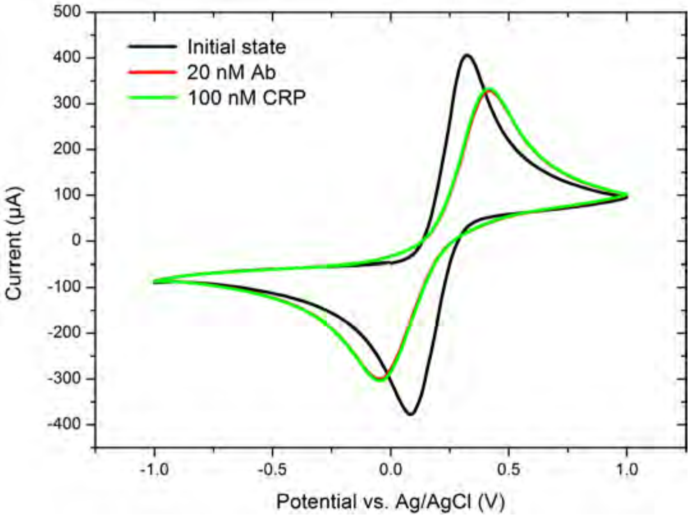

Figure 3.7: Cyclic voltammetric i-E curves of the in situ measurement of the initial state (black), immobilization of the receptor layers (red) and the addition of the CRP (green).

3.1.4 Conclusion

In the previous subsections we discussed the use of diamond as coating layer on metal electrodes to improve their electrochemical properties. They were characterized by scanning electron microscopy, cyclic voltammetry and electrochemical impedance spectroscopy. Especially the use of CV does not only provide usefull electrochemical information but serves also as a benchmark technique to inspect the film quality. We also found that surface contaminations are detrimental for electrochemistry and that all diamond samples are hence forth oxidized prior to electrochemical measurements.

The use of high quality boron doped μCD approaches an ideal reversible reversible system. However, from biosensing point of view, cyclic voltammetry does provide information about protein adsorption and the blocking of the surface impeding charge transfer but up till now, no evidence of antibody antigen binding was measured.

Note, the cyclic voltammetry is a very easy setup when working with commercial electrodes, but when custom made electrodes with different geometries were used, it became an engineering challenge for the succesfull packaging to obtain a correct and noise-less read-out. As additional information we devoted an appendix on different solutions to these read-out problems, they can be found in Appendix **??**

3.2 Electrochemical properties of variations in [C/H]-ratio.

In the following section different nanocrystalline diamond samples were used, grown under different conditions. The boron/methane ratio ([B/C]-ratio) was kept constant (5000 ppm) whilst the methane/hydrogen ratio was varied systematically between 1 and 5% ([C/H]-ratio). Janssen et al proved that small variations in grain size causes significant changes in mobility and resistivity [87, 31]. Therefore, we used the same diamond substrates to study if there was a relation between the morphological variations and the electrochemical behavior of these electrodes using impedance spectroscopy and cyclic voltammetry.

3.2.1 Experimental

All the diamond samples were grown with a boron content of 5000 ppm and the [C/H]-ratio was varied between 1 to 5%.

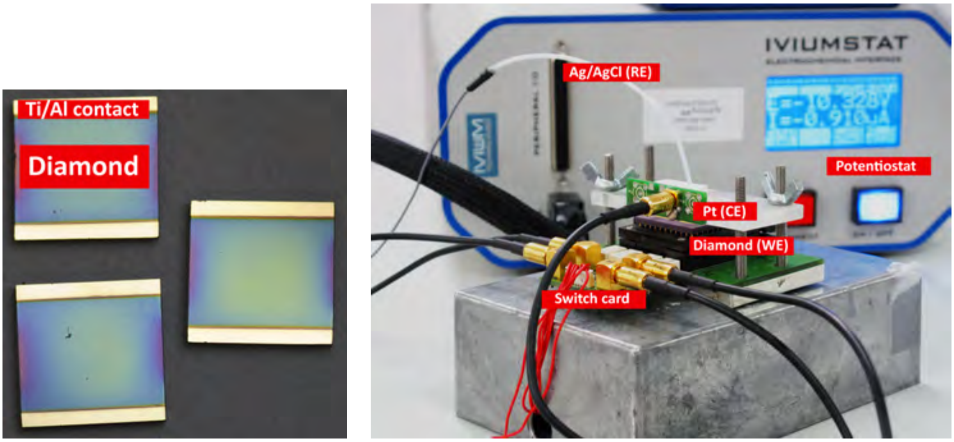

(a) (b)

Figure 3.8: Photographs (a) of the contacts on the diamond samples. The blue color originates from the high boron content. In panel (b) the electrochemical setup is shown. With a Pt wire as counter electrode (CE), Ag/AgCl as a reference electrode (RE) and the diamond film as the working electrode (WE)

Afterwards the samples were provided with ohmic Ti/Al contacts (20/150 nm) as shown in Figure 3.8 (a). Next the samples were thoroughly oxidized for 2 hours in an uv-ozone system. Afterwards they were packaged in a PGA socket (Global Chip Materials, USA) and wirebonded. A fluid cell was mounted on top with a capacity of 130 μl. Figure 3.8 shows in panel (a) the diamond samples with Ti/Al contacts and in panel (b) the packaged sample in the electrochemical setup. Electrochemical measurements were measured with an electrochemical potentiostat capable of measuring cyclic voltammetry and electrochemical impedance spectroscopy (Ivium, Eindhoven, Netherlands). Measurements were carried out with a conventional three-electrode setup, which included a Pt wire (Goodfellow, England) as a counter electrode (CE) and an Ag/AgCl reference electrode (RE) (Dryref, Precision Instruments, USA). The diamond film served as the working electrode (WE). EIS and CV were done with the Iviumstat Electrochemical impedance analyzer (Ivium, Netherlands). EIS measurements were performed between 10 mHz and 100 kHz with a V_{osc} of 50 mV in 1 × PBS at pH 7.4 as the supporting electrolyte. Cyclic voltammetry was performed with a 10 mM $K_3Fe(CN)_6$ redox mediator in 1 × PBS in a potential window of -0.8 to 0.8 V with scan rates of 10, 20, 50, 100, 200 mV/s. All measurements were performed in a temperature controlled incubator (Binder, Germany) at a constant temperature of 30°C if not mentioned otherwise.

3.2.2 Results

Electrode characterization

All of the used NCD films had an uniform film thickness of 150 nm ± 15nm and were all grown with the same Boron/Carbon-ratio [B/C]-ratio (5000 ppm). The only parameter that changed between the samples was the [C/H]-ratio.

The samples were grown by linearly increasing [C/H] from 1% to 5% in order to create grain sizes of decreasing dimensions. The average grainsize decreased from 67 nm for the 1% to 47 nm for the 5% respectively. The samples will therefore also be denoted according to their [C/H]-ratio, i.e. 1%, 2%, 3%, 4% and 5% respectively. Figure **??** shows only the 1% and 5% sample. With the scale bar at 1 μm, clear differences can be seen in the size of the diamond crystallites.

In Figure 3.10, Raman spectra of the 5 different diamond samples are

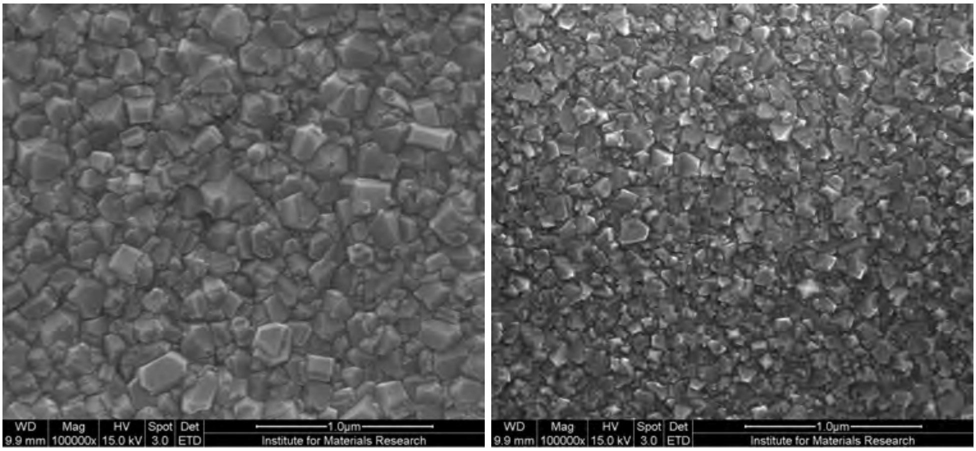

(a) (b)

Figure 3.9: SEM recordings of (a) the 1% NCD sample with an average grain size of 67 nm and in panel (b) the 5% sample with an average grainsize of 47 nm.

shown. Because Fanon resonance is a problem with boron doped diamond, exactly the same diamond samples were grown without boron to indicate the relation between the sp^2/sp^3 content. The clear and sharp peak at 1332 cm^{-1} is related to the sp^3 carbon contribution (P3); the peak at 1582

Table 3.1: Summary of the main morphological characteristics of the B:NCD films as a function of the C/H-ratio. The grain sizes are calculated from XRD spectra and the roughnesses are calculated from AFM measurements (results adopted from [31].

C/H-ratio (%)	Resistivity *mΩ cm*	Grain Size (nm)	Roughness (nm)
1	4.6	67	18.4
2	5.1	61	15.3
3	6.4	50	13.2
4	6.7	54	12.0
5	7.5	47	8.2

cm^{-1} can be attributed to the graphite G-band (P6). At last, the broad peak appearing as a 'shoulder' at 1350-1360 cm^{-1} can be attributed to the disordered sp^2 carbons which give rise to the graphite D-band peak. The point of interest is the ratio between P3 and P5,P6. The larger

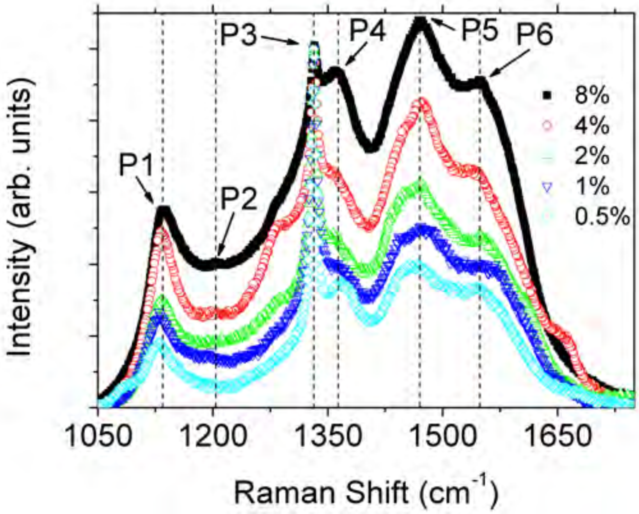

Figure 3.10: Raman spectra of NCD samples with different [C/H]-ratio. The ratio between P3 and P5 is a measure for the sp^2/sp^3 content. Source:[31]

Non-Faradaic processes

With impedance spectroscopy the current response of an electrical circuit to an alternating potential input is measured. The system was composed of the working electrode (B-NCD:O), the electrolyte solution (1 × PBS at pH 7.4 and 30°C), a platinum wire serving as a counter electrode and an Ag/AgCl as reference electrode. First, a control experiment is shown that serves a starting point for further understanding of the diamond electrode behavior. Here, a sputtered platinum film electrode was used, with the same dimensions as the B-NCD films. Figure 3.11 shows a typical Bode plot of a platinum film serving as a working electrode (note: WE: Pt, RE: Ag/AgCl and CE: Pt). The experimental data was fitted with the Randles model (Figure 3.12 (a)) and a good χ^2 of 1.4×10^{-4} was obtained, indicating a proper fit between the theoretical model and the physical system.

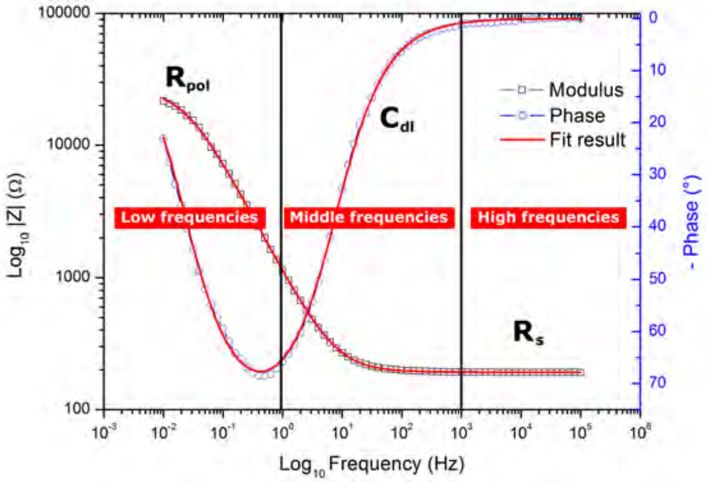

Figure 3.11: Bode plot of a Platinum film serving as a working electrode in the electrochemical setup. The experimental data was fitted with the Randles model R(QR). The spectrum was decomposed into three regions to serve as a starting point for further understanding.

To further understand the model the Bode plot will be divided into 3 regions i.e. the low (< 1Hz), middle (1 Hz to 1 kHz) and high frequencies (> 1kHz). Each domain is dominated by a certain component of the equivalent model. In the high frequencies, the modulus mainly represents the series resistance (R_s), only when the phase approaches 0°. When the frequency decreases, the phase starts to drop and directly proportional the modulus starts to slope upward to reach a higher impedance value corresponding to the polarization resistance (R_{pol}) located in the low frequencies. The decrease of the phase angle in the middle frequencies, indicates a capacitive behavior that originates from the electrode/electrolyte interface (see section 1.5.5). However, the applied circuit deviates slightly from the original Randles model. Here, the perfect capacitor is replaced by a Constant Phase Element (CPE). In nearly all electrolyte/electrode systems the CPE is used to account for frequency dispersion of the double layer capacitance.

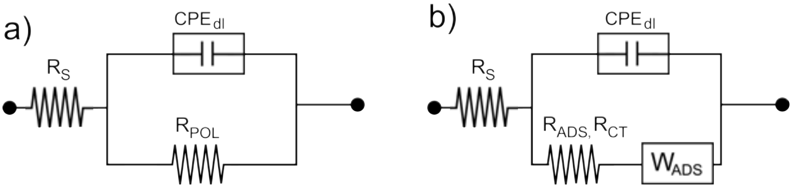

Figure 3.12: Equivalent models for electrode/electrolyte systems. (a) the typical Randles model and in (b) an adjusted model with a Warburg component to compensate for diffusion and adsorption effects.

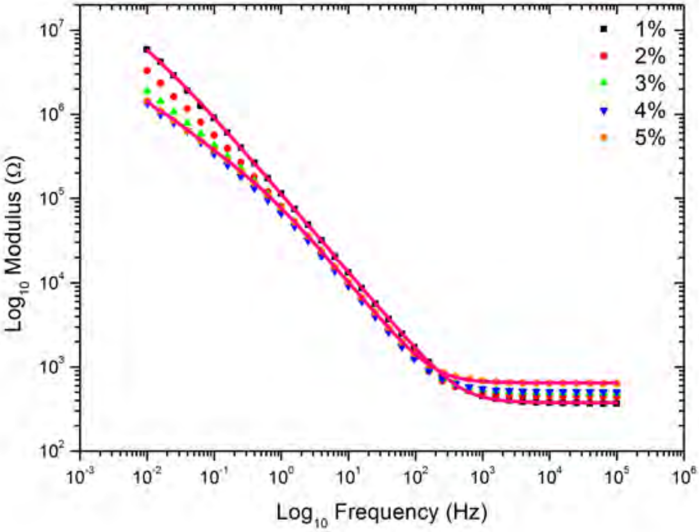

(a)

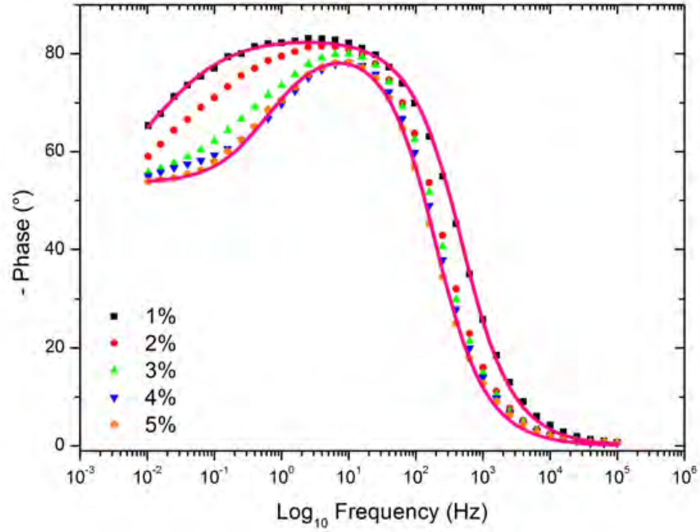

(b)

Figure 3.13: Bodeplots showing the modulus (a) and the phase (b) of the 5 different diamond samples. All of them were fitted with the model from Figure 3.12 but only 2 are shown. Representation shows half of the datapoints for clarity.

The impedance response of a CPE is:

$$Z = \frac{1}{(Q(j\omega)^n)} \tag{3.1}$$

In which Q has units of S· s^n/cm^2. In the case of an ideal capacitive interface, the exponent n = 1 and the CPE element is purely capacitive. If the associated exponent (n) approaches zero, the impedance reduces to an ideal resistor and if n = 0.5 than a Warburg impedance is obtained, in which diffusion limited effects take place. It is known that the impedance behavior reflects the electrical and electrochemical properties of the electrode materials and electrolyte solution, as well as the microscopic morphology of the interface. Since the electrolyte solution, counter electrode and measurement conditions were kept the same, the only significant differences were the morphological properties of the various samples (1-5%), as was already shown by SEM in Figure **??** and Raman in Figure 3.10.

In Figure 3.13 the Bodeplots of the 5 different diamond samples are shown. In total 15 datapoints per decade were measured but less are shown for clarity, the fitting is represented by the full line. Panel (a) shows the modulus and (b) represents the corresponding phase. Within these 5 samples there are specific frequency dependent characteristics that clearly stress out the differences between each sample. Fitting the impedimetric data with the classical Randles model from 3.12 (a) resulted in poor fits with χ^2 of 10^{-2} and worse. According to literature at least a χ^2 in the order 10^{-3} or lower is acceptable for a given model with a proper physical approximation. When measuring at lower frequencies, adsorption and diffusion phenomena come into play and the addition of a Warburg component (W) is necessary to account for these effects. After addition of the Warburg component in series with the R_{POL}, significantly better fits were obtained for all the samples, for all frequencies (χ^2 below 5×10^{-4}). The updated model R(Q(RW)) is shown in Figure 3.12 (b). By decomposing the spectra and fitted results, a better insight into the electrochemico-morphological differences was obtained.

The R_s can be extracted either mathematically or graphically from the high frequency domain. Both the calculated and graphical results show a direct proportional relation between R_s and the [C/H]-ratio. This also corresponds with the resistivities from Table 3.1. It is clear that R_s not only comprises the electrolyte solution but also includes the resistance of the electrode itself (Eq 3.2).

$$R_s = R_{electrolyte} + R_{electrode} \tag{3.2}$$

In this case there is a large contribution of the electrode resistance to the total R_s because the diamond was grown on an insulating quartz substrate and therefore relies on in plane conductivity, instead of perpendicular conductivity in the case of conductive substrates. Figure 3.14 (a) represents the relation between the calculated R_s and the [C/H]-ratio.

In the middle frequency domain the phase shifts to lower frequencies with increasing [C/H]-ratio. Interestingly the Q_{dl} was also directly proportional to the [C/H]-ratio as can be seen in Figure 3.14 (b). By increasing the [C/H]-ratio the double layer capacitance increases from 1.54e^{-6} F for the 1% to 2.46e^{-6} F for the 5% sample. From literature it is known that non-diamond sp^2 carbon results in a larger interface capacitance [88]. From the Raman

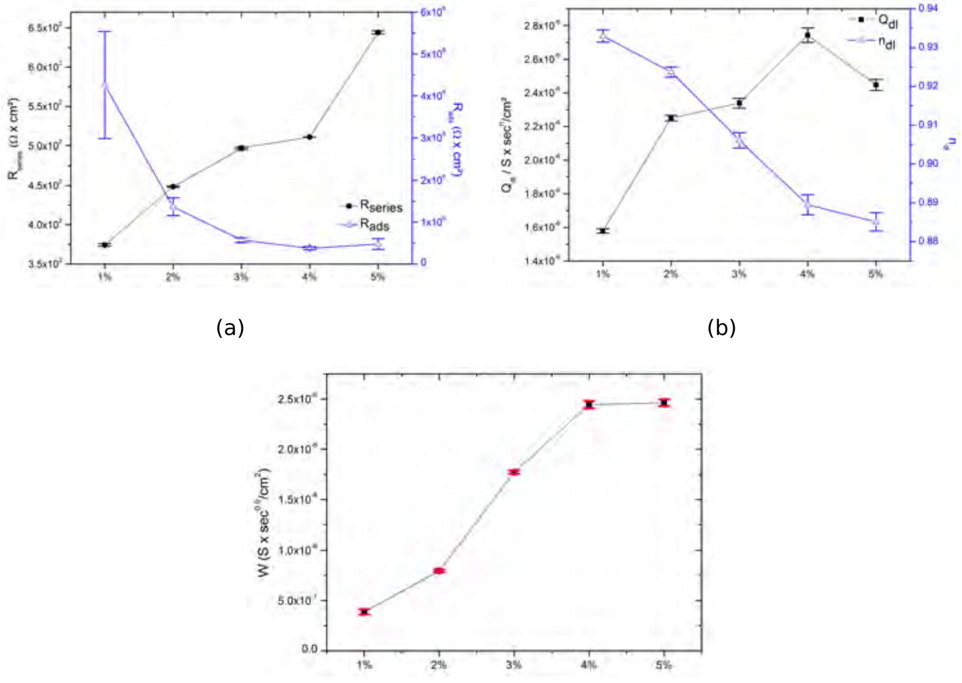

(a)

(b)

(c)

Figure 3.14: Summary of the calculated values of the impedance spectra with R(Q(RW)) model. The parameter of interest is plotted against the corresponding sample.

measurements in Figure 3.10 an increase in sp^2 carbon content was observed with increasing [C/H]-ratio. Another clear difference was observed in the low frequency regime. Especially the phase plot (Figure 3.13 (b)) indicates large differences. These changes are represented by a R_{ADS} and Warburg component. The Warburg is a diffusion-related impedance element (in the infinite-length approximation) with an impedance of:

$$Z_W = \frac{1}{Q_W(j\omega)^{0.5}} \tag{3.3}$$

It is of utmost importance that for low frequency measurements the Warburg component is present to fit the data that suggests a slow adsorption/desorption process dominates at low frequencies [48].

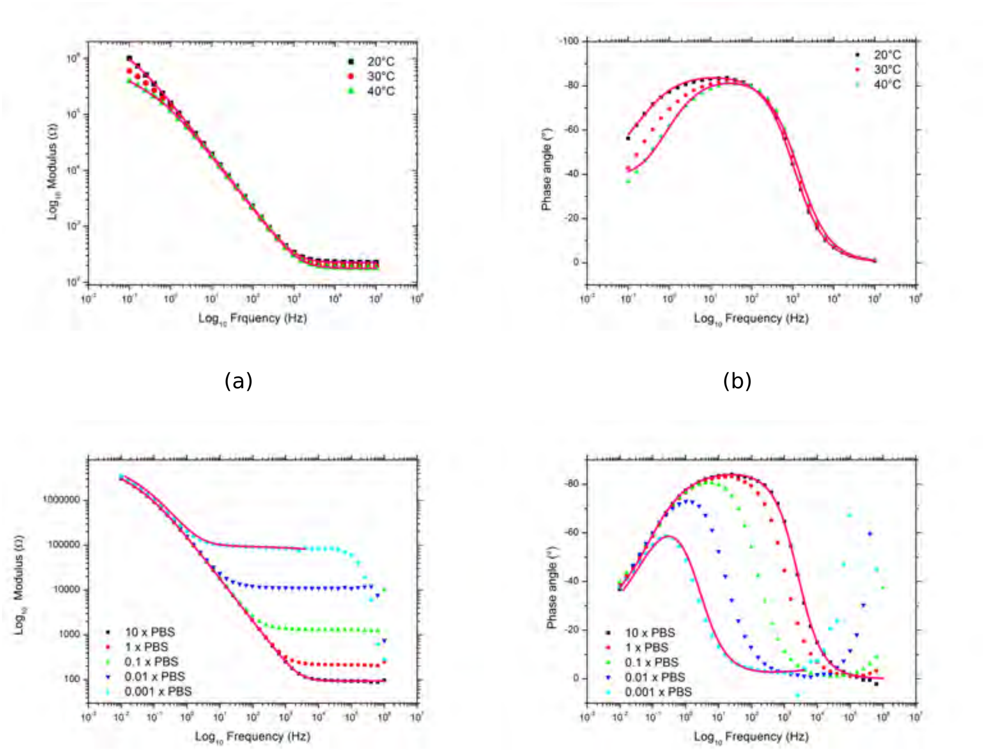

(a) (b)

(c) (d)

Figure 3.15: Bode plots of the 1 % diamond sample as illustration. In (a) the modulus of temperature variation (20-30-40°C) is shown. Panel (b) represents the corresponding phase. Panel (c) and (d) show the modulus and phase plots of varying the ionic concentrations ranging from 0.001 × PBS to 10 × PBS respectively.

The gradual change of the Warburg is also positively correlated to [C/H]-ratio which indicates, that depending on the morphology of the diamond there are different physicochemical events occuring at the interface (Figure 3.14 (c)). This finding is also supported by the inverse relation of the R_{ADS} (Figure 3.14 (a)).
To further identify these changes, 2 measurement parameters were varied:

- Temperature was varied from 20-30-40°C shown in Figure 3.15 (a) and (b)
- Ionic concentration were varied between 0.001 and 10 × PBS shown in Figure 3.15 (c) and (d).

Note, only the graphs of the 1% sample are shown as illustration but the fit results for the 1 and 5% are represented in Table 3.3.
When temperature increases, the impedance spectrum showed significant changes in the high and low frequencies. Remember, the high frequencies were dominated by resistive changes, moreover the R_s. As mentioned before this R_s comprises electrode and electrolyte resistances. According to $Kohlrausch - Onsager$ the resistance of an electrolyte decreases when temperature increases. In addition, the grain boundaries also exert a temperature sensitive conductivity in which the resistance decreases as temperature increases [87]. Both effects contribute to the overall decrease in R_s.

Table 3.2: Fit results obtained from modeling the various temperatures with the R(Q(RW)) model. Only the 1 and 5% samples are shown with the difference between the two extremes.

	1%		5%	
Element	20°C	40°C	20°C	40°C
R_{series}	224	177	680	645
Q_{dl}	1.03e-6	1.16e-6	1.93e-6	2.03e-6
n_{dl}	0.95	0.94	0.93	0.93
R_{ads}	9.86e5	2.15e5	9.86e5	1.63e5
W	1.21e-7	4.06e-7	5.22e-7	5.22e-6

The interface capacitance (Q_{dl}) shows a slight increase of ± 0.1μF in both cases. More important are the R_{ads} and W. Both show a temperature sensitivity. R_{ads} has more effect on the 5% compared to the 1%. Also the Warburg quadruples in the 1% sample whilst for the 5% it increases a tenfold. These results provide an early indication that the 5% diamond sample is more susceptible for diffusion/adsorption effects.

Table 3.3: Fit results obtained from modeling the various ionic concentrations with the R(Q(RW)) model. Only the 1 and 5% samples are shown with the difference between the two extremes

	1%		5%	
Element	0.001 × PBS	10 × PBS	0.001 × PBS	10 × PBS
R_s	192	9.06e4	377	5.22e4
Q_{dl}	1.16e-6	1.28e-6	2.29e-6	2.91e-6
n_{dl}	0.94	0.93	0.88	0.87
R_{ads}	3.02e6	1.32e6	3.66e6	5.36e5
W	1.55e-6	1.94e-6	1.79e-6	7.33e-5

The change in ionic concentration has mainly an enormous influence on the R_s due to major ionic conductivity changes. Such low conductivities results in large R_s values causing a strong upward shift in the modulus, Figure 3.15 (c) and a left shift in the phase angle (Figure 3.15 (d)). Note, when bio-measurements are conducted, such high resistivities ((R_s) from electrode or solution) should be avoided at all cost, because they mask certain parameters in a confined frequency range due to their large spectrum shift!

The Q_{dl} decreases with increasing concentration due to compression of the diffuse layer near the electrode surface. The R_{ads}, which is of important interest, drops for the 1% from 3.02e6 Ωcm^2 to 1.32e6 Ωcm^2 whilst for the 5% from 1.79e-6 Ωcm^2 to 7.33e5 Ωcm^2. In addition the Warburg contribution is also concentration sensitive. It is positively correlated to the concentration due to a higher number of ions that can participate in the adsorption/diffusion processes. From the previous results we have shown that the largest variations in R_{ADS} and W were found in the 5% sample.

To further investigate this adsorption process we applied a potential scan during impedance sweeps to identify and study the capacitive origins. The potential range was between -0.8 and 0.8 V and spectra were taken from 100 kHz to 0.1 Hz.

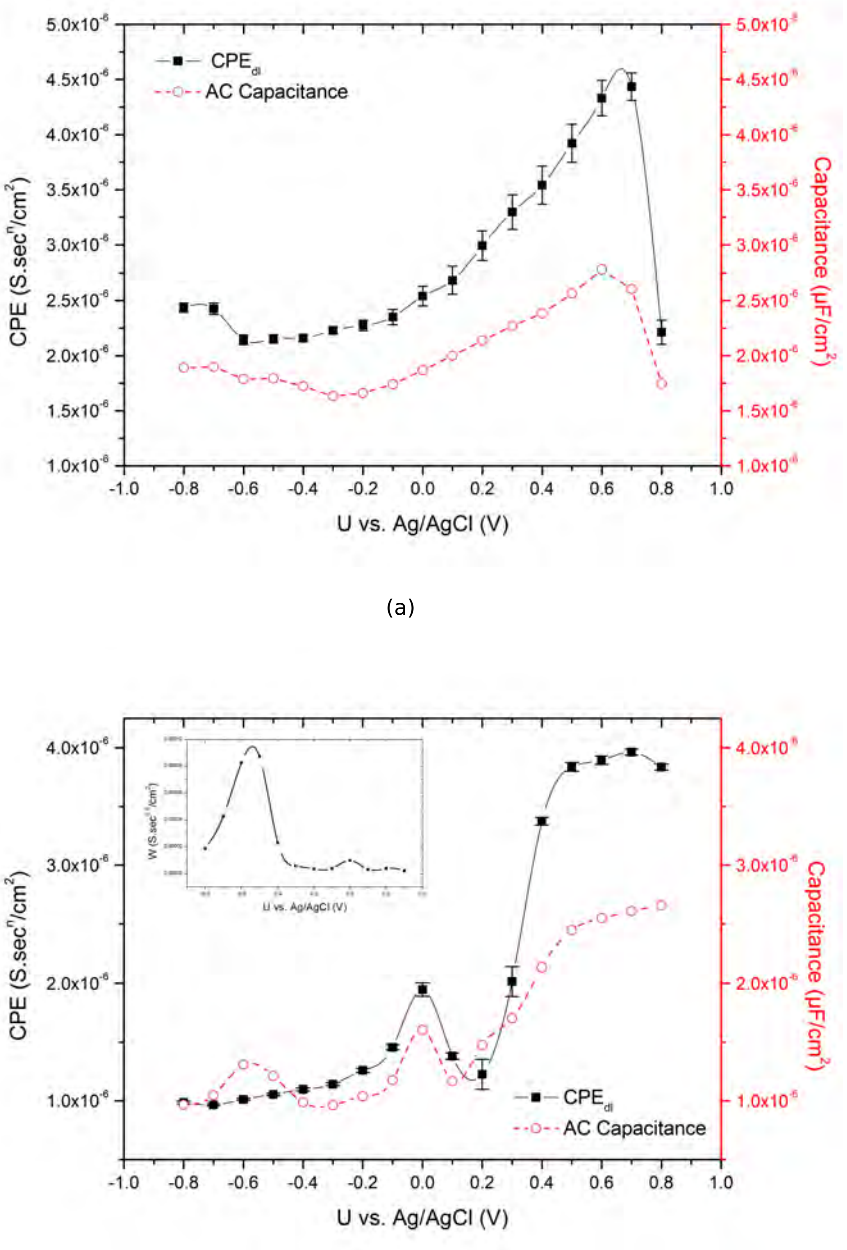

(a)

(b)

Figure 3.16: Comparison between AC capacitance (squares), measured at 10 Hz, and the values of the Q$_{dl}$ element (circles) derived from fitting the impedance spectra at different potentials of the 1% sample.Comparison between AC capacitance (squares), measured at 10 Hz, and the values of the CPE$_{dl}$ element (circle) derived from fitting of the impedance spectra at different potentials of the 5% sample.

In the 5% potentialscan (Figure 3.16 (b)) there are 2 clear peaks at 0V and -0.6V in the AC capacitance from the system (circles). By comparing this to the Q_{dl}, obtained from fitting the spectra at all the potentials, only the peak at 0V remains and the peak at -0.6 V is shifted towards the Warburg contribution as can be seen in the inset of Figure 3.16 (b). Above +0.2V a similar trend is observed between the AC capacitance and the Q_{dl}. More interesting was the 1% diamond sample where no significant peaks were observed in the spectrum (Figure 3.16 (a)). The rest of the 1% spectrum showed a similar behavior between the AC capacitance and the Q_{dl} as the 5%.

By measuring the capacitance of the 1 and 5 % samples between 1 and 100 Hz, frequency dependent differences were observed. The observed frequency dispersion in the 1% sample is lower than the 5% (Figures 3.17 (b) and 3.17 (a)) respectively (both scaled on the same axis)). The potential scans show at various potentials the adsorption behavior between the two samples. The dispersion indicates that ion adsorption at the interface is more pronounced at 0V for the 5%.

All of the results above provide the evidence that ion adsorption at the interface is more pronounced at the 5% compared to the 1% diamond sample. The correlation between the Warburg and R_{ads} to the [C/H]-ratio, the

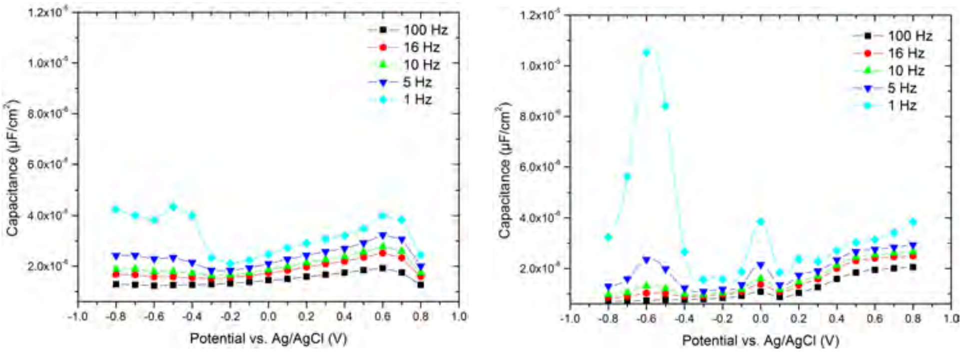

(a) (b)

Figure 3.17: Frequency dispersion of the measured capacitance of the 1% O-terminated B:NCD electrode (a) and for the 5% in panel (b). The experiments have been carried out at 100, 16, 10, 5 an 1 Hz. Frequency dispersion is observed in the potential range of the capacitance peak.

potential sweeps and frequency dispersions all indicate that the surface morphology plays an important role in the selection of diamond as working electrodes for electrochemical applications. However, up till now we only studied the non-faradaic processes. The next paragraph will discuss the electrochemical dependent behavior on diamond morphology with a potassiumferricyanide redox couple in the electrolyte.

Faradaic processes

When a redox agent, such as potassiumferricyanide ($K_3Fe(CN)_6^{3-/4-}$) is added to the solution, reduction and oxidation occurs at the electrode interface. In our case we used 10 mM $K_3Fe(CN)_6$ in 1×PBS at a pH of 7.4 at 30°C. Previously the impedance spectra only had a relative small Warburg contribution, but with the addition of this redox mediator diffusion and charge transfer dominate the spectrum. The R_{ADS} is in this case changed to a charge transfer resistance R_{CT}, and as the name implies, faradaic currents take place due to redox reactions. The electron rate constant (κ^0), a measure for efficiency, was calculated from the charge transfer resistance using Eq. 3.4 and Eq. 3.5:

$$R_{et} = \frac{RT}{nFI_0} \tag{3.4}$$

with R the ideal gas constant, T the temperature, F as Faraday's constant and I_0 as the exchange current under equilibrium.

$$I_0 = nFA\kappa^0[S] \tag{3.5}$$

Here A is the electrode area, [S] the concentration of the redox species and n the number of electrons transferred per molecule of the redox probe. No correction was made for double-layer or iR effects; therefore these are only apparent rate constants.

The impedance spectra from which the R_{CT} were extracted are shown in Figure 3.18 (a). They were fitted with the R(Q(RW)) model from Figure 3.12(b). The calculated rate constants κ^0 are shown in Figure 3.18 (b). Reports from literature on the κ^0 for diamond electrodes vary from 10^{-6} to 10^{-2} cm/s for the ferri-ferrocyanide system [89, 90]. In our case, for the lowest [C/H]-ratio B:NCD we find $\kappa^0 = 3.01 \times 10^{-3}$ cm s^{-1}. Whilst for the 5% we find $\kappa^0 = 3.51 \times 10^{-6}$ cm s^{-1}. Also the k^0 is related to the [C/H]-ratio which indicates that a high quality morphology of the diamond film is very crucial for obtaining fast electrode kinetics.

We have to note that the obtained Q_{dl}, from fitting the redox-EIS spectra (Figure 3.18), was in good agreement with the results obtained from the $non-faradaic$ section (Figure 3.14 (a)). Also the same trend was observed but in a more refined interpretation we must remember that a constant phase element is a distributed element. Physically, it can be understood as the consequence of a distribution of the activation energies on the whole electrode surface, which is correlated to the existence of a wide variety of active sites, differentially activated within the potential [88].
To further focus on the electrochemical behavior of the diamond electrodes, cyclic voltammograms were recorded at various scan rates (v) of 10, 20, 50, 100, 200 mV/s. In Figure 3.19 the background current at 0.1 V/s of the 1% (full line) and 5% (dashed line) sample in 1 × PBS solution is recorded. No faradaic transfers take place indicating no side reactions or impurities were present. The low background current density is in the transition range of nA-μA/cm^2, typically for diamond electrodes. Only at slight overpotentials above +0.6V an increase in anodic current is observed in the 5% (dashed) voltammogram. This slight increase could be related to a mild oxidation of non-diamond carbon impurities at the surface. The peak did not increase with repeated cycling [91].
By adding the potassiumferricyanide agent, the following reaction takes

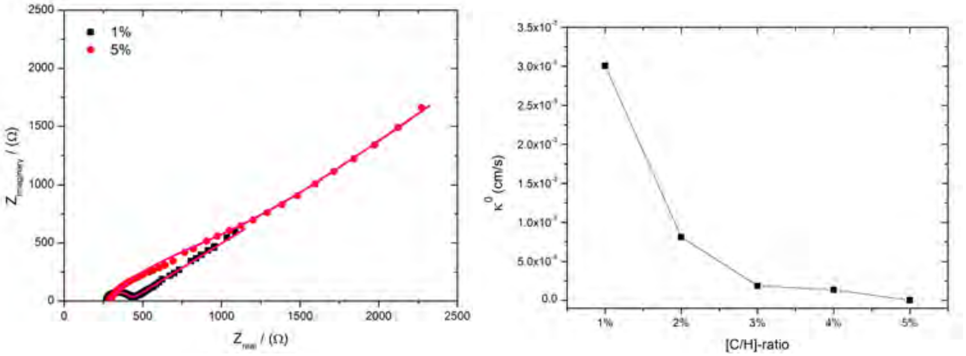

(a) (b)

Figure 3.18: Comparison of impedance spectra in the Nyquist plane in 10 mM solution ferri/ferrocyanide in 1× PBS for the 1% and 5% sample, κ^0 in function of [C/H]-ratio in 10 mM $K_3Fe(CN)_6$

place during potential cycling:

$$[Fe_{III+}(CN)_6]^{3-} + e- \leftrightarrows [Fe_{III+}(CN)_6]^{4-} \tag{3.6}$$

$K_3Fe(CN)_6$ behaves anomalously on carbon and metal electrodes and does not involve simple electron transfer, in which the electrode acts as a source and sink for electrons. There are several factors known to influence the electrode kinetics. The surface cleanliness, the doping type and level, the presence of sp^2 carbon and other carbon impurities [92]. The electrode kinetics are also influenced by the surface termination with the smallest ΔE_p observed at clean hydrogen terminated diamond. After oxidation, the ΔE_p increases drastically [91]. As discussed earlier (Section 3.1.3) the reaction rate is also very sensitive to electrolyte composition, the choice for 1 × PBS as supporting electrolyte is not the most ideal for voltammetric studies, but it is the most important biological buffer in which diamond electrodes find a large field of application.

In voltammetry 2 different currents exist, the first is the background current due to charging of the double layer capacitance at the interface and the second is the faradaic current that emerges from electron transfer of the redox species.

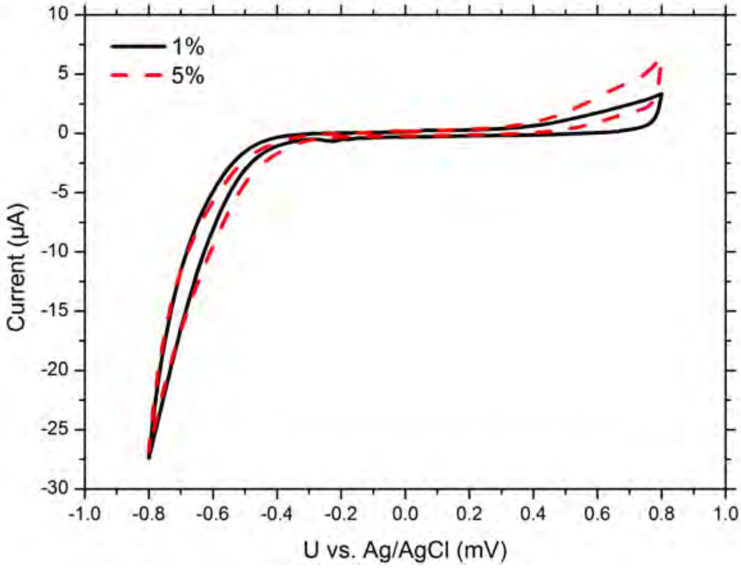

Figure 3.19: Cyclic voltammetric i-E recording of the 1% and 5% sample in 1 × PBS at pH 7.4 at 30°C

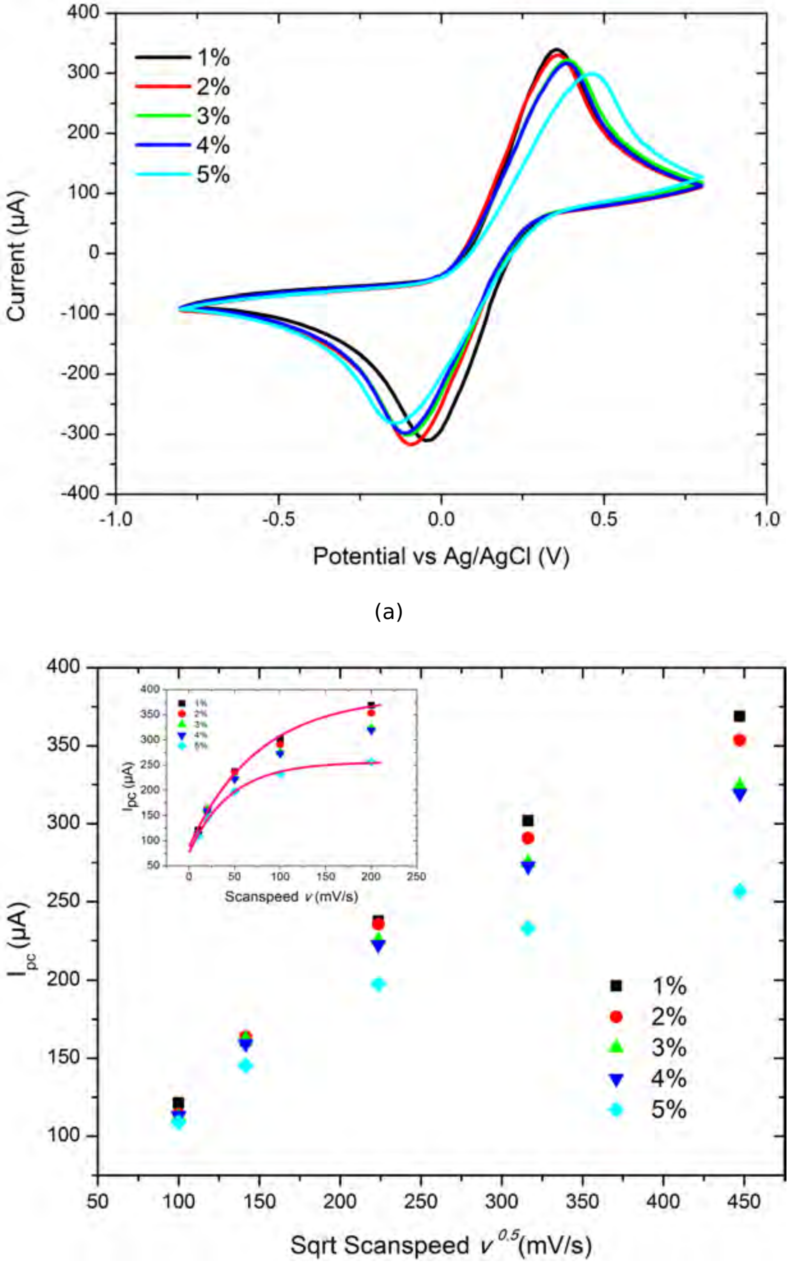

(a)

(b)

Figure 3.20: In panel (a) Cyclic voltammetric i-E curves of the 5 different [C/H]-ratio's are shown. They were recorded at a scanspeed of 50 mV/s. Panel (b) shows the relation between the cathodic current versus the square root of the scanrate. The inset provides a way to determine a measure for the reversibility

The various diamond samples were analyzed by the quasi-reversibility criteria which states that: I_p increases with the square root of the scanrate ($v^{1/2}$) but do not keep the proportionality, the peak separation (ΔE_p) is larger than 60/n mV and increases with the scanspeed (v), the cathodic peak potential shifts to negative values with increasing v. In our diamond samples the voltammograms indicate a decrease in reversibility with increasing [C/H]-ratio. Also the cathodic peak potential, E_{pc} shifts to more negative values with the increase of the v. The voltammograms obtained at 0.1 V/s are shown in Figure 3.20 (a). Ranging from 1 to 5% an increase in peak shift (ΔE_p) was observed. The obtained values are depicted in Table 3.4. The relation of I_{pa}/I_{pc} is for reversible systems 1, but in our case these values decrease depending on the [C/H]-ratio. The reversibility of an electrochemical process results in a linear relation in the current versus the square root of the scanrate ($v^{1/2}$). This was only observed in the 1% diamond sample. To have a measure for the loss in reversibility and to correlate this to the [C/H]-ratio, an unusual method was employed. The current was plotted versus the scanrate v (not $v^{1/2}$) and using a single order exponential fit, time constants were obtained. These τ's were correlated to the morphology i.e. the grain size. By using pearson correlation statistics. A correlation parameter of 95.7% with a p-value of < 0.035 indicated a strong relation between the 5 different samples and the obtained results.

Table 3.4: Summary of the cyclic voltammetry parameters at a scanrate of 50 mV/s

Sample (%)	ΔE_p V	I_{ac}/I_{pc} n.a.
1	0.318	0.968
2	0.361	0.959
3	0.392	0.951
4	0.394	0.954
5	0.483	0.901

3.2.3 Conclusion

In the previous section we studied the electrochemical properties of 5 diamond samples grown with linearly varied [C/H]-ratios (1-5%). According to SEM and XRD the size of the diamond crystallites decreases with increasing methane concentration. Raman revealed an increase in the non diamond sp^2 carbon content with increasing methane concentration. The electrochemical properties were studied using cyclic voltammetry and electrochemical impedance spectroscopy. Modeling of non-faradaic EIS measurements indicated a positive correlation between the [C/H]-ratio and the electrode resistance (R_s), double layer capacitance (Q_{dl}) and Warburg component. Only the adsorption resistance (R_{ADS}) had a negative correlation. By combining potential scans and impedance sweeps, frequency dispersions indicated that the 5 % diamond (largest sp^2 content) was more prone to ion adsorption. In addition there was a good correlation in the Q_{dl} between the faradaic and non-faradaic results. Cyclic voltammetry also indicated that an increase in the sp^2 content is detrimental for good electrode kinetics. Finally, we determined a measure for the reversibility of a CV scan and correlated this to the diamond crystal size in which a significant correlation was found. These results provide the background knowledge for selecting the proper diamond electrode for electrochemical applications. To summarize, the higher the electrode quality, the higher the electrochemical performances are.

3.3 Electrochemical properties of variations in boron doping

In this section we will briefly discuss the influence of boron doping on the electrochemical properties.

3.3.1 Materials

For this study diamond samples were grown with the same [C/H]-ratio but with a varying [B/C]-ratio between 1000 and 9000 ppm. The samples were prepared and measured in the same way as described in the section above. When boron doping increases, the transparency decreases and the diamond becomes more blueish. A photograph of the diamond samples is shown in Figure 3.21

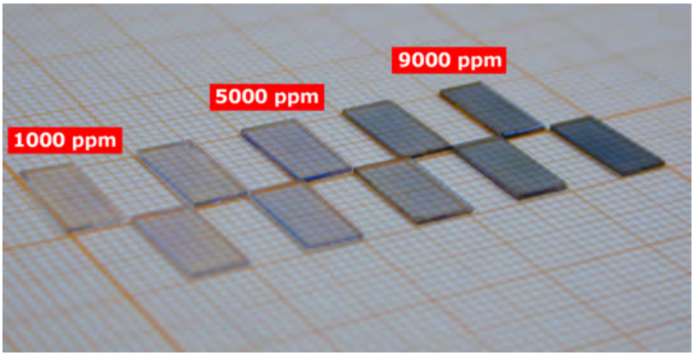

Figure 3.21: A series of variously boron doped diamond between 1000 and 9000 ppm grown by S.D. Janssen

3.3.2 Results

In Figure 3.22 the non-faradaic characteristics of the diamond samples are shown. Modeling was done with the extensively discussed R(Q(RW) model. However, this model is only applicable for high doped diamond that exerts metallic-like conductivity. For the lower doping concentrations (< 3000 ppm) a shoulder appears in the middle frequencies giving rise to an additional (QR) component. This additional (QR) component is assumed to account for the band bending in the diamond film due to the semi-conductive nature of the diamond film. In the previous section we stated that the R_s value should not be to large to avoid loss of information. Here, in these spectra, can be clearly seen that resistivity of the diamond film dominates throughout the entire spectrum causing the phase maximum to shift to lower frequencies. Interestingly, even with large variations in boron doping, all of the diamond spectra show a similar low frequency behavior (except for the 2000 ppm). These findings support the assumptions made in the previous section.

Also the electrons transfer properties are greatly influenced by variations in boron doping. The voltammograms in Figure 3.23 show the effects of various boron doping concentrations. When boron doping increases, the electrode performance also increases. Due to the high resistivity of the material and the lack conduction properties in the diamond the i_{pa},i_{pc}

drops significantly depending on the boron dopant concentration. The $\triangle E_p$ also increases and when reaching 3000 ppm it was difficult to even measure a voltammetric response, the 2000 ppm only showed a linear behavior and is therefore not shown.

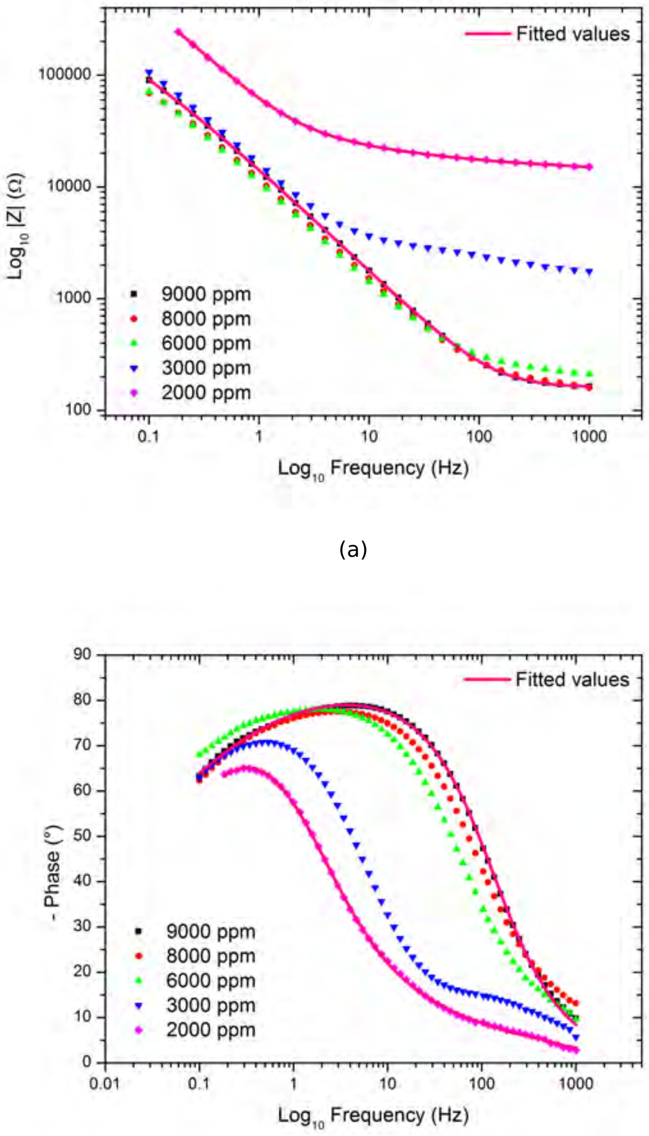

(a)

(b)

Figure 3.22: Panel (a) shows the modulus of the different doping concentrations, (b) represents the phase. Only 2 curves are fitted, the highest dopant concentrations was fitted with the traditional R(Q(RW) and the lowest dopant with R(QR)(Q(RW). Less datapoints are shown for clarity.

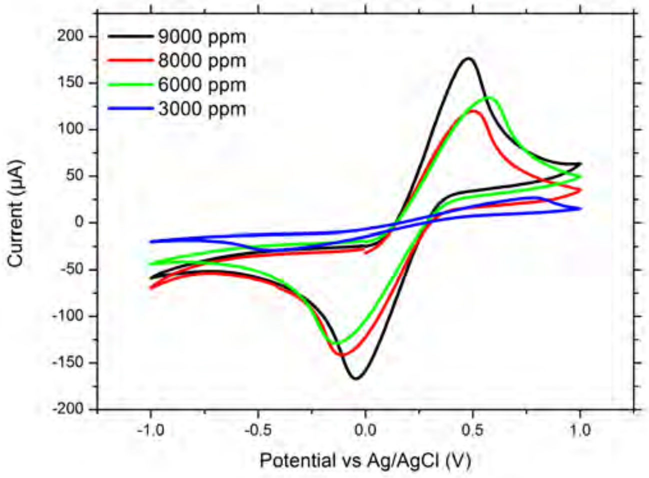

Figure 3.23: Cyclic voltammetric i-E curves from -1 to 1 V of diamond samples doped with various concentrations of boron measured in 1× PBS with 10 mM $K_3Fe(CN)_6$. Scanspeed was 100 mV/s.

3.3.3 Conclusion

The boron concentration, which is a key parameter in diamond electrode choice was briefly discussed. We conclude that the increasing boron concentration decreases the resistivity of the electrodes. In the low frequency part all of the spectra joined together. At the metal/semi-conductor transition range (around 3000 ppm) an extra consideration was made to the equivalent circuit by adding an additional (QR) component in series with the model described in the previous section. Also the electrode quality increases with increasing boron concentration. Not only is this information important for choice of diamond electrodes for various biosensing applications, it is also crucial for devising small, whole diamond coplanar electrodes which will be discussed in Chapter 6.5.

Chapter 4

The diamond interface

In this chapter we will only focus on the diamond interface, since it responsible for housing and maintaining the biological functionality of the receptors used for immunosensing. First, we will discuss the diamond interface followed by two possible surface functionalities and their properties. Next the capability and organization of the receptor layer is studied by various characterization techniques. The behavior of the receptor proteins is studied by real-time, in-situ impedance measurements. As concluding section, different surface functionalizations are proposed for possible use in biosensor constructs.

4.1 Morphology of the diamond interface

In this section the morphological characterization of diamond substrates used for immunosensing is discussed. Since the growth parameters, as the operator were the same throughout the thesis work, very homogeneous, high-quality and comparable substrates were obtained.

The main characterization tools used for the interface study were SEM, AFM, XPS and Raman. SEM showes a continuous, closed film without pinholes with individual crystal sizes ranging up to 100 nm, interconnected by grain boundaries. Average film thicknesses of 200-300 nm were used resulting in purple/greenish mirror-like samples (Figure 4.1 (a)). The overall area roughness (R_a^{rms}) was measured by AFM and typically the NCD substrates had an average roughness of 14±2 nm (Figure 4.1 (b)). It is clear

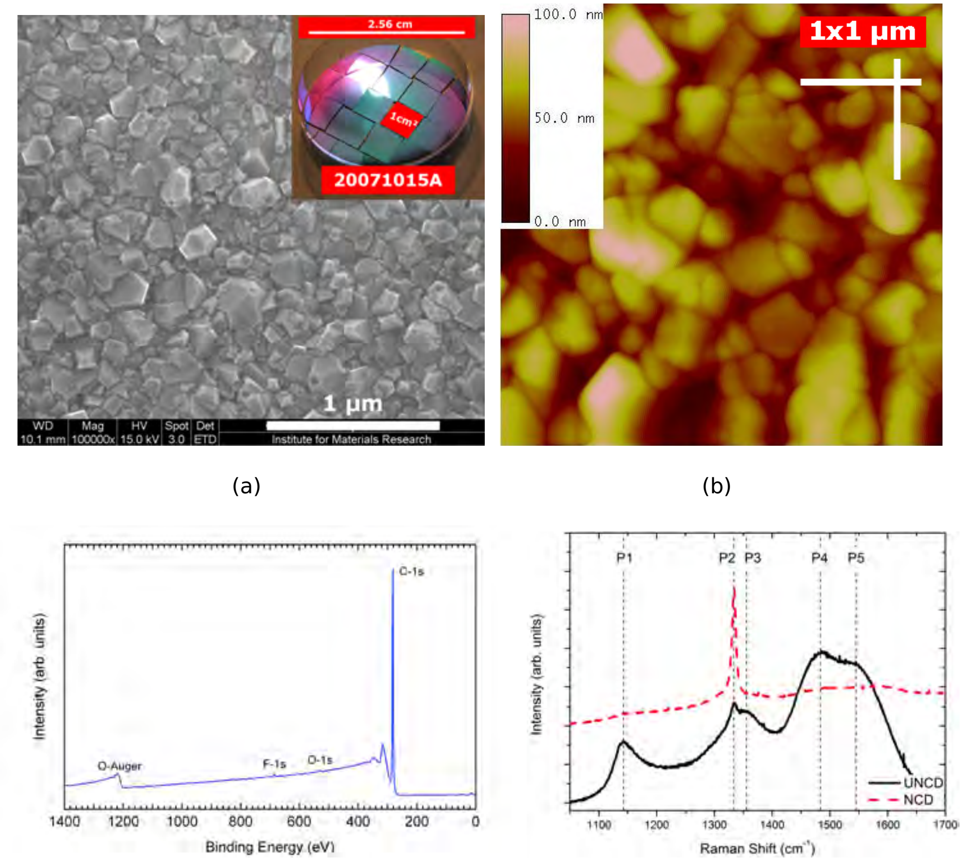

(a) (b)

(c) (d)

Figure 4.1: In (a) a SEM recording of a NCD diamond surface, the inset shows a photograph of a 2" diamond film diced in 1cm^2 samples. In panel (b) an AFM recording of a NCD surface (R_a^{rms}= 14±2 nm). In (c) an XPS spectrum of a fresh grown hydrogenated NCD surface and in (d) a Raman spectrum of the NCD and an UNCD sample.

that larger diamond grains result in a larger surface roughness. This in turn favors the immunosensor because it not only increases the total surface area but also creates possible adherence sites for receptor proteins to settle. In Figure 4.1 (c) a smooth XPS spectrum of a freshly grown diamond film shows a clear C-1s peak originating from the diamond, a small O-1s peak is present due to the adsorption of a thin atmospheric water film, and (sometimes) a small fluorine peak was observed originating from the vacuum system. The carbon content and composition (sp^2/sp^3) was identified by Raman spectroscopy shown in Figure 4.1 (d). As illustration a comparison is shown between an NCD and UNCD surface. A typical diamond (sp^3) peak is observed at 1332 cm^{-1} for the NCD sample (red). The UNCD also has a peak at this position but the ratio with respect to the other observed peaks is largely reduced (black). The peaks that arise at 1350 (P3) and 1550 cm^{-1} (P5) correspond to micro- and/or nanocrystalline carbon phases, predominantly sp^2 in character. The broad band in the 1490-1510cm^{-1} (P4) range is commonly attributed to amorphous carbon. The peak at 1140 cm^{-1} is possibly related to the acethylene C-H chains but this topic is still under discussion in literature [93, 94, 95, 31].

4.2 Oxidized and hydrogenated diamond

In this section the NCD surface terminations were further studied. Herefore the NCD films were subjected to consecutive oxidation and hydrogenation steps in order to obtain the best surface conditions for protein studies. Herefore, the following characterization tools were used: the surface free energy, contact angle and XPS measurements.

4.2.1 Experimental

Surface free energies of the diamond interface were determined by the OWRK method described in section 2.3.1. In this experiment pure test liquids were used to obtain insight in the polar and disperse properties on oxidized and hydrogenated diamond. The following probe liquids were used, listed according rising polarity: Diiodomethane (Diiodo), Benzyl Alcohol (Ba), Ethylene Glycol (Eg), Formamide (Forma), Glycerol (Gly) and Water (MilliQ). The individual polar and disperse contributions of the test liquids to the total SFE are listed in Table 4.2.

The following treatments were sequentially applied to six NCD samples to obtain either a hydrogenated (NCD:H) or oxidized (NCD:O) surface:

After each step the surface free energies were measured with the six probe liquids. This has been repeated for 3 times. The contact angles were measured by the sessile drop technique with 1 liquid per sample to avoid any memory effects of the previous liquid. Also, all the treatments were done with the same samples to avoid discrepancies as much as possible.

4.2.2 Results

In Figure 4.2 an example is given of the contact angles of 6 different probe liquids on NCD:H.

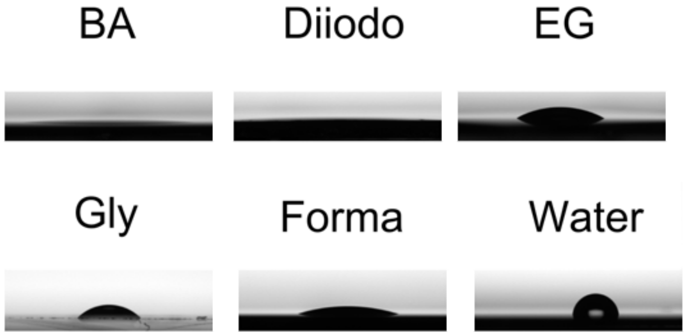

Figure 4.2: Contourplots of the different probe liquids on a hydrogen terminated NCD surface.

Taking the values of the probe liquids into account, together with the obtained contact angles, the surface free energy could be calculated according to the method described in section 2.3.1. The obtained SFE's are shown in Figure 4.3 (a). The results were averaged over 3 independent measurements and errors less than ±2% were obtained. The bar height represents the total SFE, the filled and shaded part are the contributions of the polar and disperse component respectively. The absolute values are shown in Table 4.3. As can be seen from the figure the total SFE for

Table 4.1: Surface tensions, γ_l, of the used test liquid, as well as the single contribution to the surface tensions: dispersive (γ_l^D) and polar (γ_l^P) in units of mJ/m^2.

		Diiodo	Ba	Eg	Forma	Gly	Water
γ_l^D	mJ/m^2	48.5	39	29	39	34	21.8
γ_l^P	mJ/m^2	2.3	8.7	19	19	30	51
γ_l^{D+P}	mJ/m^2	50.8	39	48	58	64	72.8

Table 4.2: Treatment steps for NCD substrates to obtain either hydrogenated or oxidized diamond surfaces.

Treatment	Procedure	Properties
Hydrogenation	H-plasma, 15 min,	Hydrophobic
NCD:H	50 Torr, 800°C, 4000W	
uv-oxidation	2 hr uv-ozone	Very Hydrophilic
NCD:O (uv)		
acid-oxidation	25 ml H_2SO_4 + 12.5 g	Hydrophilic
NCD:O (acid)	KNO_3, 180°C, 2 hr	

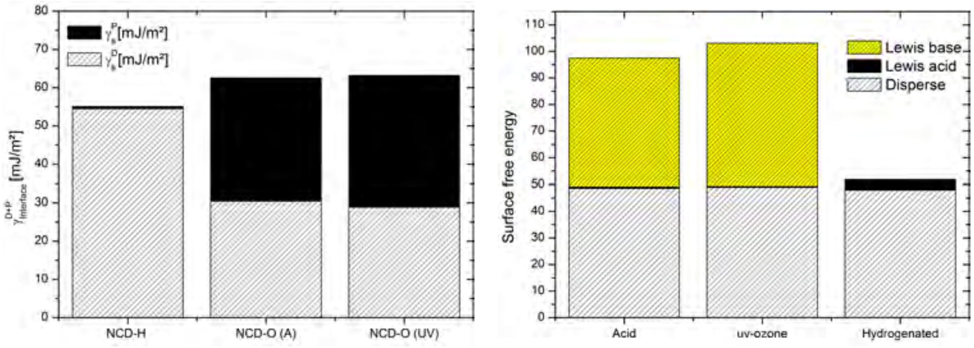

(a)

(b)

Figure 4.3: In (a) SEM image of NCD, (b) SEM image of UNCD, (c) AFM image of NCD and (d) AFM image of UNCD.

NCD:H is 55.20 mJ/m^2 with the largest contribution from a large dispersive component and virtually no polar contribution, making the diamond very hydrophobic. The hydrophobicity orignates from the hetero-polar C$^{\delta-}$ - H$^{\delta+}$ groups causing the surface dipole to reduce, and therefore in turn weakening the interaction between the polar water molecules and the film surface. This allows the cohesive forces of the water to contract, forming a well defined spherical shape.

The oxidized substrates exerted a completely different behavior. For the uv-ozone treated diamond a SFE of 63.16 mJ/m^2 was obtained and for the acid treated sample 62.56 mJ/m^2. In general, a slight increase of the total

SFE was observed whilst the polar contribution grew significantly. This polar contribution originates from the oxygen groups at the surface induced by the oxidation. These polar groups attract the electric dipoles of water molecules, which in turn minimizes the interfacial energy between the surface and the water, resulting in a wetting behavior [96]. The difference in total SFE between the oxidation steps was within the error margin. However, the focus lies on the water contact angle because all biological applications are aqueous based. The hydrophobic NCD:H had a water contact angle of 83° and dropped to 14.2° for the acid oxidized sample and non measurable for the uv-ozone oxidation. So with respect to the similar SFE, the hydrophilicity of the surface does show a significant difference. By calculating the acid/base approach of van Oss (Figure 4.3 (b)) it shows that the hydrogenated surface is mainly dominated by electron pair acceptors (Lewis acids) whilst oxidized diamond is dominated by Lewis base interactions (electron pair donors). The uv-oxidized surface results in a larger Lewis base component indicating in a more electronegative surface. In other words a better oxidized surface. Also XPS spectra were taken after each treatment step and survey scans and high resolution recordings of the C-1s peak are shown in Figure 4.4 (a) and (b). There is a clear difference between the hydrogenated and oxidized diamond surfaces. The hydrogenated only shows a carbon (C-1s) peak whilst the oxidized surfaces have an additional oxygen peak (O-1s). High resolution recordings of the C-1s show a shift to higher binding energies upon oxidation, and depending on the treatment a further shift to the left was observed. This also indicates a more electronegative surface when a diamond surface is oxidized via the uv-treatment. Note, there is also an additional oxidation

Table 4.3: Surface free energy values for the hydrogenated and oxidized NCD samples.

	γ_s^P mJ/m^2	γ_s^D mJ/m^2	γ_s^{P+D} mJ/m^2
NCD:H	54.46	0.58	55.20
NCD:O (acid)	30.47	32.09	62.56
NCD:O (uv)	28.86	34.30	63.16

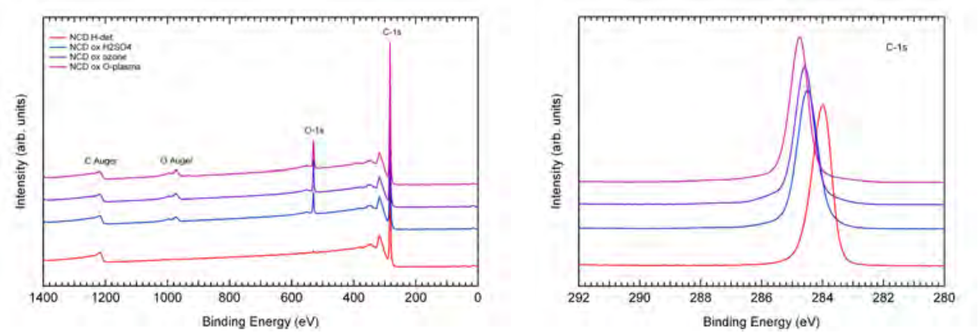

(a) (b)

Figure 4.4: XPS survey scan of the hydrogenated, uv-oxidized and acid oxidized surfaces. In panel (b) a high resolution of the C-1s peak is shown.

method shown in the XPS spectra based on exposing the diamond to an oxygen-plasma resulting in an even better oxidized surface. However, this also etches the diamond, so it is not applicable within this concept.

4.2.3 Conclusion

The surface termination facing the electrolyte has an enormous effect on the surface free energy and hydrophobic/hydrophilic properties of the diamond film. The hydrogen terminated diamond is hydrophobic whilst the oxidized were hydrophilic. The uv and acid treated samples had no clear differences in SFE, but varied largely in their water contact angle. The uv-treated samples resulted in a more electronegative surface which was indicated via the Lewis Acid/Base and XPS recordings. This indicates that uv-ozone treatment results in a more thorough oxidation. Another great advantage of this technique is the non-aggressive nature towards the diamond compared to oxygen plasma or acid oxidation which both cause etching and deterioration of the film quality. Therefore, in the future experiments we preferred the uv-ozone treatment as the most favorable oxidation treatment.

4.3 Adsorption of proteins at the diamond interface

The most reproducible and straight forward method of receptor layer immobilization, similar as in traditional ELISA experiments, is physisorption. Different substrates were tested such as diamond, silicon, quartz and silicondioxide but only the diamond surface was capable of protein adsorption. The antibodies (IgG's) adsorb on both the oxidized as hydrogenated diamond. These proteins serve as the receptor layer in future immunosensing experiments. In the end anti-CRP antibodies were used as functional receptor layer, but to obtain visual and qualitative information of IgG adsorption on diamond surfaces, we now used an anti-IgG labeled with an Alexa-488 fluorescent tracer. After adsorbing Alexa-488 fluorescent labeled antibodies (Ab-X), a qualitative visualization via confocal fluorescence microscopy was obtained. The adsorption process was done by dropcasting the diamond sample with 20 nM (30μg/ml) proteins in 1 × PBS at 37 °C for 2 hours. Afterwards the samples were rinsed for 2 times 10 sec in 1 × PBS and were also stored in PBS. In Figure 4.5 (a) fluorescence recordings of antibodies incubated on a bare hydrogenated substrate is shown. The fluorescence, originating from the proteins, result in the (artificial) green color and the black line represents a photobleaching line, which indicates that fluorescence originates from the proteins and not from background reflection. In (b) a NCD surface was first blocked with bovine serum albumin (BSA) and afterwards incubated with the same protein concentration as before. Here, no fluorescent signal was observed because BSA blocks free binding sites and therefore inhibiting antibody adsorption.

To further understand the adsorption behavior, 20 nM antibodies were exposed for different time intervals to the oxidized and hydrogenated surface. The results are shown in Figure 4.6 (a). After 10 minutes there is no longer a significant difference observed in fluorescence signal. This indicates that between 10 and 30 minutes a saturation is reached and the diamond surface is completely covered with proteins. The absolute difference between the hydrogenated and oxidized diamond at each time interval could be due to quenching effects that occur on hydrogenated diamond surfaces as described by Sakon et al [97]. Regardless of the short adsorption time required, the antibodies were always 2 hours incubated

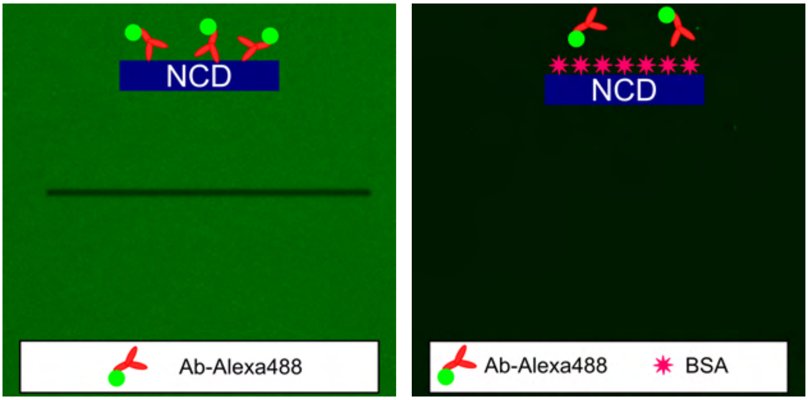

(a) (b)

Figure 4.5: Fluorescence images of Alexa labeled antibodies on (a) a bare hydrogenated diamond surface, the black line is a bleach line which differentiates the fluorescence from reflection. In (b) a BSA blocked diamond surface is shown. (256 x 256 μm, gain 850)

before usage.

When the concentration of antibodies were decreased from 200 to 2 nM, the fluorescence also decreased as shown in Figure 4.6 (b). Note, the gain was set at 750 to have a good distribution range from high to low concentrations.

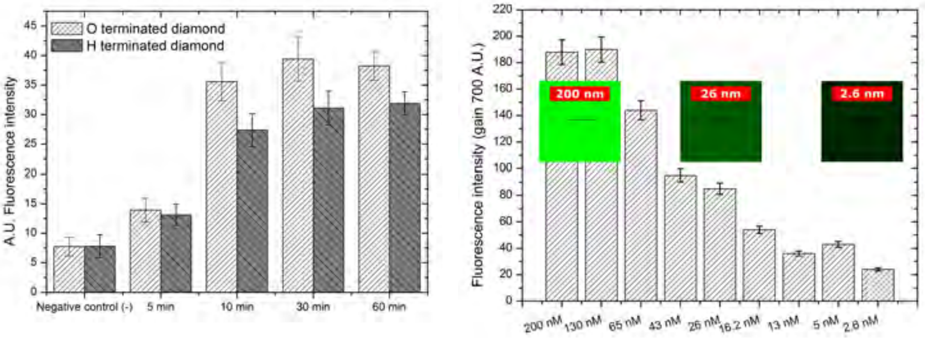

(a) (b)

Figure 4.6: In (a) different adsorption times for 20 nM of Ab-X are shown whilst (gain 700) (b) represents different concentrations of Ab-X adsorbed with the gain set to 750.

It has been shown that antibodies easily adsorb on the hydrogenated and oxidized diamond surfaces and quickly reach a saturation. We continue to use the 20 nM concentration for protein adsorption. In the following section we study the difference of immobilized protein layer on oxidized and hydrogenated diamond by X-ray photoelectron spectroscopy.

4.4 XPS study of protein layers at the diamond surface

With X-ray photoelectron spectroscopy it is possible to give an estimate of the protein coverage on oxidized and hydrogenated diamond.

4.4.1 Experimental

Four diamond substrates were used from which 2 were uv-oxidized and 2 were hydrogenated. From each treatment there was one reference and the other was coated with 20 nM antibodies. The antibodies used were goat-anti-mouse IgG's with 6 Bodipy FL fluorescent labels per antibody (Invitrogen, Belgium). This label has a molecular core containing 2 fluorine atoms (F) that could serve as a tracer for elemental analysis and quantification. After the standardized incubation, the samples were washed in 1 × PBS and dried under N_2.

4.4.2 Results

The survey and high resolution scans of the four samples are shown in Figure 4.7. In panel (a) the bare diamond reference samples are shown. On the NCD:H there was a small boron peak (B-1s) and on NCD:O silicon peaks (Si-2s and Si-2p) were present.
The spectra of the protein coated substrates are shown in Figure 4.7 (b). In both spectra additional peaks were observed such as nitrogen (N-1s), oxygen (O-1s) and sulfur (S-2s, and S-2p). Interestingly, the silicon signal is now present on both substrates and even increases after functionalization. This appears to be inherent to the system, probably due to protein purification of the supplier. The N and O elements originate from the protein amino acid content ($-NH_2$, -COOH) groups. The amino acids methionine and cystein contain sulfur groups used for disulfide bridging and in addition give rise to the S-1s peaks. Unfortunately the Fluorine-tracer concentration was out of detection limits, so we focussed further on the sulfur signal to construct a theoretical model for obtaining surface information regarding the protein coverage.

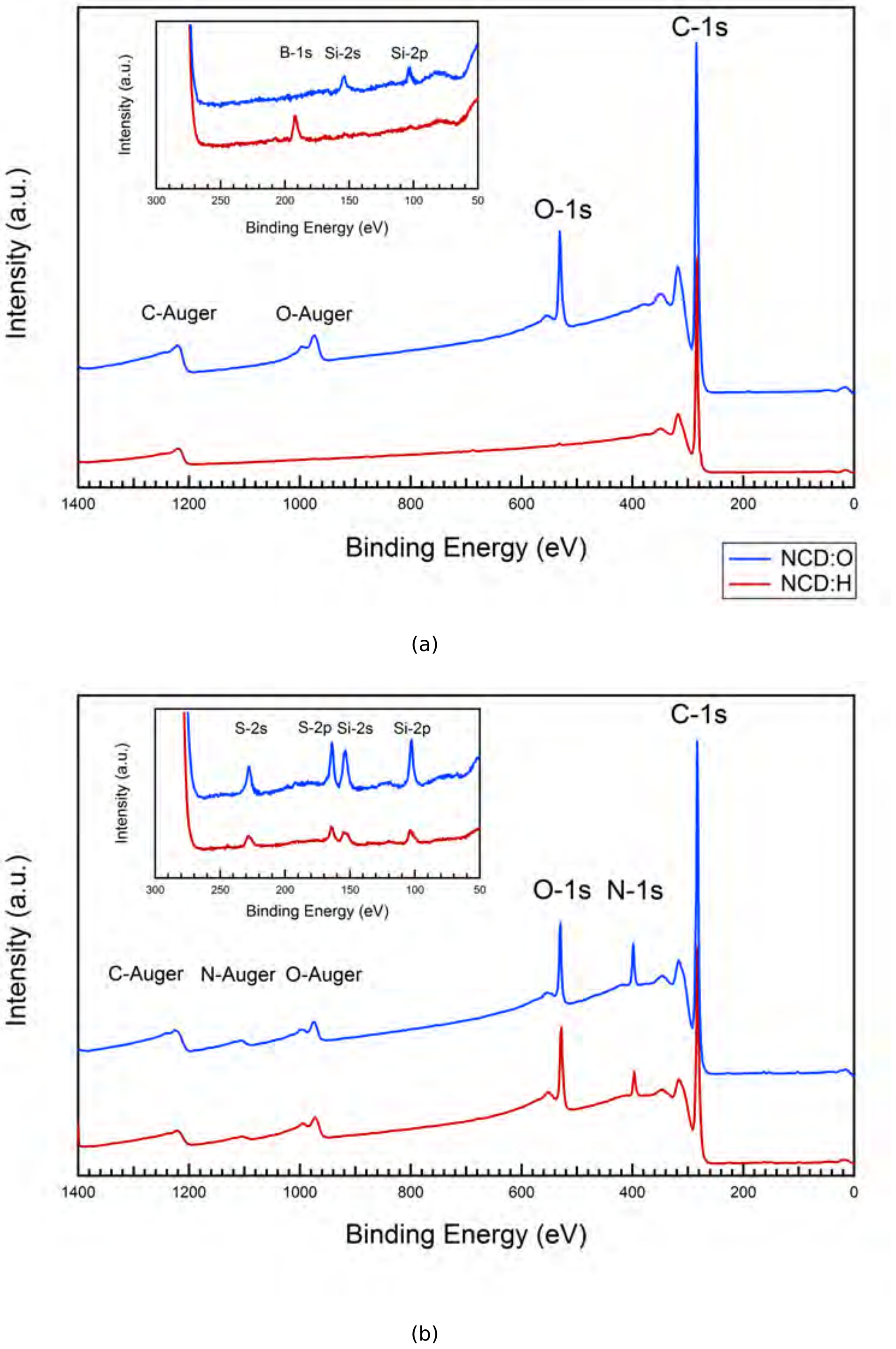

Figure 4.7: XPS spectra of nanocrystalline diamond films. In the upper panel survey scans of oxidized (red) and hydrogenated (blue) diamond. The bottom panel shows survey with high resolution inset of the protein functionalized surfaces. The legend is shared for both graphs.

Theoretical model

According to literature there are between 20 and 34 sulfur containing amino acids distributed over a total estimate of 1200 amino acids for the entire protein. If an average of 10 atoms per amino acid was used, it forms a theoretical approach of 0.22±0.06% sulfur content per protein. The measured spectra contained carbon and sulfur peaks. According to Eq. 4.2 the carbon signal originates not only from the diamond surface but also from the proteins. In contrary to the sulfur signal which can only originate from the proteins (Eq. 4.1). In Figure 4.8 a schematic representation of the two theoretical boundaries is shown. In the upper panel, the photo electrons only contain the sulfur information (I_S) of a single protein (Eq 4.1) and carbon (I_C) of the substrate ($I_{C_{NCD}}$) and from a single protein ($I_{C_{prot}}$) as is shown in Eq 4.2. In this case, the [S/C]-ratio would diminish to extreme low values beyond the detection limits (Eq 4.3).

$$I_S = I_{S_{prot}} \tag{4.1}$$

$$I_C = I_{C_{prot}} + I_{C_{NCD}} \tag{4.2}$$

$$Ratio = \frac{I_{S_{prot}}}{I_{C_{prot}} + I_{C_{NCD}}} \tag{4.3}$$

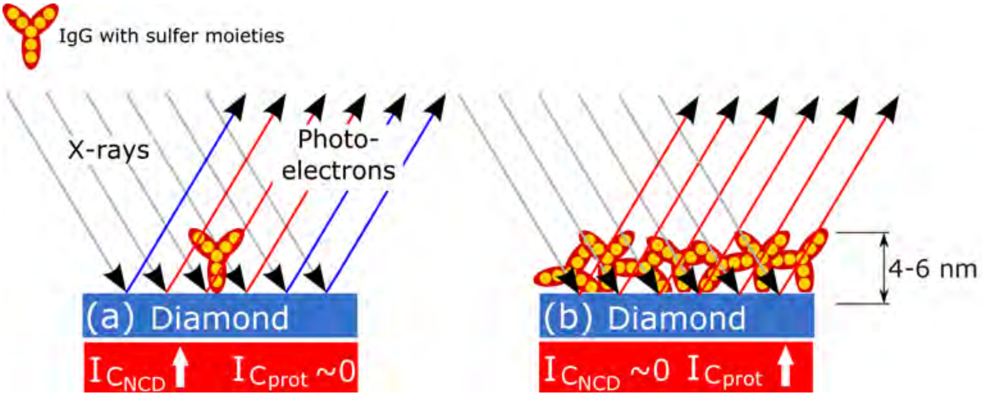

Figure 4.8: Model for XPS analysis of protein coverage. In the upper panel the scenario for a single molecule is shown. Only partial information is wrapped in the photoelectrons but the background is dominating. In the bottom panel a complete coverage is shown with the expected ratio of sulfer to carbon.

In the case of a complete coverage (panel (b)), the carbon intensity is now dominated by the $I_{C_{prot}}$ resulting in a [S/C]-ratio corresponding to the theoretical predicted values.
The experimental quantification was done by the Shirley integration of the XPS peaks after background correction. The absolute values are shown in Table 4.4.

Table 4.4: Peak intensities for protein covered oxidized and hydrogenated diamond surfaces. With σ photoelectric cross-section for the atomic orbital of interest (cm^2)

	Oxidized	Hydrogenated	σ
I_{C-1s}	7.62e5	6.98e5	0.013
I_{S-2s}	2.94e3	2.8e3	0.019
$\frac{I_{S,rel}}{I_{C,rel}}$	0.274%	0.287%	

The integrated peaks are absolute values and material dependent so a relative value needs to be obtained by correcting for the photoelectric cross section σ. Normally, a more elaborate approach is employed but in this case a simplified equation can be used:

$$I_{exp} \sim C \cdot \sigma \tag{4.4}$$

Here, I_{exp} is the experimental intensity, C is the atomic concentration, σ the photoelectric cross-section for the atomic orbital of interest. These intensities were used to calculate the final [S/C]-ratio resulting in 0.274% for the oxidized diamond and 0.287% for the hydrogenated diamond. These experimental obtained values are in excellent agreement with the theoretical predicted values. Indicating a dense and well packed protein layer is present on both diamond surfaces without a clear difference.

4.4.3 Conclusion

From these results we can conclude that proteins are present on both surfaces in a very dense and well packed layers. Also, no significant difference in coverage was observed between the NCD:H and NCD:O. Unfortunately, due to the thickness of the protein layer and the limited depth of information, any substrate information is blocked and cannot be used to quantify the exact protein coverage. We can assume that IgG's are globular proteins and when packed in the densest configuration, $2.8e^{11}$ receptors per mm^2 are present, and even higher numbers are possible in case of multilayer stacking.

4.5 In-situ study of protein adsorption

Current techniques to study protein adsorption can be classified under optical techniques, such as optical waveguide lightmode spectroscopy, total internal reflection fluorescence and ellipsometry and under non-optical techniques, such as the quartz crystal microbalance. Both techniques have advantages and drawbacks. The optical techniques show lack for precise kinetic adsorption data, the need for labeling with fluorescent dyes and transparent substrates. The non-optical techniques show sensitivity for viscous drag of the liquid contacting the surface and need piezoelectric properties of the transducer. Here, the semi conductive properties of B-NCD and electrochemical impedance spectroscopy are combined in order to monitor molecular changes at the interface without the need for any visualization methods.

4.5.1 Experimental

Thin B-NCD on silicon substrates were grown using a 3% [C/H] mixtures and 200 ppm TMB as dopant in an ASTeX reactor as described in [31]. Hydrophobic diamond was prepared by hydrogenation in a H_2 plasma (50 Torr, 800°C, power 4000 W, 1 min). The hydrophilic diamond was prepared by uv-ozone oxidation as described in section 4.2. An ELISA amplification system based on the cyclic redox reaction of NADH/NAD+ was obtained from Invitrogen (Merelbeke, Belgium). Unlabelled and alkaline phosphatase (AP)-labeled anti-CRP monoclonal antibodies and their specific antigen CRP were synthesized by Scipac (Kent, United Kingdom). Fluorescence measurements were done with a goat-anti mouse IgG labelled with an Alexa-488 fluorophore (Sigma Aldrich, Belgium). EIS measurements were done on the HP4149A by applying a 50 mV AC voltage (U) in sweeps of 50 frequencies ranging from 100 Hz to 1 MHz (Figure 4.9). No DC-offset was used. Spectra were taken in an incubator oven (Binder, Germany) at 37°C and were modeled with ZSimpWin. The electrochemical setup consisted of a working electrode (NCD-film) and a platinum counter electrode. No reference electrode was used. Images obtained with the CFM were normalized versus the background to quantify the intensity. The biological activity was shown by ELISA.

4.5.2 Results

The hydrogenated diamond was implemented in the measurement setup and after a stabilized impedance signal was obtained in 1 × PBS, 20 nM antibodies were added. After reaching a new equilibrium after adsorption, the NCD:H was taken out for thorough cleaning in the $H_2SO_4 + KNO_3$ mixture. Finally the sample was oxidized via the uv-treatment and re-implemented in the setup for measuring the protein adsorption on oxidized diamond.

After pinpointing a specific frequency, the time-resolved impedance (TRI) was monitored. In Figure 4.10 the TRI of the adsorption process on NCD:H (panel (a)) and NCD:O (panel (b)) is shown at 100 Hz. These plots contain not only the normalized modulus ($|Z|_t/|Z|_{t=0}$) in function of time but also the corresponding phase ($|P|_t/|P|_{t=0}$).

When proteins adsorb on the diamond surface the impedance modulus

(a) (b)

Figure 4.9: Instrumentation used for the time resolved impedance measurements with in (a) the HP4194A impedance analyzer with home-made software on the Labview platform and in (b) a home made single channel flow cell with Pt counter electrode.

increases and the phase angle decreases. This change is directly proportional to the adsorbed proteins on the surface. When protein adsorb there is first an initial rate of adsorption which shows a fast and linear behavior followed by a slower phase in which kinetic effects start to dominate. In Figure 4.11 this behavior is shown with in panel (a) the NCD:H and (b) the NCD:O.

From the TRI plots in Figure 4.10, two significant differences are present between the NCD:H and NCD:O surface:

- The difference in adsorption time
- The difference in impedimetric magnitude and behavior

First the adsorption time: The modulus and phase plots were fitted with a Boltzman fit to obtain an estimation of time constants. The NCD:O reached a saturation after 16 minutes with a time constant of 6.9 min (Figure 4.10 (b)) whilst the hydrogenated diamond saturates after 30 minutes with a time constant of 14.6 min (Figure 4.10 (a)). So for NCD:H the impedance nearly doubled in adsorption time compared to NCD:O. To understand this adsorption behavior we first focus on the nature of proteins. Antibodies are globular proteins with a high water solubility.

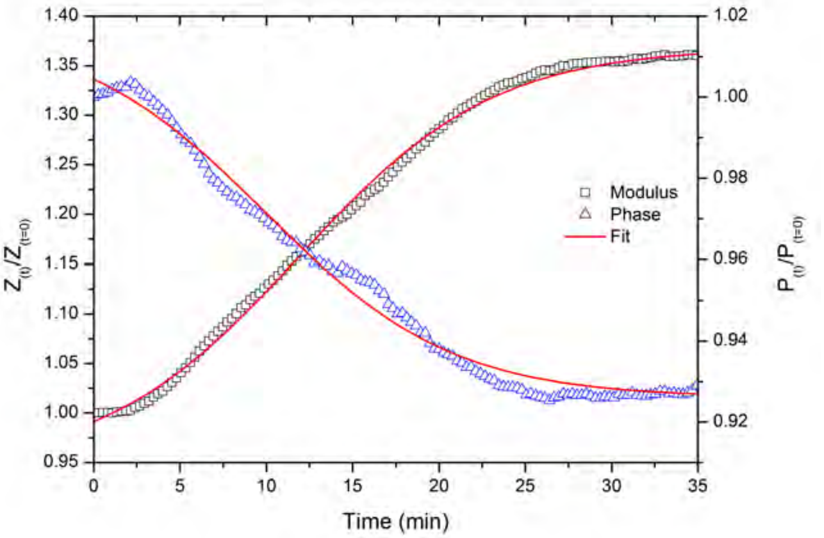

(a)

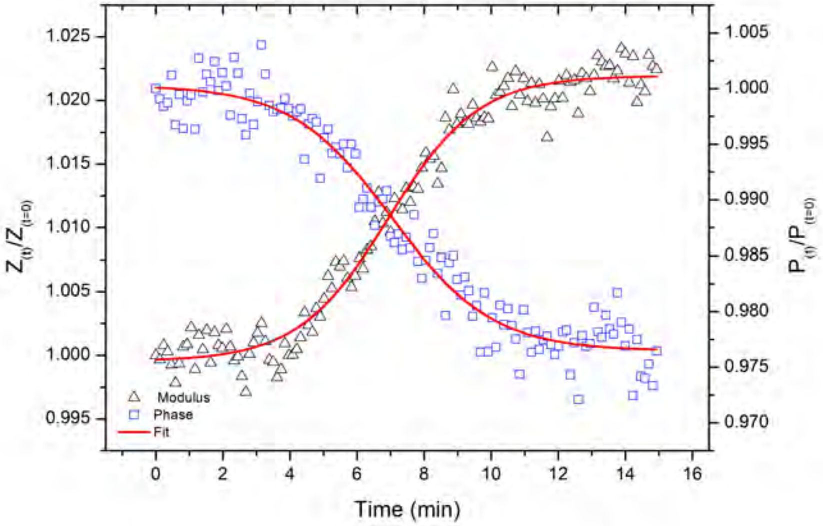

(b)

Figure 4.10: TRI plots of protein adsorption, the modulus and phase were both normalized to the point of addition and plotted in function of time. In panel (a) the result of the hydrogenated diamond is shown and in (b) the oxidized diamond. Both TRI's have been fitted with a Boltzman curve.

These proteins fold into organized, compact and roughly spherical shapes in a way which allows hydrophobic amino acid side chains to localize on the inside of the sphere while the hydrophilic side chains are localized on the interface with the aqueous medium. The natural structure of proteins is dictated by their amino acid sequence, their interaction with solvent molecules, the pH and the ionic composition of the solvent. Their quaternary structure tends to fold in such a way that they form the most stable i.e. lowest free energy structure. Note, this form is also responsible for their biological activity.

From section 4.2 we learned that oxidized diamond has a large polar character causing low water contact angles. The presence of these polar groups at the suface facilitates the adsorption of proteins, which also have their hydrophilic groups located at the protein/water interface resulting in a faster equilibrium.

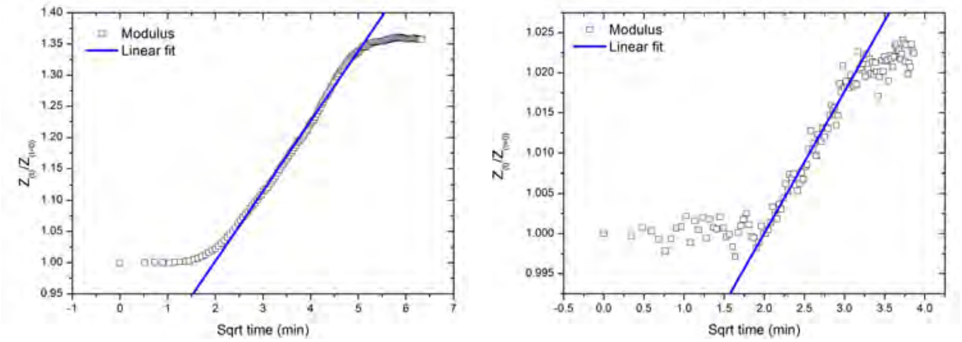

(a) (b)

Figure 4.11: Initial rate of protein adsorption for the NCD:H (a) and NCD:O (b) surfaces.

The second large difference is the impedimetric magnitude: For NCD:H the impedance nearly doubles in adsorption time and the impedimetric response is more than a tenfold larger than the NCD:O. These changes were observed at 100 Hz. By constructing the Nyquist plots of the entire frequency range, specific frequency dependent characteristics can be studied. In Figure 4.12 the Nyquist are shown of different time intervals (t=0, t=15 and t=30). In panel (a) the NCD:H is shown and in (b) the NCD:O. The modeling was done with the equivalent circuit R(QR)(QR) which is further described in Figure 4.13. Qualitative fits were obtained with a χ^2 less than 10^{-4}. The selection of the appropriate model fulfilled the Boukamp theorem and is therefore the most relevant [98]. The mathematical values obtained from these fits are shown in Table 4.5

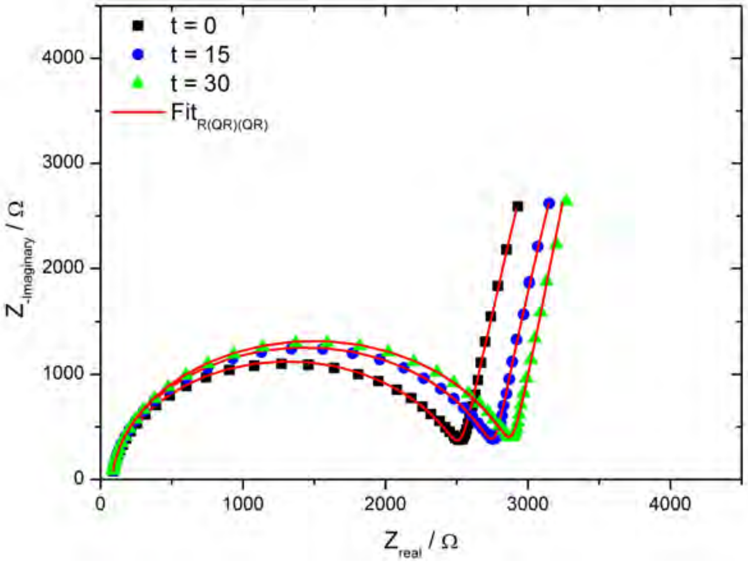

(a)

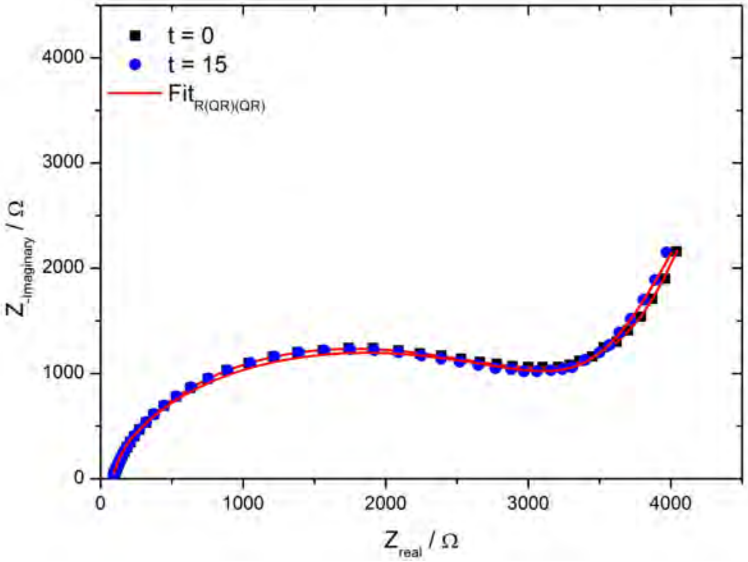

(b)

Figure 4.12: (a) Nyquist plot of before, during and after adsorption of proteins on hydrogenated diamond (NCD:H), (b) Nyquist plot of before and after protein adsorption on oxidized diamond (NCD:O). Both Nyquist plots are fitted with the R(QR)(QR) model.

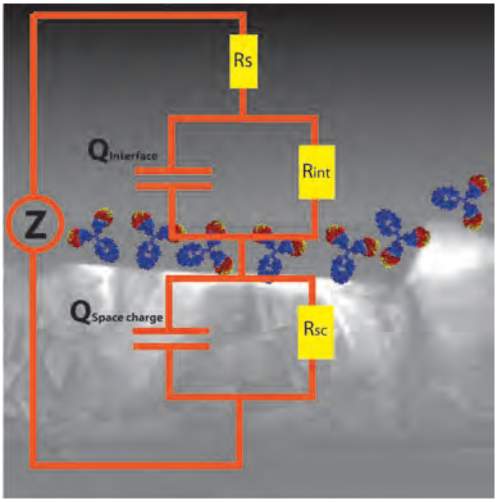

Figure 4.13: Cartoon of protein adsorption at the interface of a diamond film shown with the equivalent model R(QR)(QR). With R_s as the series resistance, Q_{dl}, R_{dl} the double layer capacitance and resistance. Q_{sc} and R_{sc} the space charge capacitance and resistance. The capacitors are treated as Constant Phase Elements (Q).

From these Nyquist plots and the modeled values large differences can be seen between the NCD:H and NCD:O. The nature for these impedimetric changes originate from two different effects, firstly the morphological behavior at the interface and secondly charging effects on the space charge capacitance.

In any case, the R_{series} is not influenced by protein adsorption. The double layer capacitance (Ox-Q_{dl}) decreases after adsorption indicating morphological changes at the interface. The impedance of the constant phase element (Q) is:

$$Z = \frac{1}{(Qi\omega)^n} \tag{4.5}$$

To obtain a better insight in the capacitive changes, a pseudo capacitance can be calculated from the constant phase element (Eq. 4.6).

$$C = Q_{dl} \times (Q_{dl} \times R_{dl})^{\frac{1-n}{n}} \tag{4.6}$$

For further focus on the capacitance Eq. 4.6 can be expanded to Eq. 4.7:

$$C = \epsilon_r \epsilon_0 \frac{A}{d} \tag{4.7}$$

With ϵ_r the relative permittivity, ϵ_0 the vacuum permittivity, A the surface area and d the distance between charges. So from Eq. 4.7 it can be seen that the double layer capacitance is sensitive to changes in the relative permittivity ϵ_r and thickness d. The permittivity of water is 78 and when proteins adsorb the permittivity at the interface decreases. Also the presence of proteins cause a charge separation at the interface causing d to increase. So both elements are responsible for the decrease of the interface capacitance.

In NCD:O solely the morphological effect on the interface can be seen. For the NCD:H this decrease in Q_{dl} is also present but there are also additional changes. These changes are due to the protein behavior at the interface. Once a globular protein (hydrophilic outer shell) adsorbs on a hydrophobic surface, a conformational change occurs. Therefore, creating a denser and more adhered layer causing an augmented effect on the double layer parameters. Interestingly the H-R_{dl} decreases after adsorption. This effect was also observed by Rezek et al. in which they state that proteins decrease the electrolyte electronic barrier induced by C - H dipoles and facilitate another route for charge transfer across the interface [99]. AFM studies from literature on protein conformation and thicknesses on diamond in solution show a larger thickness on oxidized- in comparison with hydrogenated diamond [99, 100]. This is caused by the hydrophobic protein core that remains surrounded by hydrophilic parts upon adsorption on a hydrophilic surface. In our case the Q_{dl} decrease is much higher on NCD:O than on NCD:H diamond which indicates that the protein thickness is larger on NCD:O. Besides the Q_{dl} and R_{dl} an interesting parameter is the associated n value of the constant phase element. The fact that it reduces on oxidized- and increases on hydrogenated diamond suggests a different protein behavior at the surface. As mentioned before, proteins tend to exfoliate their hydrophobic inner part to a hydrophobic surface, therefore creating a tight packing and reducing the roughness. The reduction in roughness results in an increase in the H-n_{dl}. For the oxidized diamond surface the Ox-n_{dl} decreases because proteins are settling without conformational changes. A schematic representation is shown in Figure 4.14. This is also confirmed in literature where a similar effect is found by AFM studies of protein adsorption on diamond [101].

Besides the capacitive changes there is an additional effect. After plasma hydrogenation the diamond surface has C-H bonds creating positively charged dipoles that originate from electronegative differences. At the diamond/liquid interface there is a band bending profile (space charge region) due to the low doping of the diamond. The energy band of the H-terminated diamond surface moves upward to form an accumulation layer of holes near the surface. If negative charges are present at the surface, the energy band bending of the hydrogen termination can be enhanced and therefore causes the impedance to increase. The ionic properties of proteins, determined primarily by their amino acid side chains, are pH dependent. The iso-electric point (IEP) is a pH value by which the net overall charge is zero. Antibodies have an IEP around pH 6 giving them a slight negative charge at pH 7.4. According to Eq. **??** the screening length of a particle in an electrolyte with physiological salt concentrations (±150 mM) is less than a nanometer (0.8 nm) so in case of hydrogenated diamond the proteins are wetting the surface more than on hydrogenated diamond and therefore cause such effects on the space charge capacitance.

Additional data obtained from ELISA show colorimetric results of the biological activity (Figure **??**). A higher biological response of the adsorbed proteins on the oxidized diamond in comparison with the hydrogenated diamond is obtained.

The time and impedimetric response for the hydrogenated diamond doubles and prolongs respectively. Protein unfolding and rearrangement upon adsorption on the hydrophobic surface are responsible for this effect. Figure 4.15 shows the ELISA results. This immunologic technique provides crucial information about the biological activity of the adsorbed proteins. A doubled biological activity for the NCD:O in comparison with the NCD:H

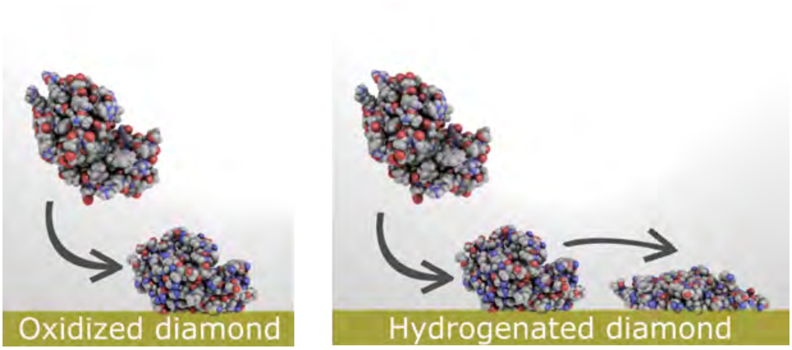

Figure 4.14: Schematic representation of protein adsorption on hydrogenated and oxidized diamond. In the case of NCD:H the proteins tend to increase the wetting compared to NCD:O.

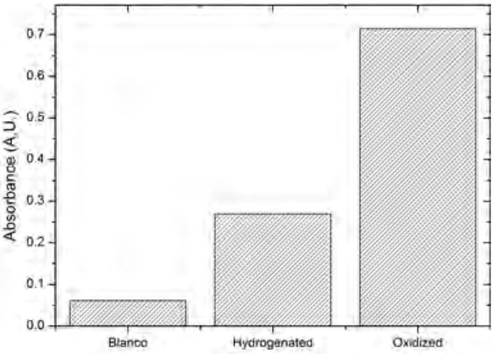

Figure 4.15: ELISA results as biological assay with the immunogenic complex for the oxidized and hydrogenated diamond.

was measured.

Table 4.5: Fit results for the equivalent model for the oxidized (Ox-) and hydrogenated (H-) diamond samples. The components represent: the solution and electrode resistance (R$_s$), the double layer at the interface Q$_{dl}$,n$_{dl}$ and R$_{dl}$ and the space charge region in the diamond film Q$_{sc}$,n$_{sc}$ and R$_{sc}$.

Symbol	Oxidized		Hydrogenated		
	Before (t=0min)	After (t=15 min)	Before (t=0 min)	During (t=15 min)	After (t=30 min)
R_s (Ω×cm)	80.36	79.96	77.77	79.21	79.15
Q_{sc} (S × sec^n/cm^2)	4.21e^{-8}	4.31e^{-8}	4.92e^{-9}	3.92e^{-9}	3.80e^{-9}
n_{sc}	0.856	0.854	0.940	0.954	0.955
R_{sc} (Ω×cm)	2771	2791	2430	2667	2794
Q_{dl} (S × sec^n/cm^2)	6.92e^{-6}	6.60e^{-6}	1.14e^{-6}	1.01e^{-6}	9.63e^{-7}
n_{dl}	0.876	0.854	0.905	0.920	0.925
R_{dl} (Ω×cm)	3.81e^5	1.16e^5	2.31e^5	9.42e^4	7.27e^4
χ^2	1.19e^{-4}	6.37e^{-5}	1.19e^{-4}	6.37e^{-5}	5.94e^{-5}

The reduced signal for the hydrogenated diamond indicates that proteins partially lose their biological activity due to conformational changes when adsorbing on hydrophobic diamond and therefore confirm previous results. These results are also in good agreement with Hoffman et al. [102].

4.5.3 Conclusion

By combining impedance spectroscopy and boron doped nanocrystalline diamond with hydrophobic or hydrophilic properties it was possible to study the time resolved adsorption behavior of globular proteins. This in situ, real-time study of protein adsorption withholds kinetic and protein behavioral information. We learned that hydrophilic diamond yields in a lower impedimetric response but results in a larger biological activity according to ELISA. Probably because polar interactions between the protein and the interface do not promote conformational changes. In addition this also results in a faster adsorption rate. However, the use of oxidized diamond in impedance measurements requires low noise levels and stable conditions because only small capacitive interface changes occur. Hydrogenated diamond on the other hand is a favorable electrode material because it has a space charge sensitivity for the negative charged proteins resulting in a larger response. However a drawback is the partial loss of protein conformation. This yields in a stronger adsorption of proteins on the surface which has an augmented effect on the interface capacitance and additionally creates space charge effects. A question that rises with the obtained results is: Can hydrogenated diamond provide a sensitive surface for protein detection? Unfortunately there is no ideal scenario with a high biological affinity and a large impedimetric response so regarding the noise levels of the signals, and the magnitude of response and the loss in biological functionality we continue to use the hydrogenated diamond as biosensor sensor substrate.

4.6 Biofunctionalization of diamond

Grafting linker molecules on diamond is an important topic for biosensor research. However the application of the functionlization pathways haven’t been employed extensively throughout this work, we still summarize the most important and straight forward possibilities for oxidized and hydrogenated diamond functionalization. Depending on the molecule that needs to immobilized it is important to have the right functional groups on the surface. Next these groups can be combined with coupling chemistry (such as EDC/NHS) to provide a chemical linkage between the surface and the molecule. The reference molecule in the following sections is a short fluorescent labeled 8 basepair DNA strand (described in section **??**). DNA is used for 3 main reasons, it cannot crosslink since it only has a single functional group, secondly the washing steps can be stringent so adsorbed DNA is rinsed off whilst covalent bound remains tethered to the surface and third it contains a fluorescent label allowing fluorescence read-out. In Table **??** an overview is given on the possible diamond surface functionlizations. Some of these techniques were already described in literature but they were also employed in this topic with the scope as suitable surfaces for future biomolecule coupling on diamond substrates.

	Oxidized	Hydrogenated
-COOH	Succinic acid	Fatty Acid, diazonium
-NH2	Silanization	TFAAD

4.6.1 Carboxyl functionalization

In the following paragraphs the carboxyl functionalizations of diamond are discussed:

10-undecenoic acid (fatty acid)

A pure 10-undecenoic acid solution (Sigma, Bornem, Belgium) was added to freshly hydrogentated diamond samples and sandwiched between a quartz lid. Next they were placed in a low-pressure mercury lamp (Philips, TUV-G4T4 4W) which exposed the surfaces for 20 hours. The calculated intensity at the diamond surface is 14 mW/cm^2. After coupling the samples are 20 minutes washed in hot acetic acid at 120°C and finally rinsed in 3 runs of first 5 minutes in dH_2O by ultrasonic agitation and heated dH_2O respectively. After drying under nitrogen a grafted surface with carboxylic acid groups is obtained. It is essential that the surface is hydrogen terminated and exposed to UV in order to tether the linker molecules properly

(Figure 4.16). The carboxylic acids can be used for coupling DNA to the surface as has been described in section 2.4.1.

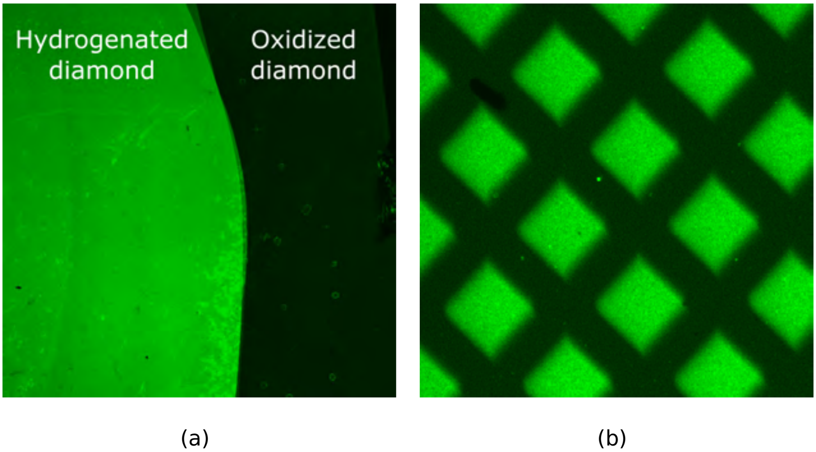

(a) (b)

Figure 4.16: In panel (a) a partially hydrogenated/oxidized surface exposed for fatty acid coupling and in (b) selective illumination of the fatty acid linkers..

Succinic anhydride

In contrary to the fatty acid coupling the succinic anhydride does not require a hydrogenated nor UV exposure to the surface. This surface modification is done in dry acetonitrile (ACN) on thoroughly oxidized diamond surfaces. A 0.8 M solution was prepared and added to the substrates under a nitrogen atmosphere with continuous shaking for 20 hours.
Afterwards the samples are 3 times washed for 5 minutes in ACN and dried under a nitrogen flow. After 8bp DNA coupling the fluorescence recordings indicate a succesful result on the positive sample compared to the negative control.[103].

4-benzoic acid diazonium

An additional carboxyl functionalization of the hydrogenated diamond surface was by grafting the surface with diazonium salts. The diazonium used in this work was the 4-benzoic acid diazonium tetrafluoroborate. The chemical structure and coupling mechanism is shown in Figure 4.18. The diazonium was prepared in house following the recipe of Kizil et al. The obtained product was characterized by NMR and FTIR both indicating good functionalities. The coupling reaction was carried out with a 8.7 mM reaction in MilliQ with an incubation time of 2.5 h. Afterwards the samples were rinsed for 2 times in MilliQ (10 min) and dried before used in EDC coupling. However, the diazonium result is less pronounced with respect to the succenic anhydride and the fatty acid routes.

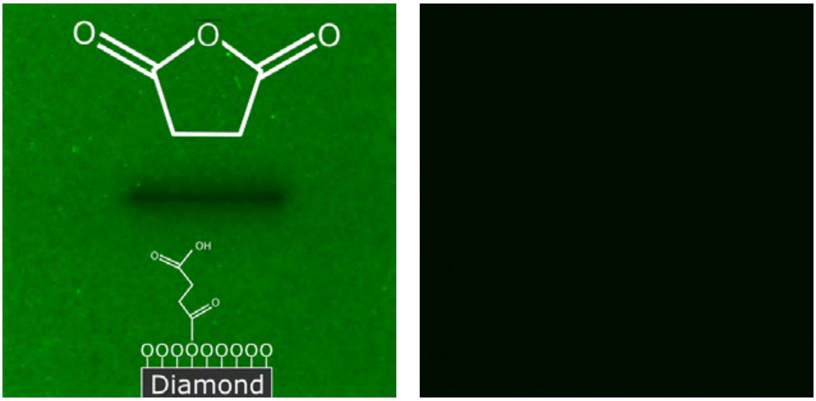

(a) (b)

Figure 4.17: In panel (a) a succenic anhydride functionlized substrate and in (b) a negative controle without the reactive compound.

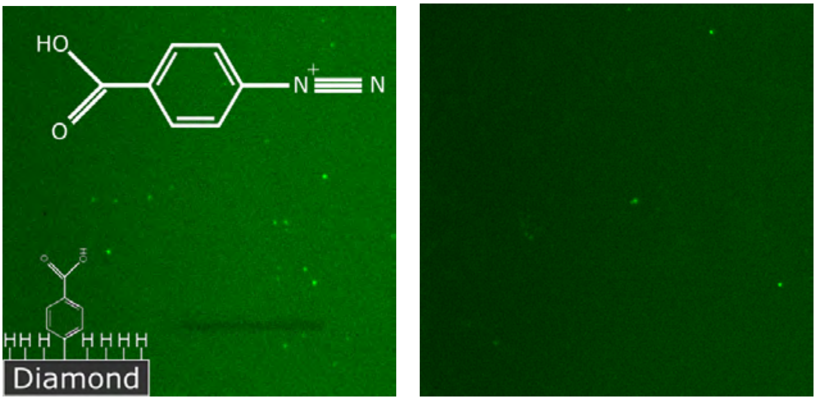

(a) (b)

Figure 4.18: In panel (a) a partially hydrogenated/oxidized surface exposed for fatty acid coupling.

4.6.2 Amine functionalization

Short linker functionalization

The first efforts for diamond functionalization with amine groups in this work were carried out with short molecule linkers. From fatty acid attachment was known that the double bond in combination with UV causes a covalent bond between the linker and the surface. Therefore, a short linker with a double bond and an amine group, such as allylamine was used to graft the surface. However, results were not convincing for this molecule so ethylenediamine was used. Results from contact angles were positive but no coupling with DNA was achieved.

3-aminopropyltriethoxysilane

Diamond silanization is widely described in literature. Depending on the silane, a certain functional group can be used. Here an 3-aminopropyltriethoxysilane (APTES) was used which results in an amine functionalized surface. Silanes require hydroxyl terminated surfaces so the NCD was 2 hours exposed to uv-ozone. Afterwards, were boiled in MilliQ water and finally they were 30 minutes immersed in 2% (v/v) APTES into 95:5 (v/v) EtOH/H_2O at room temperature under N_2 atmosphere. After extensively washing with EtOH and H_2O the samples were dried and baked at 110° for 15 minutes.

Afterwards 8 bp DNA with a carboxyl functional group and fluorescent label was coupled via the EDC-pathway. In Figure 4.19 the recorded fluorescence images are shown with the EDC+ in (a) and the EDC- (b). Contact angles after uv-ozone were 10° and increased to 75° for the silanized and were 25° for the negative control.

4.6.3 Surface regeneration

In addition a large time consumer is the cleaning of diamond for reusing. This involves washing in MilliQ to remove adsorbed salts, washing in acid and re-hydrogenation. Also with the scope of future application in diamond array’s, which are integrated in certain systems, makes it difficult to recycle the complete diamond surface with aformentioned treatments. Therefore efforts have been made to regenerate the functionalized diamond surface. The diamond interfaces are functionalized with fatty acid

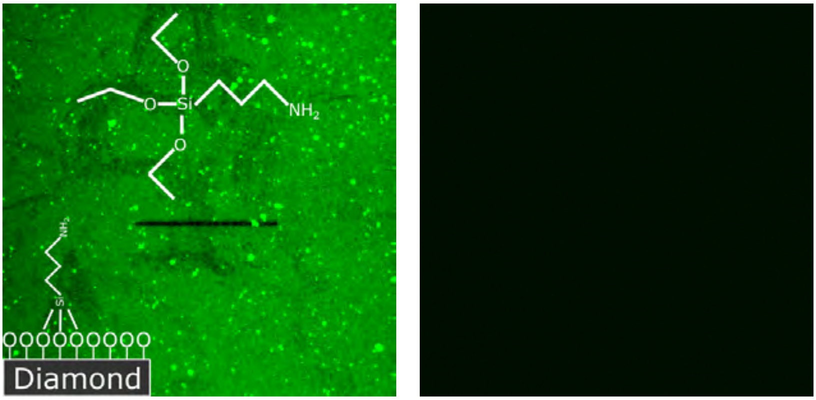

(a) (b)

Figure 4.19: Amino functionalized oxygen terminated diamond. (a) the EDC+ sample with bleachline and (b) the EDC- sample.

linkers and coupled with fluorescent labeled DNA. After confocal imaging the substrates were washed with different procedures in order to break the formed amide bond, regenerate the carboxylic acid group to its proper functionality and re-couple DNAto the surface. Herefore different solutions have been used at different temperatures such as.

The breaking of the amide bond is done by interconversion and nucleophylic acyl substitution (hydrolysis). The enzymatic routes with proteinase

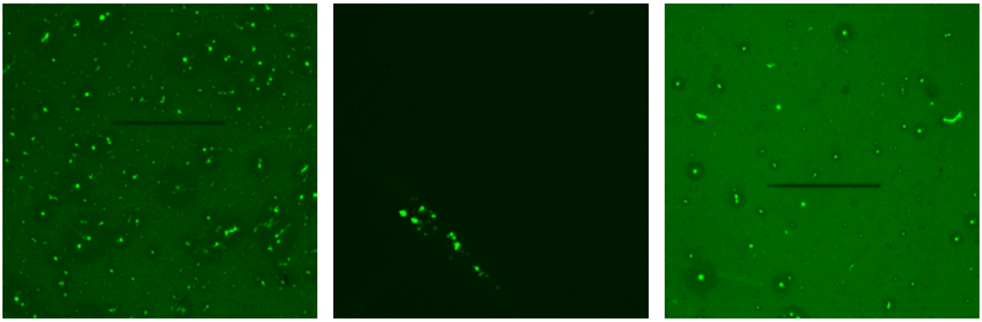

(a) (b) (c)

Figure 4.20: Regeneration of a fatty acid surface with (a) the initial state (b) the removal of DNA strands (c) re-functionalization with 8bp-Alexa488 label

K, Pepsine A and α-chymotrypsinogen were supposed to break the amide bonds but this did not fulfill the expectations. Heating MilliQ water from 30 to 120 °C also did not result in signifcant changes. Acidic washin with 10 M NaOH, 1 M NaOH and 0.1 M NaOH at RT, 80 and 120 °. This resulted in succesfull decoupling, but the re-coupling showed excessive striations and spots. Finally acdic washing with 10 M H_2SO_4 at room temperature for 2hr30 resulted in successfull de/re-coupling as can be seen in Figure **??**.

4.6.4 Conclusion

The functionalizations of diamond surfaces are a very interesting and imporant aspect in biosensors. Biomolecules can be tethered covalently to a surface. Especially the oxygen termination, which is of large imporatance for future biosensor research not only provides a better surface for proteins, but it also makes life easier. Especially the huge workload that arises from hydrogenation of diamond it is now possible to employ surfaces that can be generated much more rapidly, which the same result and serve as a possible biosensor substrate. Currently the succinic acid coupling is used to investigate SNP detection and is still work in progress. In addition, experiments on supported lipid bilayers on diamond films have also been done but these results are not discussed in this thesis. These results can be found in [104].

Chapter 5

Immunosensing: The search for CRP

5.1 Characterization of the immunosensor

With an enzyme linked immunosorbent assay the bio-functionality of the immunosensor was proven. In section 4.3 we found that the bio-functionality on oxidized diamond was much higher compared to hydrogenated diamond. In this section, we further focus on hydrogenated diamond because of the improved electrical sensitivity. In Figure 5.1 (a) the biofunctionality of the immunosensor construct is shown. Here 4 NCD samples were used as following: two samples were incubated with 20 nM anti-CRP and blocked with BSA (6w%) overnight. The other two were only blocked with BSA. For the antibody/antigen immune complex the largest colorimetric result was obtained (A-CRP + CRP). In BSA+CRP there was no signal measured indicating that CRP does not adsorb on BSA coated surfaces. A-CRP+bfr indicates that the secondary antibody does not cross-bind onto the primary antibody, yielding in no colorimetric change. Similarly the BSA + bfr show there is no random adsorption of the secondary antibody on the BSA blocked surface. Only a clear and significant signal was obtained upon formation of a complete Ab/Ag complex. In panel (b) the sensitivity and specificity versus the antigen (CRP) and a negative control protein, plasminogen, is represented. Plasminogen is a 66 kDa protein with similar structural properties like CRP. In this case all of the substrates have the same concentration for the primary receptor. The blanco, which had CRP-buffer, did not respond. Also, the different plasminogen concentrations did not result in any colorimetric change. The CRP channels showed a concentration dependent behavior. According to these measurements the biological functionality, with high specificity and sensitivity within clinical relevant concentrations is still present. From these calorimetric results we prove the functionality of hydrogenated diamond as a suitable biosensor substrate.

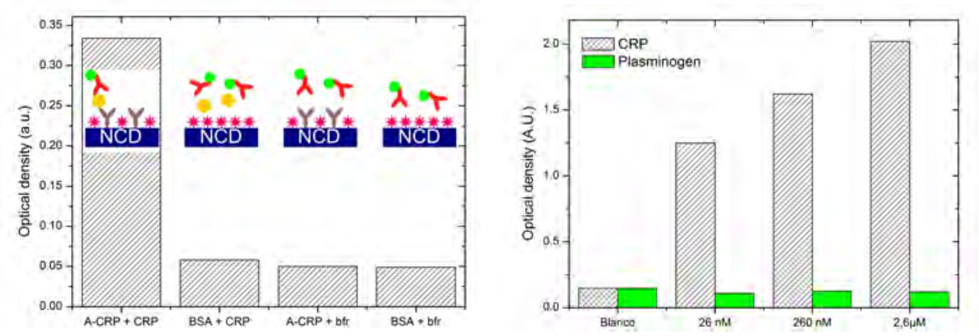

(a) (b)

Figure 5.1: ELISA results indicating the bioactivity (a) and the selectivity/sensitivity of the immunosensor against CRP.

5.2 Label-free immunosensing by impedance spectroscopy

In the section above we demonstrated that hydrogenated diamond has the viability and potential to serve as a suitable biosensing substrate. The next sections will describe the impedimetric read-out based on a label free method. For this the diamond samples were interfaced with the HP4194A impedance analyzer. In Figure 5.2 a schematic and photographs of the biosensor lay-out is shown. Typically impedimetric measurements took place in a 4 well setup with a volume of 140 μl buffer solution. The working electrode was the diamond film and the counter was a gold wire. Next they were connected to a multiplexer, that allowed sequential measurements, which was finally interfaced with an impedance analyzer.

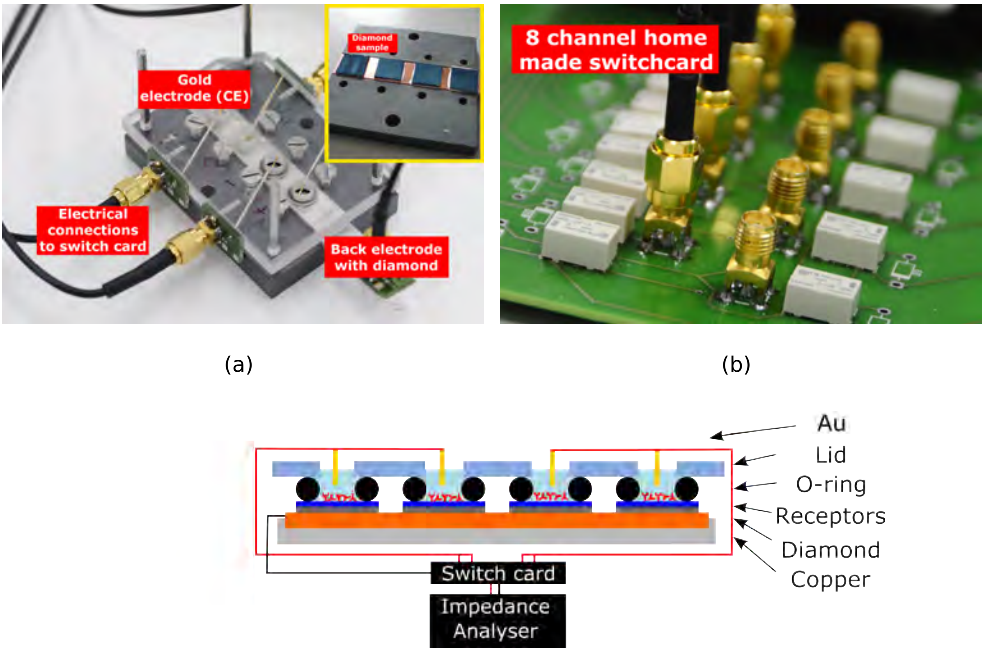

(a) (b)

(c)

Figure 5.2: Photograph (a) shows the measurement cell with the 4 channels and the inset shows the diamond samples. In (b) the switchcard is shown that allowed sequential measurements. In (c) a schematic representation of the measurement setup is shown.

5.2.1 Specificity of the immunosensor

Hydrogenated diamond NCD substrates functionalized with 20 nM anti-CRP and blocked overnight with BSA were implemented in the biosensor. The wells were topped up with 1 × PBS and were stabilized at 37°C. After a stable impedance signal was obtained the proteins, CRP and plasminogen, were added to different wells to reach a final concentration of 500 nM. Note, this point is denoted as (t=0) and is used for data normalization. In Figure 5.4 (a) the time resolved impedance at 100 Hz is shown before, during and after the addition of the proteins. The normalization was done versus the first point *before* protein addition, (t=0). The addition volume is typically 6 μl and causes temperature differences and convection in the liquid cell. This causes the impedance to slightly jump upward (due to the decrease in temperature and disturbances in the molecular layer). Also, after rinsing a similar increase was observed. For trend analysis and general overview this is in an interesting way of representation. However, to further focus on the actual difference between CRP and the negative control protein, the normalization point was now chosen as the first point *after* addition of the proteins. This means that the graph from panel (b) is actually the zoomed in version of (a) and only shows the time resolved data during the protein addition. Here clearly can be seen that the CRP channels increase with 2% over 40 minutes whilst the plasminogen shows a typical decrease, in this case, of ±1%.

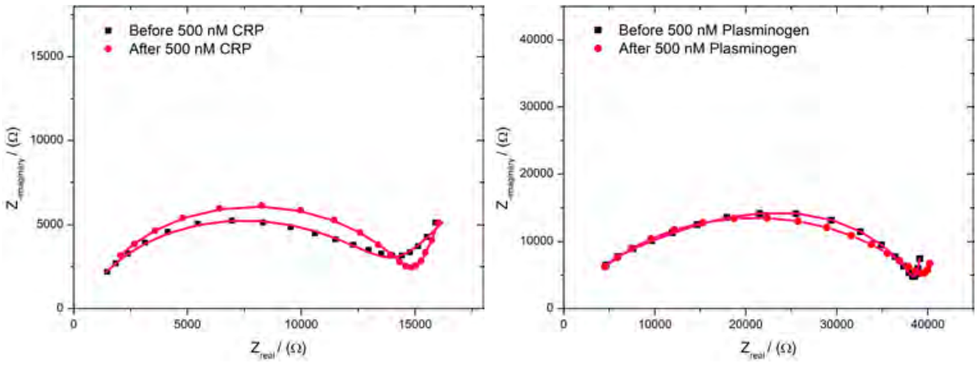

(a) (b)

Figure 5.3: Nyquist plots modeled with the R(QR)(QR). The curves show snapshots at t=0 and t=50 min of Figure 5.4 (b).

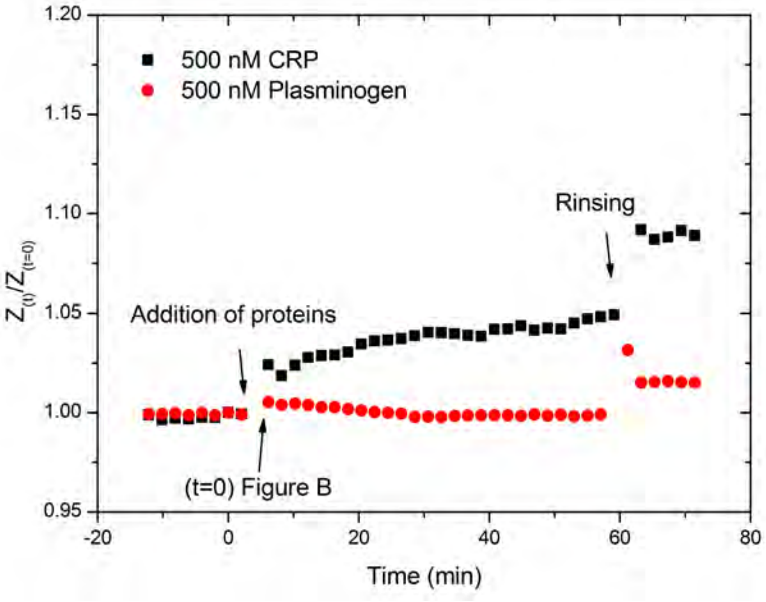

(a)

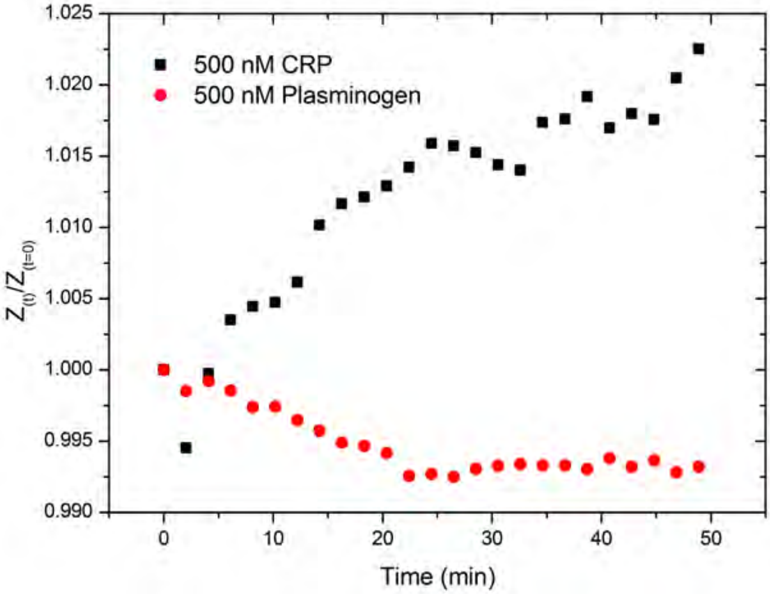

(b)

Figure 5.4: Normalized time resolved impedance at 100 Hz for the addition of 500 nM CRP and plasminogen. In panel (a) the time lapse before, during and after addition is shown whilst in (b) a new point of origin is chosen after addition of the proteins.

For further analysis Nyquist plots were made from t=0 and after addition, t=50 min. They were modeled with the typical R(QR)(QR) and the fitresults are shown in Figure 5.3. The calculated values had indicated the largest change in the double layer capacitance of the CRP channel, on average there was a decrease of 58% and the space charge capacitance (Q_{sc}) increased by ±8%. The plasminogen channel showed no significant changes, here only a 3% increase for both the Q_{dl} and Q_{sc} was observed.

5.2.2 Reliability of the immunosensor

In order to get more insight in the reliability of the immunosensor, a variation on the specificity measurements, that were described above, were performed. First, the diamond substrates were either coated with anti-CRP (NCD+anti-CRP) or just blocked with BSA (NCD). Secondly, instead of measuring the CRP and plasminogen separately in different wells the addition was now done in sequence. First 500 nM plasminogen was added and afterwards 500 nM CRP. The results are shown in Figure 5.5. Also here the time resolved impedance of 100 Hz is normalized versus (t=0). Because there is no complex forming there is also no change in low-frequency impedance and the two channels behave similarly with downward trend.
The TRI decreased with ± 2% and 6% for the BSA blocked and receptor functionlized substrate respectively. In panel (b) of Figure 5.5 CRP was added as the second step after rinsing of the cell. Here also the final concentration was 500 nM. Interestingly, the decrease that was observed in panel (a) upon plasminogen addition is now gone and a upward sloping trend is observed whilst the receptor free surface suffers from the same regression as in (a).

5.2.3 Sensitivity of the immunosensor

The sensitivity of the immunosensor is studied by adding different CRP concentrations. These were 0 nM (CRP-buffer), 10 nM and 100 nM. The time resolved impedance normalized after protein addition (t=0) is shown in Figure 5.6 (a). In panel (b) the concentration versus the relative impedance at (t=40 min) is shown. In the concentration range between 0 and 1000 nM an exponential dependence versus concentration is shown. The data represent the mean value and standard deviation for the change in Z after 40 minutes of CRP treatment. The mean value and standard deviation for pure CRP buffer (0 nM CRP) is indicated by the full line and shaded area, respectively. From this curve it is clear that 10 nM, was the lowest concentration that could reproducibly be discriminated from buffer.

The impedance at 100 Hz changes in a concentration-dependent manner. The different impedance spectra, corresponding to the different CRP concentrations, can be clearly distinguished from each other within 40 minutes. The impedance of the reference channel (triangles) shows a characteristic decrease, while the impedance of the channel with a CRP concentration of 100 nM (squares) is clearly increasing, and shows a comparable behavior to the effect described in Figure 5.4 and Figure 5.5 associated with a decrease in molecular layer capacitance. The impedance of the channel with the lowest CRP concentration (circles triangles), however, already starts to show a slight decrease, suggesting a lower density of antigen/antibody-complexes, and approaching the condition of non-recognition, also seen with buffer and plasminogen treatment.

The real-time impedance spectra observed at 100 Hz in the previous Figures indicate that, when comparing the sample channel to a reference channel in the same measurement, a good discrimination between the two conditions is obtained after 40 minutes. However, because of the reproducibility of the sensor, it is also possible to compare the sample channels of separate measurements. This is illustrated in Figure 5.7, where the CRP-dependent impedance curve (black squares) is the average of 5 independent impedance measurements at 100 Hz on anti-CRP functionalized samples, while the non-specific plasminogen-dependent impedance curve (red squares) is the average of 7 independent impedance measurements at 100 Hz on anti-CRP functionalized samples. The added concentrations were identical to the previous experiments. The error bars indicate standard deviations. It can be seen that, after 25 minutes, the two types of curves significantly diverge, and obtain a range of values specific for reference and sample. The rise in impedance remains consistently characteristic for the specific CRP recognition.

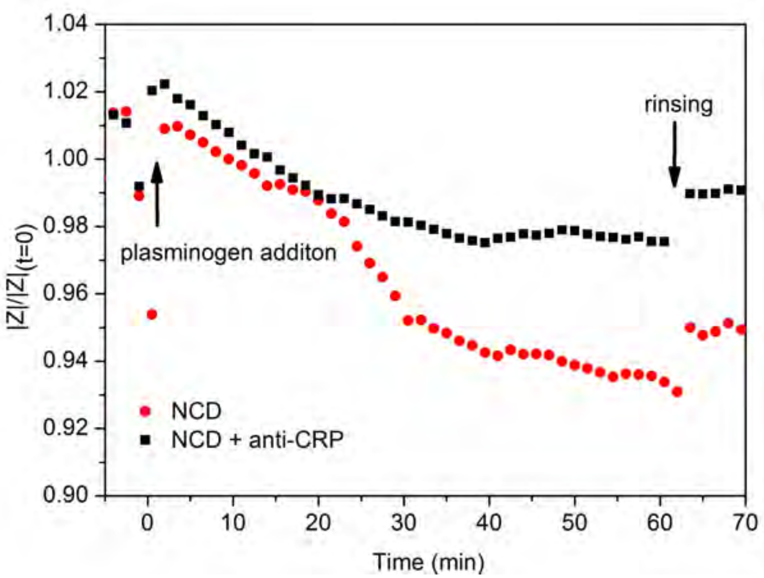

(a)

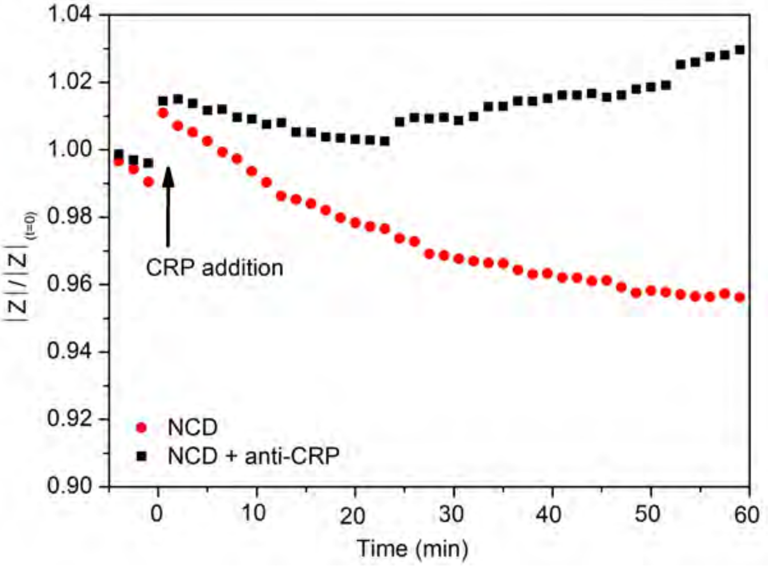

(b)

Figure 5.5: TRI at 100 Hz normalized at t=0 before protein addition. In (a) the plasminogen addition is shown on BSA blocked and anti-CRP functionalized NCD and in (b) the CRP addition.

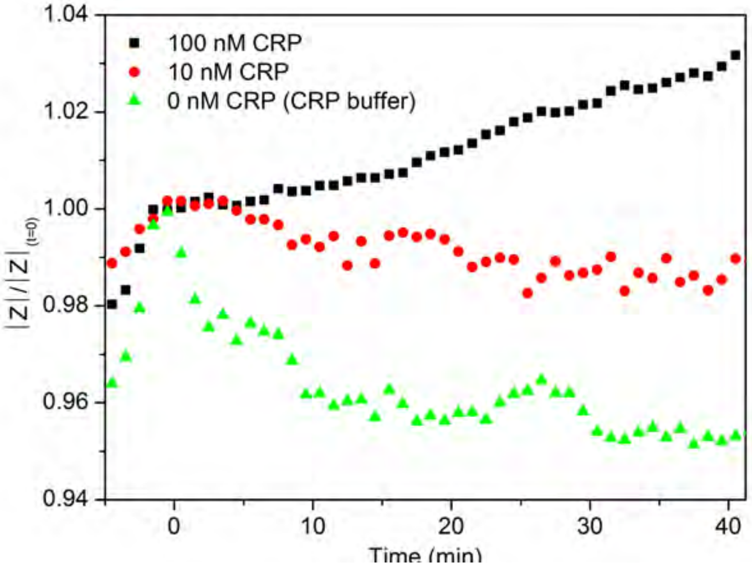

(a)

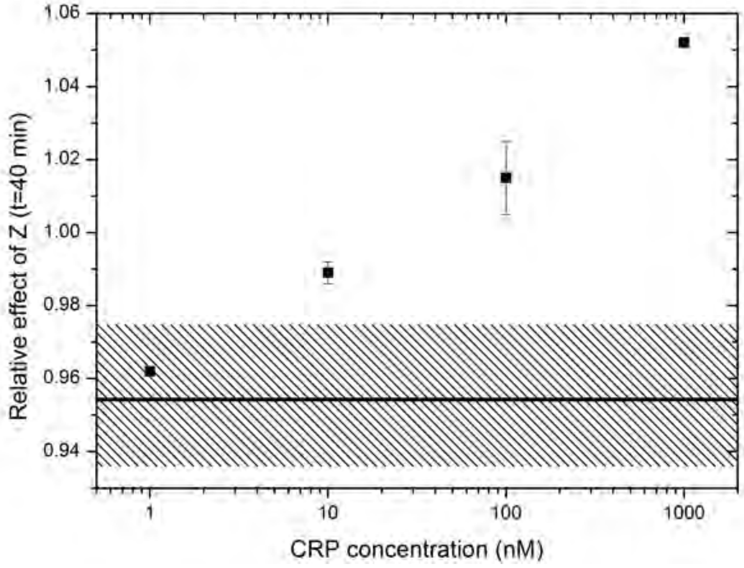

(b)

Figure 5.6: In panel (a) a TRI of 0, 10 and 100 nM Time resolved impedance of different CRP concentrations (0, 10 and 100 nM)

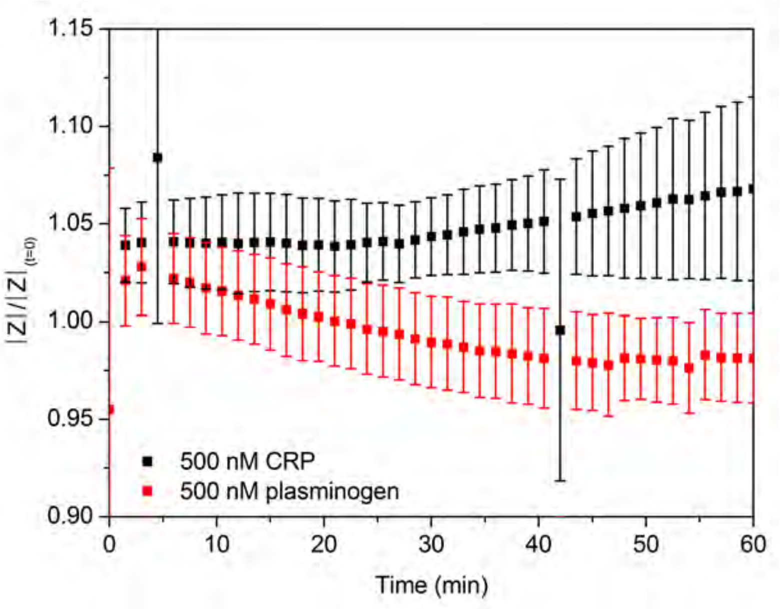

Figure 5.7: An averaging of impedance spectra taken at 100 Hz during 500 nM CRP addition (black) and 500 nM plasminogen addition (red).

5.2.4 Detection of CRP in complex matrix

The goal of the immunosensor was the detection of C-Reactive Protein in crude human serum. For this, blood of a healthy donor was centrifuged (4000 rpm, 20 min, 5°C) to obtain crude serum. As a reference the serum was cross-checked by a specialized institute (Labo RIGO, Genk, Belgium) in which a CRP concentration well below 4 nM were quantified. Compared to buffer solutions the use of complex media such as serum creates additional (unwanted) effects. In Figure 5.10 the time resolved impedance of three different substrates is shown. The first has a bare NCD substrate (red) and the other two are blocked with BSA (black, green). After stabilization, PBS was added to a BSA blocked channel (black) and serum was added to a bare and blocked surface (red and green). After an incubation time of an hour the samples were rinsed and refilled with PBS to record the end phase. The black channel (PBS addition) does not show any significant changes throughout the entire measurement. The serum addition channels (green and red) show impedance increases that correlate to adsorption effects. The BSA blocked surface which is exposed to human serum has an increase of 5% whilst the bare NCD substrate increases up to 20%. From this it is clear that serum has an additional large blocking effect on the surface compared to buffer solutions. This is caused by the high concentrated protein cocktail. Especially the human serum albumin, which is heavily charged and can easily adsorb on the bare surface and can even cause an additional blocking on the other substrate. This effect is also seen in the Nyquist plots. Figure 5.9 (a) shows the initial condition of the bare electrode with the addition of serum and the final phase after rinsing and refilling. The impedance increases not only in the space charge but also in the double layer region. (b) has the similar exposure only the diamond surface is blocked with BSA. This causes a dampened effect on the impedance changes.

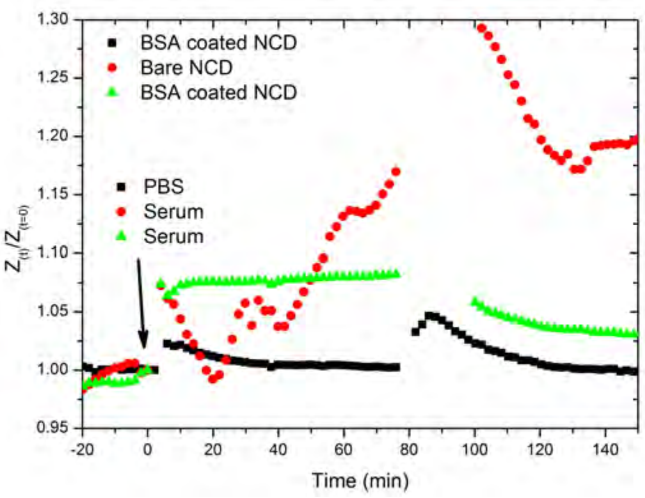

Figure 5.8: TRI curve of NCD samples, the black (square) and green (triangle) are coated with BSA and the red (circle) is a bare substrate. At t=0 PBS is added to one of the BSA coated NCD and human serum to one BSA blocked and one bare electrode.

From these results we learn that if immuno measurements are performed in human serum it is necessary to stabilize in crude (unspiked) serum. Because any addition of bulk protein material causes an impedance increase that could mask the small impedimetric signal that originates from antigen binding. In Figure **??** the average of 6 independent time resolved impedance measurements in serum are shown. The initial phase of stabilization was done in unrefined serum. The proteins were diluted in serum

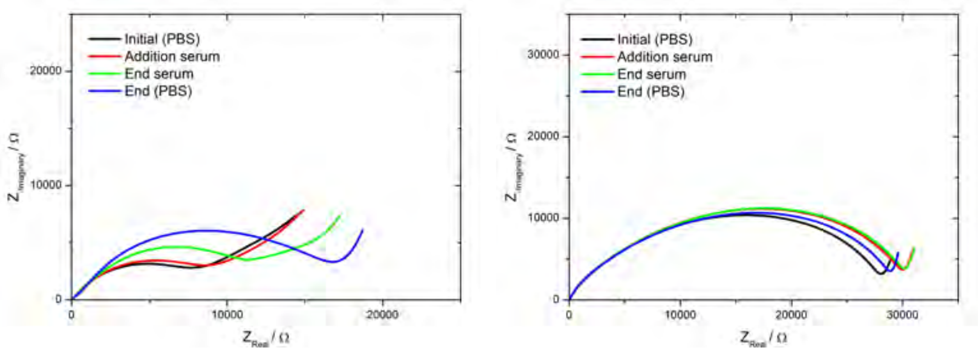

(a) (b)

Figure 5.9: Nyquist plots of different measurement conditions. In (a) a BSA blocked NCD substrate with only PBS additions. (b) a bare NCD substrate with human serum addition, (c) BSA blocked surface with serum addition

and were afterwards added to the sensor. The positive sample received CRP spiked serum that resulted in a 500 nM end concentration whilst the negative control only had CRP buffer diluted with serum.

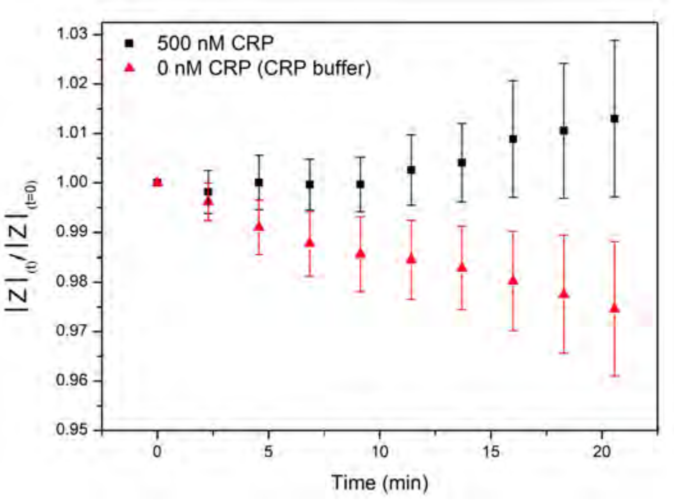

Figure 5.10: TRI of 500 nM spiked serum (black) compared to unspiked serum (red), average was taken of 6 independent measurements.

The negative control shows the typical decrease in impedance signal. The spiked serum causes a characteristic impedance increase of 1.6% after 30 minutes. As compared to the measurements in buffer, shown in Fig. 6, the impedance effect is slightly less, probably due to the high complexity of the medium. However, difference in impedance behavior between spiked and unspiked serum was significant ($p > 0.045$).

5.2.5 Conclusion

In the previous sections the potential of EIS on H-terminated NCD is demonstrated for the development of a real-time and label-free immunosensor. The suitability of this diamond substrate for functional antibody adsorption was demonstrated with an ELISA reference technique. In this study a specific discrimination between CRP and plasminogen was obtained in real-time at low frequencies (100 Hz). Specific CRP recognition by the physisorbed anti-CRP antibodies was consistently associated with an increase in impedance, due to a decreased capacitance of the molecular layer caused by CRP binding. The level of increase varied between 2 and 6%. On the other hand, non-specific conditions, either by the addition of plasminogen or buffer to anti-CRP functionalized NCD or the use of BSA-coated NCD, were characterized by a small impedance decrease at 100 Hz of 5%. The sensitivity of the immunosensor was analyzed by incubating the NCD samples with different concentrations of CRP. At 100 Hz, the lowest concentration of CRP used in our experiments (10 nM) was still clearly distinguishable from the reference channel treated with buffer within 20 minutes. This indicates the possibility that our prototype immunosensor for CRP can reach a sensitivity within the physiologically relevant concentration range, important to discriminate between healthy controls (8 - 10 nM) and patients at risk for CVD (>10 nM). Serum measurements were also performed, and showed that the impedimetric immunosensor was capable of significantly distinguishing between spiked and unspiked serum. However the analyte concentrations is very large and is not within the physiological range. Therefore an amplification of the signal is necessary to achieve a larger impedimetric response so a beter differentiation is possible between various concentrations. In the following sections some efforts for signal amplification are shown such as sensor area increase, gold labeling of proteins, thermal insulation and protein orientation.

5.3 Optimization of sensing properties

5.3.1 Increasing the sensing area

By increasing the surface area it is possible to improve the sensor response. A larger surface area can house more receptors, and therefore increase the sensing effect. In section $refsec : chratio$ we showed that the interface capacitance can be changed slightly by varying the growth poperties but a drastic enlargement is necessary. Therefore, an array of ZincOxide (ZnO) nanorods was grown on boron doped nanocrystalline films to construct a three dimensional structure that not only serves as a possible optimization for the current biosensor, but also serves as a viable proof-of-principle concept for a new generation of biosensors based on a ZnO platform. In literature, up till now, the combination of diamond, serving as a normal electrode, covered with ZnO nanorods and the impedimetric read-out is new and not yet described!

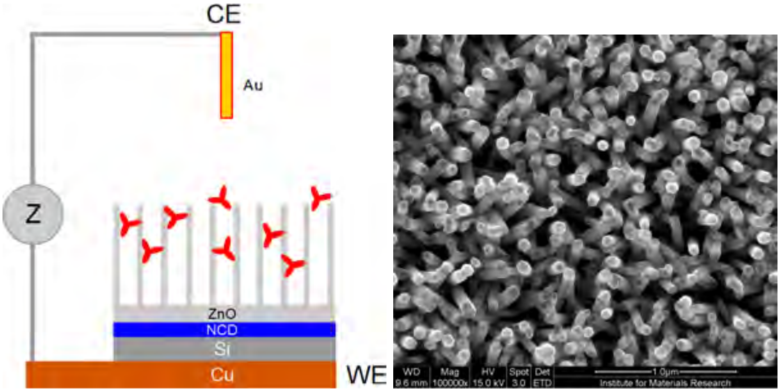

(a) (b)

Figure 5.11: (a) The schematic representation of the sensor setup with the ZnO rods serving as an increased sensor area (b) SEM recording of a bare NCD film (c) NCD film covered with ZnO rods (d) close-up of ZnO rods (synthesis: L. Baeten)

The setup is composed of a B-NCD serving as an electrode, a thin ZnO film (generally 20 nm) on which a ZnO nanorod array was grown (more information about the ZnO synthesis and deposition can be found in [105, 81]. This nanorod array forms the surface in contact with the solution (Figure

5.11(a)) with the surrounding solution. Measurements were done in 1 × PBS at pH 7.4 at 37°C. Measurements were done with the HP and IVIUM impedance analyers in the top-down setup based on the flow-chamber described in [106]. Figure 5.11 shows a SEM recording of the nanorod array. In comparison to a flat surface, roughness of the NCD crystallites cause the nanorods to tilt and therefore open up for so proteins can diffuse more easily and settle in the meshlike surface.

Impedance spectra show besides the typical two hemispheres a third capacitance element that is attributed to the interface of ZnO and NCD. By modeling the impedance spectra with an additional (RQ) element a good fit with a χ^2 of 1.27 e^{-5} is achieved. In total the model comprises R(QR)(QR)(QR) elements, in which each (QR) represents a certain parameter i.e the interface capacitance, the space charge region and an additional diamond/ZnO interface. For normal NCD substrates the interface with the liquid results in a capacitance value that is around 2-5 μF but in the case of the ZnO interface capacitance increased up to 40 μF.

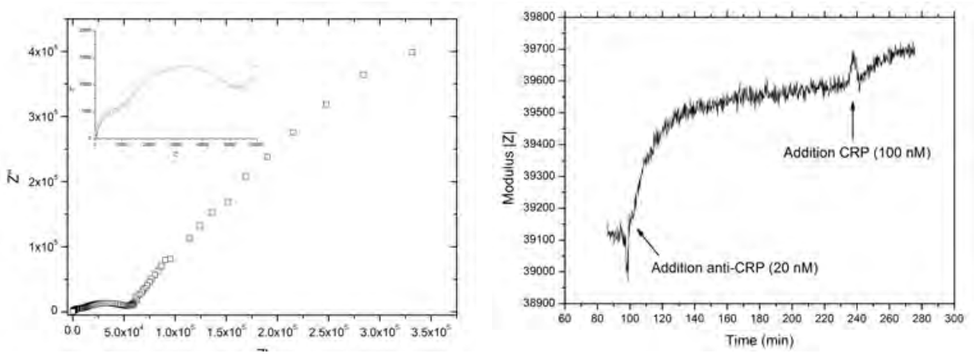

(a) (b)

Figure 5.12: Nyquist plots of the NCD/ZnO-nanorods array in 1 × PBS. (b) the addition of antibodies and target CRP at 100 Hz.

The use of the nanorod array is very interesting in combination with diamond. Besides ITO the only viable substrate for ZnO nanorod growth is diamond because it can withstand the harsh growth conditions without forming any oxide layer (as is the case for silicon). The array can not only be used to capture proteins, but is also a viable immobilization layer for other receptors such as enzymes. The drawback of the ZnO array is the long stabilization time required. Probably the water penetration into the rods (4.5 hours approximately) causes a constant growth of the interface capacitance. If analytes also need to diffuse into this dense array the measurement times are drastically prolonged. Only if the density packing of the nanorod array can be tuned to create larger inter-rod distances, the ZnO array can prove its true potential for biosensing applications.

5.3.2 Labelling proteins with metallic particle

To enlarge the surface sensitve effect, affinity purified polyclonal goat-anti mouse antibodies (H+L chain) with a 10 nm colloidal gold particle (KPL, Maryland, USA) were used as an antigen. 3 diamond samples were implemented in the $top - down$ setup and the impedance was measured at 37°C at pH 7.4. A schematic representation is shown in Figure 5.13 (b). The time resolved impedance, shown in Figure 5.13. From the TRI the black line is the positive sample i.e. the sample incubated with the primary antibody (or image (c) in the sketch). The red line shows the negative control (blocked with BSA (image (b)). A distinct feature is observed in the green line, which represents the bare diamond electrode, in which the noise is much lower and upon protein addition only after 50 minutes a slight increase is observed.

The diamondsamples from the impedance measurement were extracted from the $top - down$ setup and they were 5 seconds gently rinsed with milliQ water to remove any salts. After drying SEM micrographs were made (Figure 5.14). Particle analysis by the image processing software (ImageJ) resulted in average coverage of of ± 5.09 particles/μm^2 for the bare diamond surface (a), 0.78 particles/μm^2 for the BSA blocked surface and 1.09 particles/μm^2 for the primary antibody covered surface.

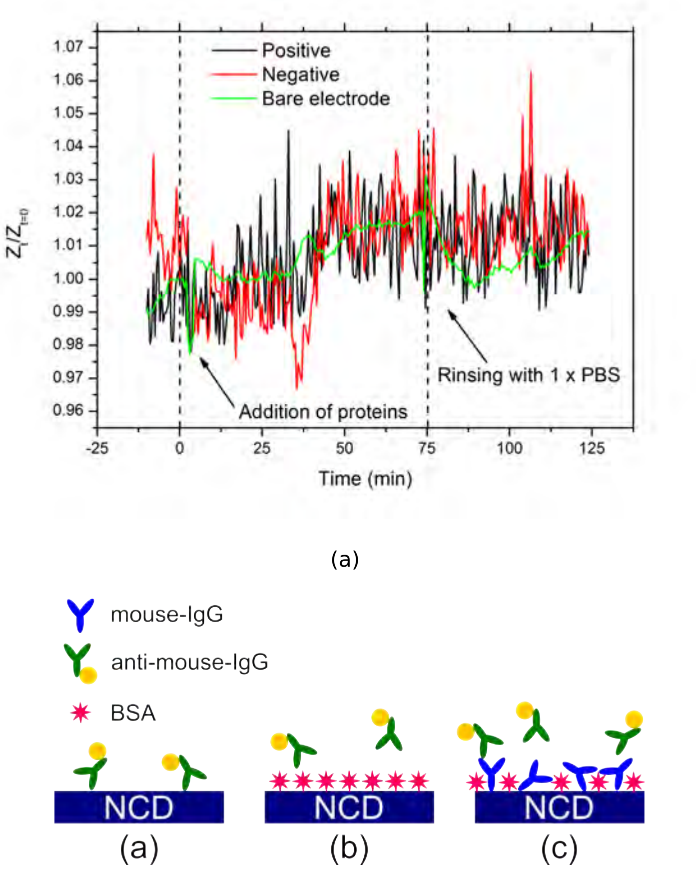

(a)

(b)

Figure 5.13: in (a) a time resolved impedance spectrum is observed at 100 Hz of the recognition and after rinsing. For clarification in (b) a schematic representation is shown of the sensor lay-out.

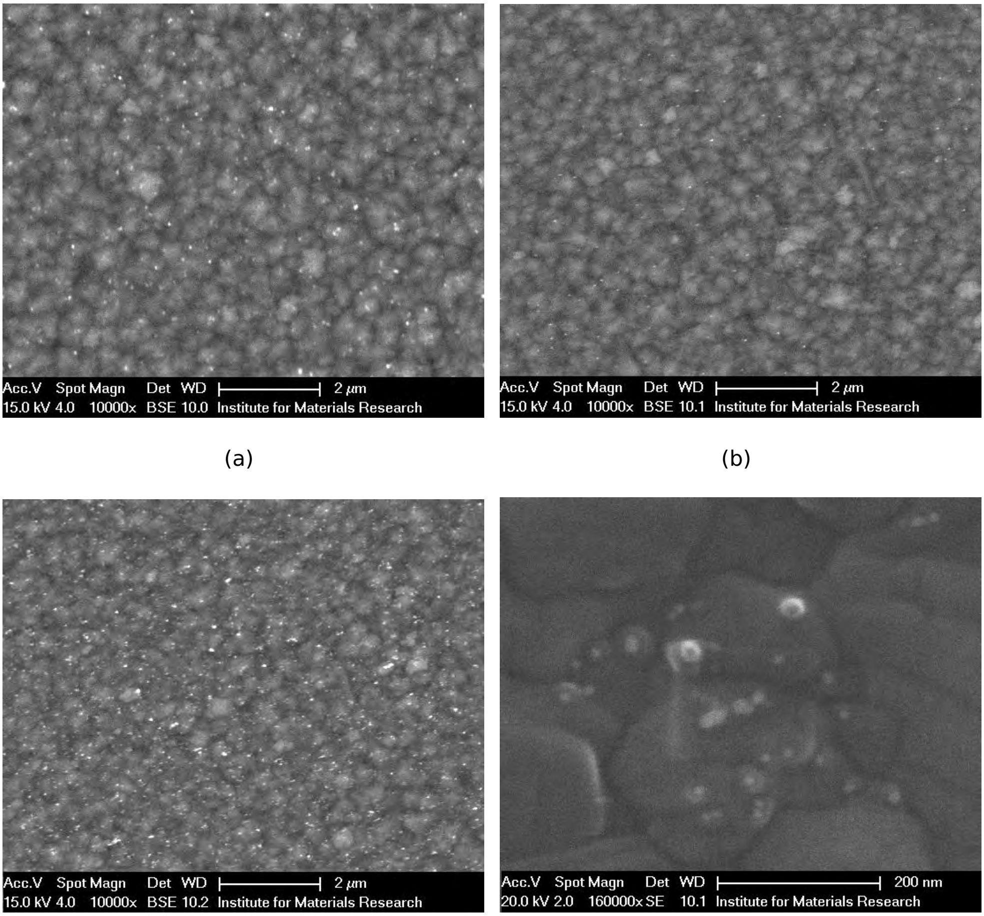

(a) (b)

(c) (d)

Figure 5.14: SEM micrographs of the bare NCD electrode with incubated antibodies (a), BSA covered diamond surface with the antibody incubation (b) and a primary antibody covered diamond surface incubated with the anti-IgG gold particles (c). Close up of the gold antibodies on the diamond surface.

5.3.3 Insulation properties of proteins

In the previous sections we have shown that protein adsorption causes the impedance to increase due to the blocking effect of the electrode. In addition if controlled temperature system is used that is heated from a single side, and the temperature gradient is measured between the working electrode and the liquid electrode a heat transfer constant can be deduced (R_{th}). In the case of DNA hydridization/denaturation a R_{th} change is observed. Here, the adsorption of 20 nM of protein causes an increase in the impedance but no change is R_{th} is measured. Similar effects are observed on μCD.

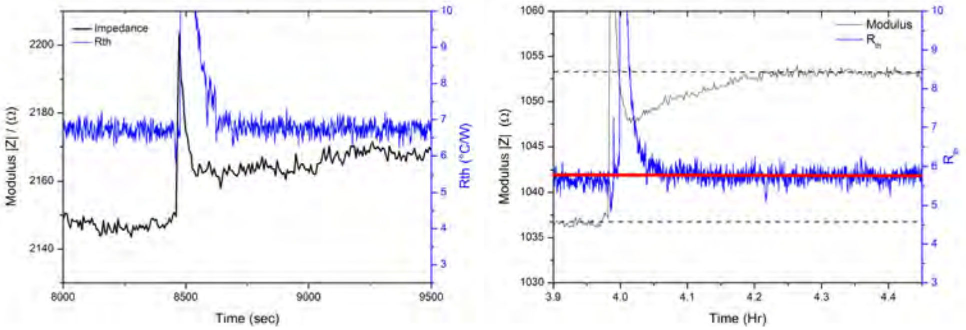

(a) (b)

Figure 5.15: Impedance versus heat transfer resistance (Rth) with in (a) the adsorption of protein on NCD diamond and (b) μCD diamond.

If the adsorbed surface is heated from 20 to 80 °

Protein adsorption First, the antibody adsorption was investigated. A high concentrated solution of 1 μM was used to investigate temperature changes during adsorption on a B:NCD surface. For reference, 1 × PBS with a dummy stock solution without proteins was added to the sensor. This sample represents a concentration of 0 nM. After a stabilized signal was obtained antibodies with a fluorescent label were added. Incubation was during 1 hour at a constant temperature of 37°C. Afterwards the samples were rinsed again with 1 × PBS. Figure **??** shows the impedimetric and thermal response of the protein adsorption. After addition a significant peak in the thermal (bleu) and impedance (black) is observed. Clearly this is caused by thermal effects of the addition process. After addition the

the impedance increases and the thermal gradient remains unchanged. After rinsing the impedance remains at the new level and the temperature gradient between the liquid and copper shows no change. The impedance increase after protein adsorption is described in the previous section.
When the adsorbed proteins are heated up to 70°C there is small anomaly occurs at 45 °C

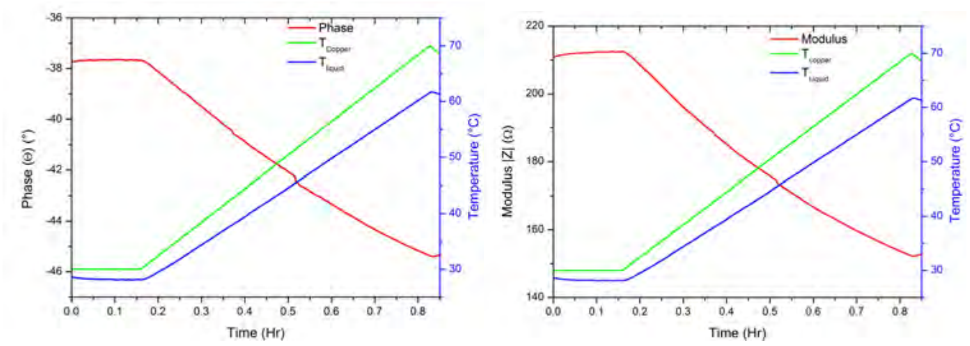

(a) (b)

Figure 5.16: B:NCD with adsorbed proteins. (a) phase in function of time and temperature and (b) show the Modulus at 125 Hz.

Chapter 6

Diamond Architectures

In the first section a brief motivation explains why it is useful to pattern diamond into micro-arrays. Next, the actual development and interfacing with read-out instrumentation is discussed. The patterning technique was based on the typical top-down technique. Also, a novel secondary technique is proposed to create diamond (and other material) structures bottom-up. The final section will encompass some proof-of-principle measurements on whole diamond based electrodes with proteins and DNA.

6.1 Why pattern diamond?

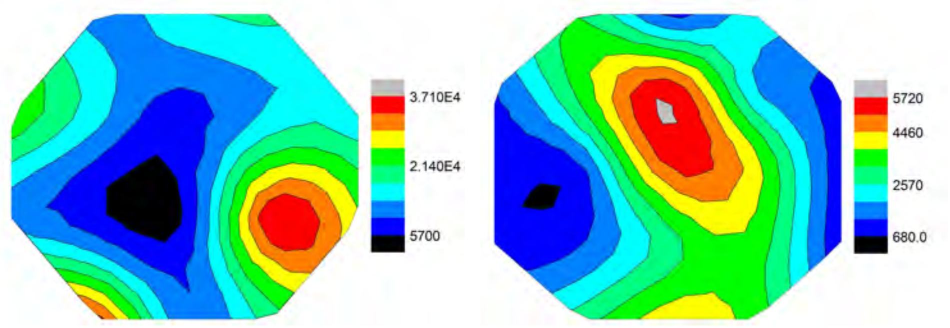

(a)

(b)

Figure 6.1: Here, boron-doped diamond films grown on Si substrates are shown. The color grating indicates resistance variations. In (a) a lower doping concentration was used compared to (b).

By using chemical vapor deposition the uniformity of diamond growth is dependent on the plasma sphere and therefore also on the reactor size. During deposition, different growth rates and dopant incorporation speeds are taking place across the substrate resulting in an inhomogeneous landscape of electronic properties as is shown in Figure 6.1. These plots show a resistance distribution of 2 independent diamond wafers grown on a silicon substrate. It is obvious that these variations in resistance also cause changes in impedance spectra. In Figure 6.2 (a) a photograph of a 2" wafer is shown and in (b) the impedimetric spectra after dicing into 1 cm^2 samples.

As can be seen there is a large inter-sample variation from the same wafer that interdicts comparison of absolute impedimetric data.

Decreasing the sample size and patterning into an electrode array results in more homogeneous electrodes. In Figure 6.2 (c) patterned diamond electrodes are shown and their impedance spectra (d) indicate a larger homogeneity resulting in a much smaller inter-sample variation that is highly beneficial for comparison between electrodes.

6.2 Whole diamond based electrodes

In this section the technical part of diamond patterning is discussed. This includes the technical procedures and interface challenges with read-out techniques. Also, additional considerations are mentioned working with coplanar diamond systems.

6.2.1 Diamond patterning

First, diamond films were grown with the required conditions. In Chapter 3 we demonstrated the different properties of diamond electrodes. Here, typically dopant concentrations between 5000 and 8000 ppm were used with C/H-ratio’s of 0.5 to 1 %. This results in the lowest electrode resistance which is important for good electrode properties. Figure 6.3 shows the different steps employed.

After diamond growth a film of 150 to 400 nm is obtained depending on the substrate (quartz or SiOx). Next an aluminum film of 100 nm was sputtered on top (10 min, 100 sscm Ar, 150 W, 11.7 cm). On this aluminum film a positive photoresist layer (S1818) was spincoated (30 sec, 3000 rpm) and pre-exposure baked at 110°C for 1 minute. The UV exposure was done on a Karl Suss mask aligner (Garching, Germany) with a 350 W Xenon lamp with XXXXX mJ/cm^2 for 8 to 10 seconds. Developing was done 1:4 Microposit developer for 30 seconds. After developing the aluminum was etched in "aluminum etch solution" (RECIPE ETCH SOLUTION) for 5 minutes. The photoresist was removed by an acetone wash (2 minutes).

The remainders are a diamond film with a patterned aluminium cover that serves as a hard mask for oxygen etching. After loading the diamond in the sputtering chamber an oxygen plasma was created (100 sscm O_2, 2 min,

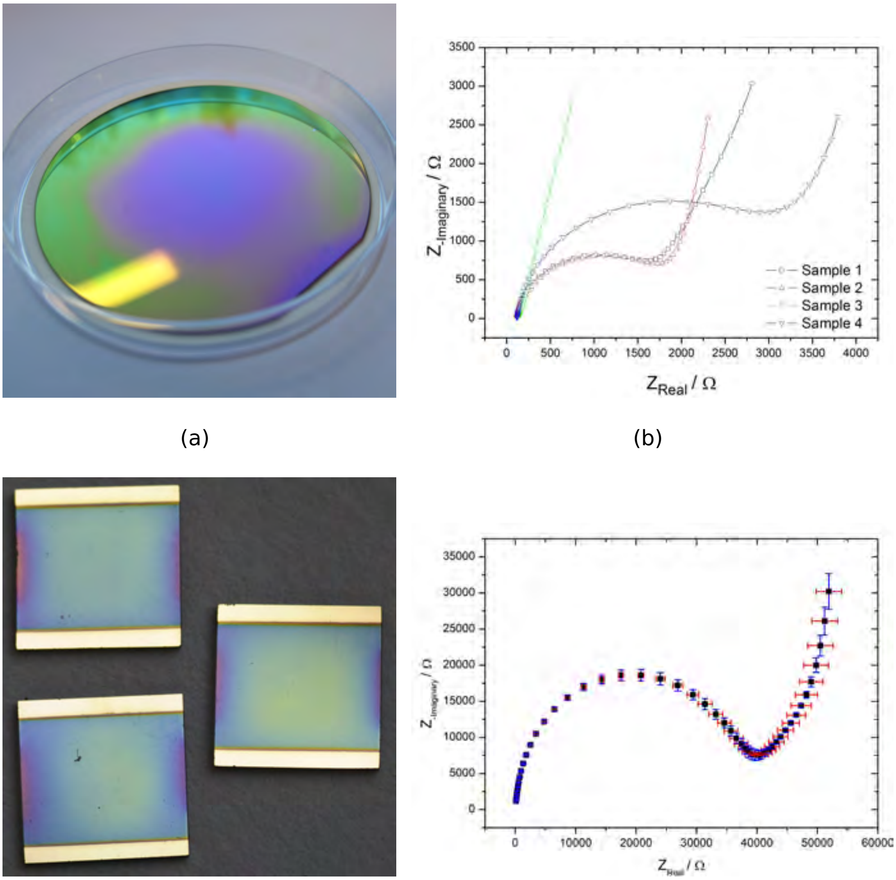

(a)

(b)

(c)

(d)

Figure 6.2: In (a) 4 Nyquist plots of samples from the same wafer are shown in a single measurement. (b) after patterning diamond homogeneous electrode behavior is observed.

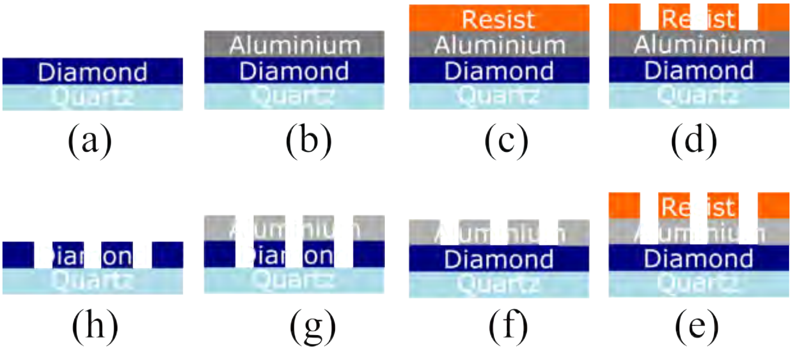

Figure 6.3: Lithographic process for diamond patterning: (a-b) diamond growth, (b-c) aluminium hard mask, (c-d) resist spincoating, (d-e) patterning, (e-f) aluminium etching, (f-g) oxygen plasma diamond etching, (g-h) aluminium removal

11.7 cm, 150 W) to etch the diamond that is not covered by aluminium. In a final step the aluminium was removed by again etching in aluminium etch for 5 minutes. The final result is shown in Figure 6.5. In panel (a) an overview of the 4 electrodes with their concentric counter electrodes are shown. Panel (b) clearly shows the border of the etched diamond electrode.

6.2.2 Interfacing with peripheral equipment

The diamond electrodes now consist of small structures. For contacting the structures were provided with ohmic (Ti/Al) contacts by using a shadow mask for sputtering. These contacts allow two different interfacing methods:

- Packaging and wirebonding for an addition setup
- Contacting via spring-loaded pogo-pins

The packaging consists of gluing the diamond substrate into a pin grid array (PGA). Afterwards, wirebonds were made to provide the electrical connections between the PGA and the substrate. Finally, the PGA was mounted in the socket of a dedicated 4 channel switchcard (Figure 6.5 (a) and (b)).

An O-ring based fluid cell was mounted on these electrodes to form an addition setup similar to those from the immunsensing measurements

(Chapter **??**). A platinum wire fixated in the measurement cell could serve as an optional counter electrode.
A second way of interfacing was via spring loaded pogo pins that served as contacting mechanism (Figure 6.5 (c)). The connections were extended via SMA-coaxials to a bifunctional multiplexer (a single or common gound per channel) which in turn is connected to peripherals. In addition, this setup could be mounted on a peltier element with a temperature range of -10 to 80°C with an accuracy of ±0.05°C. Here the fluid cell was a flow injection mechanism made from polydimethyl siloxane (PDMS) with a volume of 15 μl. The pump was an Ismatec (IPC-N, Wertheim-Mondfeld, Germany) with a pumping range between 200 nl and 3 ml in a open or closed loop system. Typically a flow rate of 100 μl was used.

6.2.3 Electrochemical read-out

First the behavior of oxidized and hydrogenated diamond electrodes is compared to an electrode with the same geometry made from aluminum. Figure 6.6 shows the Bode plots of the four electrodes. The diamond electrodes show a similar spectrum with no additional elements besides the typical R(QR). The only aspect that clearly stands out is the much smaller

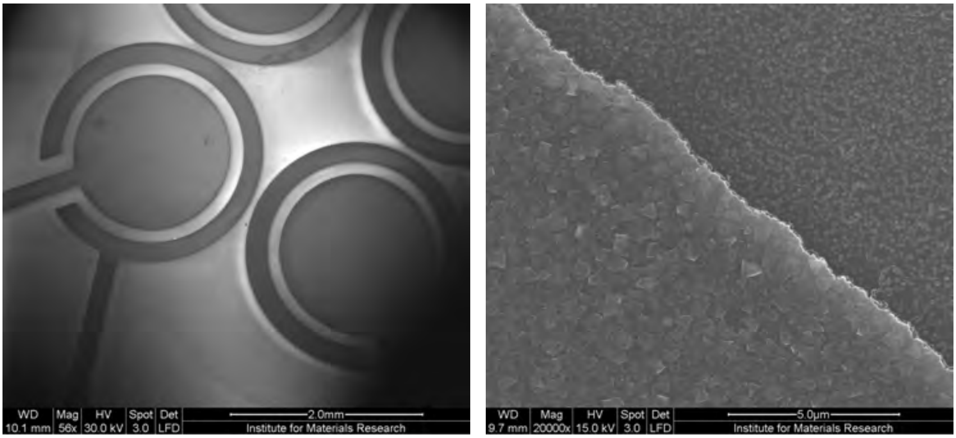

(a) (b)

Figure 6.4: In (a) patterned aluminium on a diamond film, (b) patterned diamond, (c) close up of aluminium patterned electrode after etching, and (d) final patterned diamond electrode after aluminium removal.

series resistance (electrode resistance) of the aluminum electrode.

The large series resistance dominates the spectrum between 100 Hz and 1 MHz so a smaller interface contribution is visible in the lower frequencies. Also there is a large difference between coplanar and top-down sensing. In Figure **??** electrodes were wirebonded and packaged in the addition setup. First a spectrum was taken between 2 symmetrical diamond electrodes and afterwards between a metal electrode in the solution and a diamond electrode. The spectra were fitted with the adapted Randles model R(Q(RW)) (Figure 3.12) and the results are shown in Table 6.1.

From Figure In the case of coplanar electrodes the series resistance nearly doubles cause of the additional diamond electrode involved and the double layer capacitance. The fact that the impedance is measured between 2 diamond electrodes it causes the interface capacitance to decrease (by a

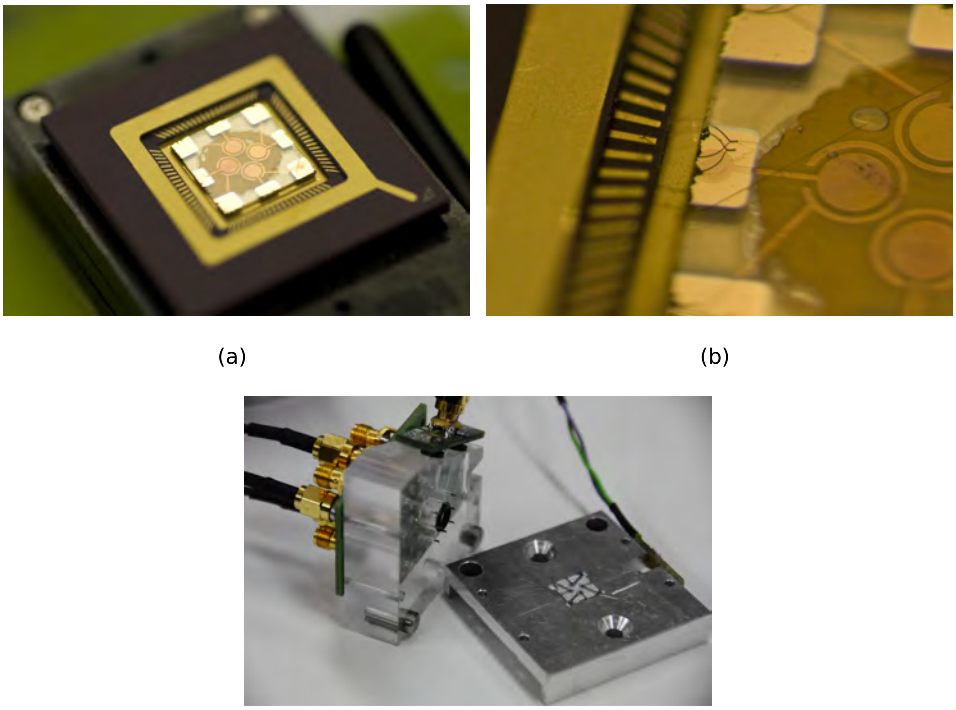
(a) (b)

(c)

Figure 6.5: Complete diamond array packaged in a PGA socket (a) and electrical connections were made by wirebonding and in (c) by spring loaded connections.

Table 6.1: Fitted results of the difference between a top-down and coplanar sensing

Component	Top-down	coplanar	Ratio
R_{series}	2.565e4	4.536e4	1.8
Q_{dl}	6.645e-8	4.078e-8	0.61
n_{dl}	0.92	0.89	0.97
R_{ct}	8.813e6	1.52e6	0.17
W	5.402e-8	4.37e-7	8.1

factor 2). Also the diffusion limited resistance (W) increases in the case of diamond diamond electrodes. Earlier we have shown that this is due to ion adsorption and diffusion near the diamond interface. The use of a coplanar diamond system has a reduced interface capacitance. The stability of the electrodes in electrolyte solution in function of time is impressive. Only a noise level of 0.33 % over 25 hours was observed (results not shown). This greatly improves the measurement conditions.

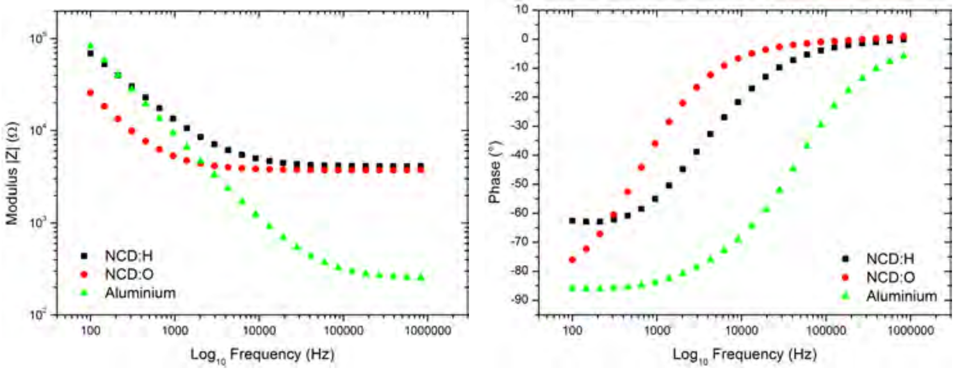

(a) (b)

Figure 6.6: Comparison of Bode plots of electrodes with the same geometry but different characteristics. An Aluminum, NCD:H and NCD:O electrode were measured.

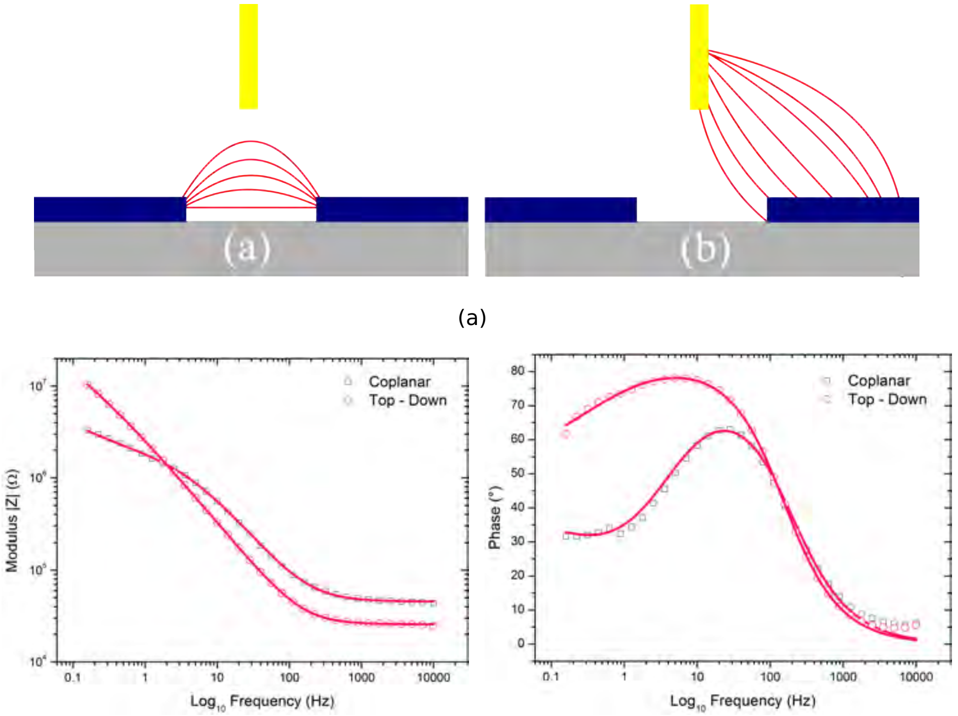

(a)

(b)

(c)

Figure 6.7: Differences between top-down and coplanar sensing. In (a) schematic is shown to illustrate the difference in sensing principle. In (b) the modulus and in (c) the matching phase plots are shown.

6.2.4 Improving electrode lifetime

A great advantage of diamond microarrays is the ability, in contrary to traditional electrodes, to be recycled. The recycling procedure is based on the traditional cleaning in an organic acid mixture with afterwards a hydrogenation step. As mentioned in the introduction, the hydrogen plasma etches sp^2 carbon, this in combination with the aggressive acid, causes the polycrystalline diamond structures to deteriorate and degrade after repetitive cycles. This degradation is visualized in Figure **??**. In panel (a) a CFM recording of an electrode is shown. The yellow edges indicate a different thickness which causes the laser reflection and they also show spots where the diamond is milled. In panel (b) a SEM recording of an etched diamond structure is shown.

To bypass these problems oxidized diamond surfaces were used as a functionlization platform. The functionalization routes have been shown in section **??**. In this case there is no need for hydrogenation and only a short acid wash (1-3 minutes) is employed. Thorough oxidation is done by the mild uv-ozone exposure described earlier. In addition, this is also beneficial when the electrodes are provided with ohmic contacts. The ohmic contacts are destroyed by the hydrogen plasma. The only metal that could withstand is Tungsten (W) but it forms tungsten carbide upon heating so wirebonding is no longer possible.

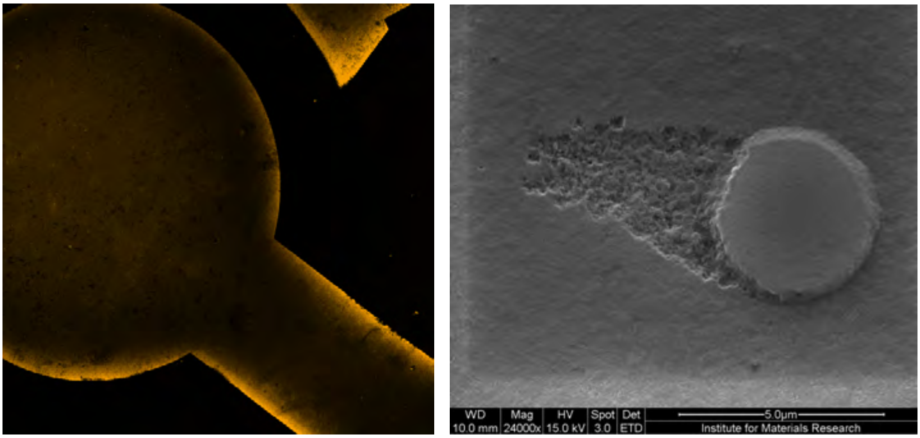

(a) (b)

Figure 6.8: Examples of diamond electrode degradation. (a) shows the reflection during a CFM measurement and in (b) a SEM recording of an etched area.

6.2.5 Biofunctionalization of whole diamond electrodes

An additional challenge to work with these micro structures is the selective biofunctionalization of each electrode. The traditional setup requires large volumes (50-100 μl) but now with the reduced surface area of 1 mm^2 volumes of 1μl are in order.

Therefore PDMS reactors have been made which allow specific functionalization. We preferred triangular structures that were milled from PTFE which were moulded afterwards with PDMS. The micro-reaction chambers act as flow injections that constrain the biomolecule liquid for specific

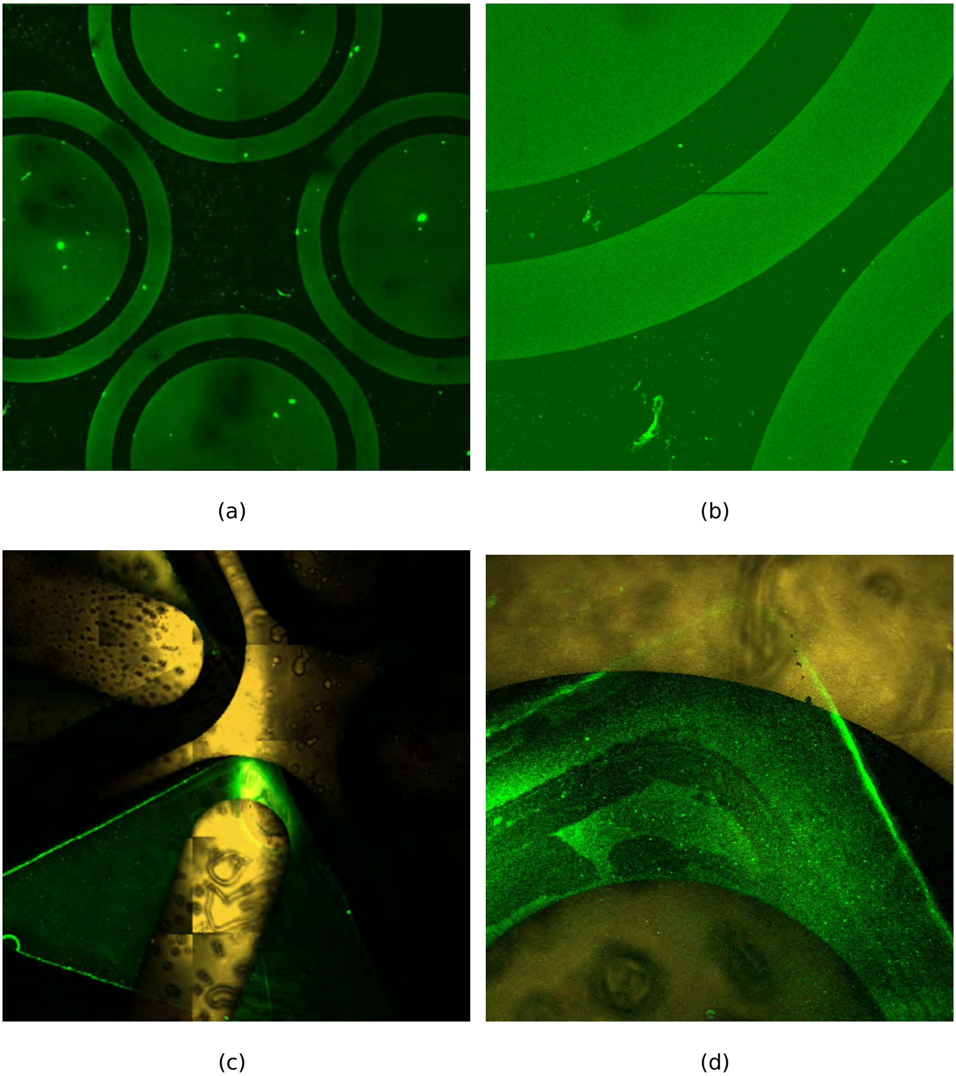

Figure 6.9: Functionalization of diamond electrodes. In panel (a) and (b) the adsorption of fluorescent labeled antibodies. (c) and (d) show the diamond electrode (yellow) with selective functionalization of antibodies (green) by a PDMS chamber.

functionalization. These experiments gave rise to the following section in which the PDMS micro-reactor principle is further employed.

6.2.6 Conclusion

In this section we have shown the construction of whole diamond based electrodes. The great advantage of these electrodes is the possibility for miniaturization. In addition the diamond provides also a large durability with lots of potential for surface functionalizations. The synthesis of these electrodes requires a good understanding of the electrical and electrochemical properties of these diamond films. The properties studied in Chapter 3 are of utmost importance for the application in these electrodes.

6.3 A novel and innovating bottom-up approach for diamond electrodes

In this section we discuss the possibilites of using PDMS micro-stamps as reactors for bottom-up construction of

6.3.1 Mold synthesis

Fused silica and SiOx substrates were cleaned in two steps, first a solvent cleaning and finally immersion in piranha solution for 20 minutes. Afterwards they were dried under a N_2 flow and placed in a uv-ozone cleaner for 30 minutes. SU-8 2075 photoresist (Microchem, Newton, US) is diluted with its developer to obtain a 80% concentration. Next, the substrates were spincoated (300 rpm for 8 seconds, 8000 rpm for 40 seconds). A 65°C curing was done for 1 minute, and afterwards a pre-exposure bake at 95°C for 10 minutes. eBeam lithography was performed with an exposure of XXXXXC. Post exposure baking was done at 95° and 2 minutes developed in pure SU-8 developer (Microchem, Newton, US). Afterwards a final curing of 150° was performed. These epoxy structures form a predefined mold on which a silicone elastomer PDMS was casted. Afterwards the PDMS was peeled off and transferred to another substrate to create the 'negative' of the 3D SU-8 structure.

To illustrate this concept we designed a proof-of-principle which is shown in Figure 6.10. In panel (a) a SEM recording is shown of the SU-8 structure created by e-beam lithography. Because e-beam is CAD programmable there are more degrees of freedom compared to conventional lithography. The epoxy mold that serves as a template is covered with the PDMS.

PDMS settles around the form and after it is hardened the PDMS is peeled off and transferred to another substrate. Here, quartz is used to have a transparent substrate. The mold is connected to a flow system through which fluorescent labelled antibodies are flushed as a tracer. The image shown in panel (b) was recored in the initial phase. The width of the PDMS channels were around 25 μm for highly reproducible results. In the following subsection the PDMS chambers are employed for device construction.

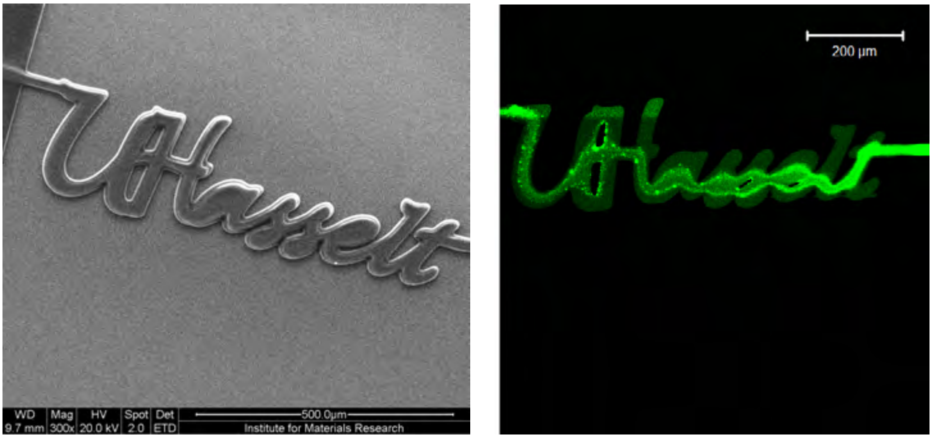

(a)

(b)

Figure 6.10: (a) SEM recording on an SU-8 mold (b) the filling of the negative image made from PDMS. As tracer we added fluorescent labeled biomolecules.

6.3.2 Selective seeding

The construct discussed in the previous section is here employed to cover specific area's with a seeding solution of nano-diamonds. Diamond seeding occurs instantaneously so after a short flush and drying at 65°C for 30 minutes the PDMS is peeled off and diamond was grown. For these delicate surfaces a two step growth process was employed. First the power was set to 3500 W at 28 Torr during 10 minutes, next the power was ramped up to 4000 W at a pressure of 45 Torr for 30 minutes. The gas mixture was made of hydrogen (H_2,CH_4, and Trimethyl borane with 410, 15 and 75 sscm respectively.

The results are shown in Figure 6.13. The structures show a well defined geometry with a clear and high resolution edge. The highest reproducibility is obtained with structures of 20 μm width. However, smaller structures are also possible! An example of diamond lanes with a few micron width to even a 600 nm bottle neck diamond structures have been made and are shown in panel (c) and (d). The film quality between (a), (b) and (c), (d) is also different, this could be improved by prolonged growth time. Besides diamond structures a broad variety of this bottom-up approach is

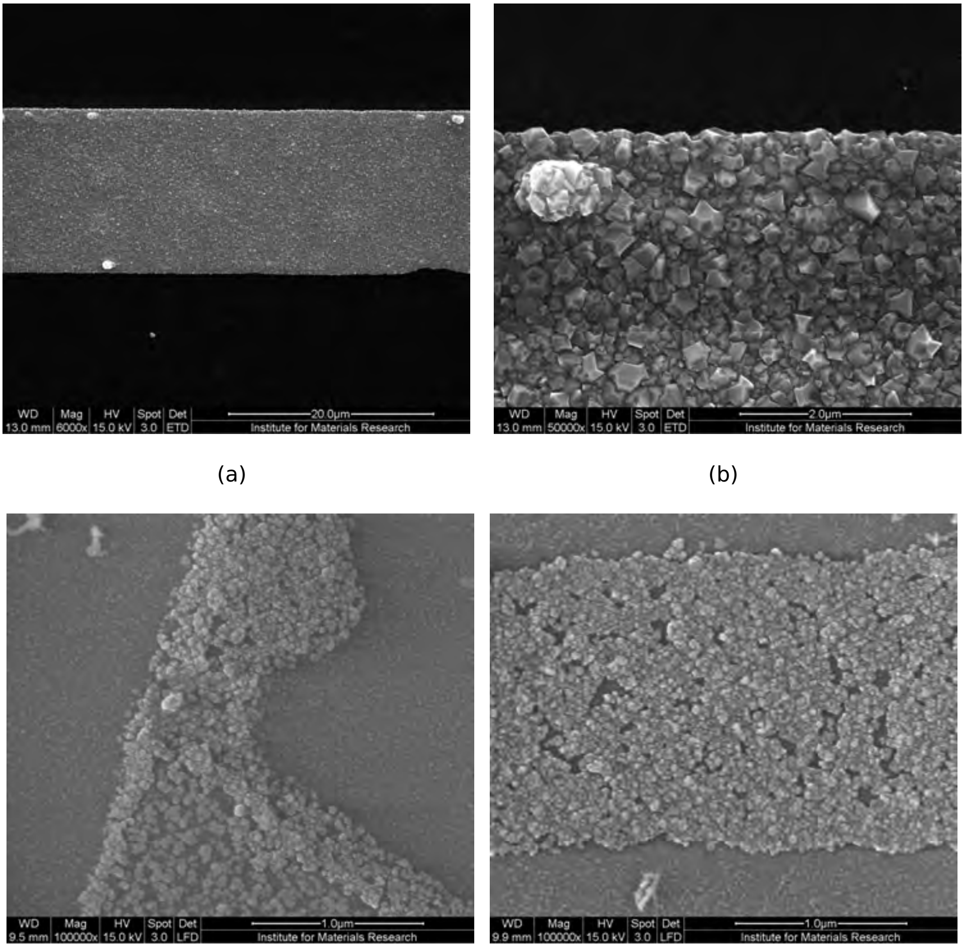

(a) (b)

(c) (d)

Figure 6.11: (a) Small selective seeded diamond structure. (b) the master mask out of SU-8 photoresist.

possible. There could be applications in the ZnO research in which ZnO precursor is patterned along a surface and nanorods are grown from this. Another is the micro-biofunctionalization of surfaces for protein adsorption or covalent coupling of DNA in micro-reactors.

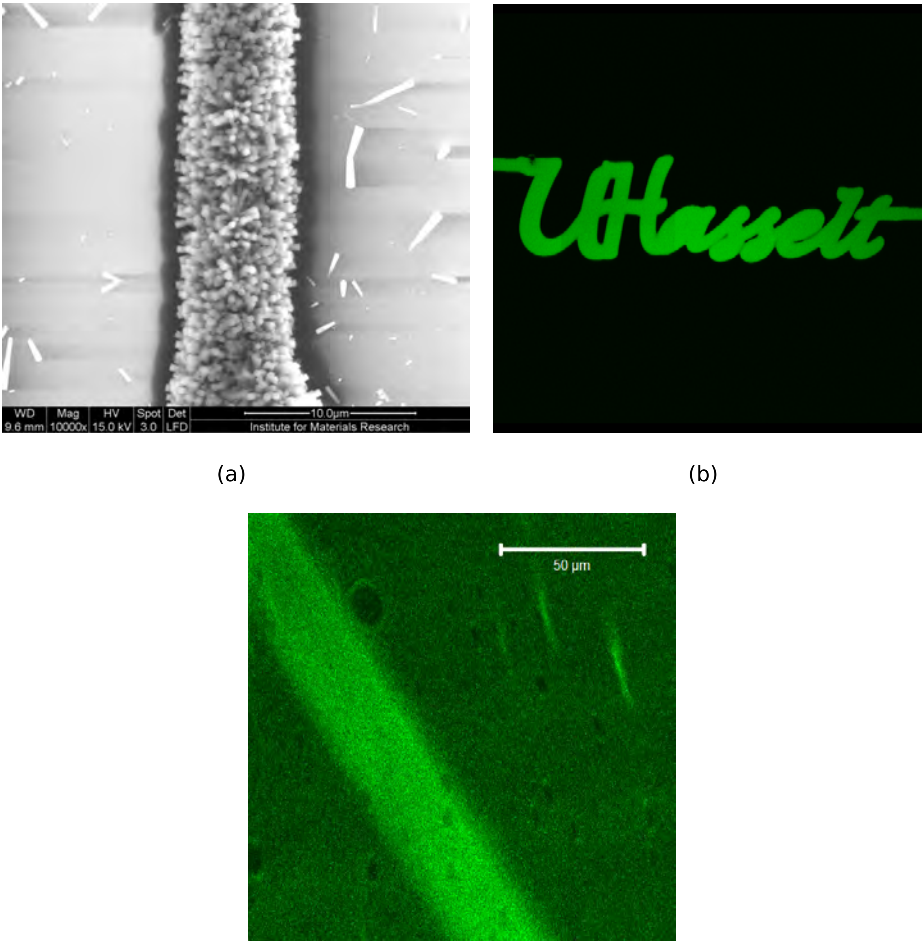

(a)

(b)

(c)

Figure 6.12: (a) Small selective seeded diamond structure. (b) the master mask out of SU-8 photoresist.

6.4 Coplanar diamond electrode arrays and integration

In this section the structures described in section 6.2 are employed for proof-of-principle biosensing.

6.4.1 Protein adsorption

For protein adsorption hydrogenated and oxdized electrodes were packaged in a flow injection system. The stabilization of the measurement is done in 1 × PBS with the temperature control at 37°C. After a stable signal 20 nM antibodies were added and the TRI is monitored at 100 Hz. Upon addition the typical upward trend is observed. However the signal intensity now only increased less than 1 % due to the smaller sensitive area. The Nyquist plot only shows a variation in the lowest frequency. The first semicircle remains unchanged whilst the doublelayer, similar as before, changes. The interface capacitance (Q_{dl}) was 217 nF and after adsorption it decreased to 199 nF. Also the R_{dl} increased from 7915 to 7983 Ω.

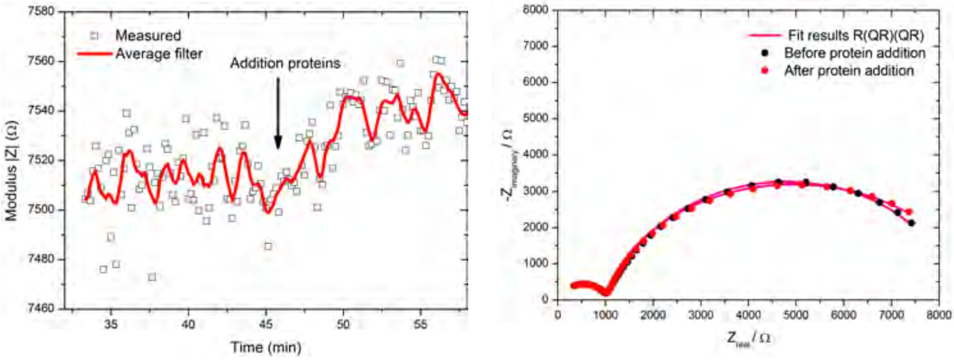

(a) (b)

Figure 6.13: (a) TRI and (b) modeled Nyquist results with the R(QR)(QR) model of protein adsorption on coplanar diamond electrodes.

6.4.2 DNA denaturation

For this oxidized diamond was functionalized via the succenic anhydride pathway described earlier (REF SECTION XXXXXXXX). 10 pmol/μl DNA is coupled to the surface via the EDC coupling. After washing in 1 × PBS and in 2 ×SSC /0.5% SDS (30 min, KT) the sample were hybridized by a full match complementary strand. A 100 pmol/μl solution is added diluted with hybridization solution which is incubated for 2 hours at 60°C. Afterwards a stringency washingstep in 2 × ssc/0.5% SDS (30 min, KT) resulted in completely fullmatch surface. The complementary strand was coupled with a fluorescent label resulting in a fluorescent signal in case of full hybridization.
INSERT FIGURE

The measurement conditions were kept constant in 1 × PBS at 37°C and after a stable impedance signal was obtained 0.1 M NaOH was added in a flow rate of 100 μl/min for 2 minutes. The impedance regresses and the cell was reflushed after some time with PBS. The denatured DNA is now again exposed to 0.1 × NaOH as a reference and forms a second decay. Figure6.14 shows two independent normalized TRI measurements at 1150 Hz. In panel (a) the difference before and after NaOH rinsing is indicated in these graphs.
FIG. **??** shows the impedance profile of the denaturation of full-match DNA on the B:NCD sample. At t = 0, 0.1 M NaOH enters the cell and replaces the 1×PBS buffer, causing a drop of the fluorescence intensity and the impedance. This emerges from the denaturation and the change of liquids, while the fluorescence drop stems from DNA denaturation only. The extraction of the time constants τ_1 (denaturation) and τ_2 (exchange of fluids) is based on the Fits 1 and 2, as described in:

$$Z(t) = Z(t=\infty) + A_1 exp\left(-\frac{t}{\tau_1}\right) + A_2 exp\left(-\frac{t}{\tau_2}\right) \tag{6.1}$$

$$Z(t) = Z(t=\infty) + A_2 exp\left(-\frac{t}{\tau_2}\right) \tag{6.2}$$

are double-exponential fit according to EQ. 6.1 for superimposed, independent decay processes is known e.g., from the decomposition of biomass (tomato leaves) and the mass loss of tomato DNA as a function of time [**?**]. The parameter A_1 represents the denaturation-related decay amplitude and τ_1 the associated time constant; the amplitude A_2 refers to the impedance drop by the medium exchange and τ_2 is the corresponding time constant. The fit according to EQ. 6.2 describes solely the influence of the medium exchange from 1×PBS to 0.1M NaOH after the denaturation has taken place and is therefore representative for the medium exchange as such. The first time constant, derived from the impedimetric data (τ_1) is 2.24 ± 0.14 min from. To determine $\tau_2 = 0.97 \pm 0.06$ min, the cell was refilled with 1×PBS buffer at $t_1 = 12$ min and flushed with 0.1 M NaOH at $t_2 = 30$ min. The amplitudes A_1 and A_2 indicate the respective influence of denaturation and liquids exchange on the impedance changes.

6.4.3 Results

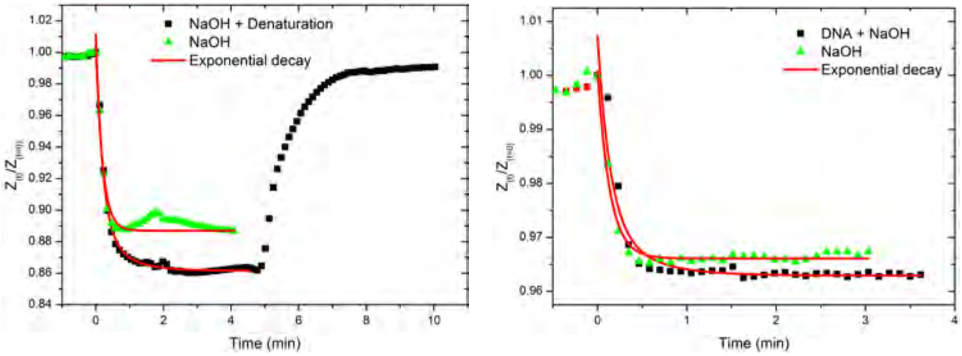

(a) (b)

Figure 6.14

Table 6.2: Summary of τ_1 and τ_2 values for different types of target DNA.

target DNA	τ_1 (minutes)	τ_2 (minutes)
Complementary	0.19 ± 0.1	0.70 ± 0.1

FIG. **??** gives an overview of the denaturation steps performed on B:NCD with complementary target DNA(a), mismatch at base pair 20 (b), mismatch at base pair 7(c), and the random target sequence (d). All data described as *chemical denaturation* are normalized to the impedance value at the moment when 0.1 M NaOH enters the cell and fitted with the double exponential EQ. 6.1 (Fit 1) as described before. The curves denoted

as *medium exchange* refer to the second replacement of 1×PBS by 0.1 M NaOH after the actual denaturation step. These data are normalized with respect to the equilibrium impedance value at the time t_2 obtained after refilling the cell with 1×PBS buffer (Fit 2 according to EQ. 6.2). TAB. 6.2 summarizes the obtained values. It is clear that the thermodynamically most stable system is the hybridized DNA system with the complementary DNA strand. All other systems have τ_1 values which are significantly much lower. The τ_2 values are all the same which reflects the repeatability of the measurement.
Protein adsorption, LEUVEN, DNA hybridisatie denaturatie

6.4.4 Conclusion

Further characterization is done by confocal fluorescence microscopy. When using a fluorescent dye it is possible to perform tommography like recordings that contain 3D information about the channel.

Chapter 7

Gravimetric protein detection on diamond-like surfaces

In this chapter efforts were made to construct a gravimetric protein sensor. Up till now no commercial QCM sensors are coated with diamond. The reason for this absence are the requirements of piezoelectric properties of the quartz crystal to actuate the sensing principle. These properties start to degrade when the quartz crystal is heated above 300°C. Diamond growth however can start from 500°C resulting in loss of the piezoelectric properties. Therefore, we tried to develop a novel concept system of a gravimetric immunosensing platform based on based on a diamond-like surface by using nano-diamonds as anchorpoints for protein immobilization.

7.1 Theory and background

When a thin quartz slice is cut in an angle of 35°10’ (AT-cut) ith respect to the optical axis of an α-quartz crystal it gains piezo-electric properties. The application of a voltage to an AT-cut crystal causes thickness shear movement by mechanical induced shear-strain forces in the crystal. An alternating voltage will in turn create an oscillatory movement (shaking) of the crystal. The resonance frequency of the crystal is dependent of the mass load on top of the crystal. With an increasing mass the resonance frequency of the sensor decreases which makes the quartz crystal microbalance a gravimetric read-out technique with mass sensitivities down to nanogram/cm^2. The relation between the frequency shift (Δf) and the mass was explained by the Sauerbrey equation (Eq. 7.1). Figure 7.1 (a) shows the drop in frequency after a mass adsorbs at the surface.

$$\Delta f = -\frac{2f_0^2}{A\sqrt{\rho_q \mu_q}} \tag{7.1}$$

With f_0 the resonance frequency of the crystal (Hz), Δf the frequency change (Hz), Δm the mass change (g), A the piezo-electric active area (m^2), ρ_q the quartz density and μ_q the shear modulus of quartz AT-cut crystal. The previous equation can be reduced to the following:

$$\Delta m = -\frac{C \cdot \Delta f}{n} \tag{7.2}$$

With C the mass per frequency per area sensitivity for a 5 MHz crystal (17.7 ng Hz^{-1} cm^{-2}) and n (1,3,5,7) the overtone number.

In most situations the adsorbed film is not rigid and the previous relations becomes invalid. A film that is ’soft’ (viscoelastic) will not fully couple to

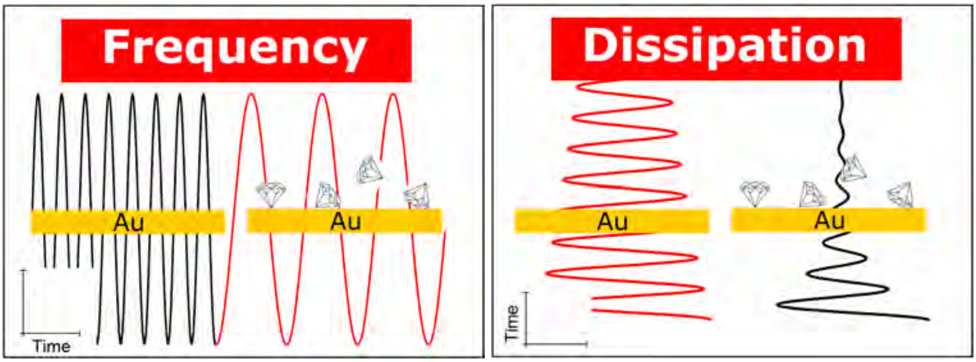

(a) (b)

Figure 7.1: Schematic representation of the QCM-D principles. In panel (a) the drop in frequency is shown upon gaining a mass load on the surface and in (b) the shift in dissipation due to creating a different coupling behavior to the liquid when a new layer is formed.

the oscillation of the crystal, so the Sauerbrey relation will underestimate the mass at the surface. A soft film will dampen the sensor's oscillation. The damping or energy dissipation (D) of the sensor's oscillation reveals the film's softness. The dissipation is defined as:

$$D = \frac{E_{dissipated}}{2\pi E_{stored}} \tag{7.3}$$

Where $E_{dissipated}$ is the energy lost during one oscillation cycle and E_{stored} is the total energy stored in the oscillator. The dissipation is measured by switching of the driving power and voltage of the sensor crystal decays exponentially as a damped sinusoidal. The change in dissipation due to different coupling to the surrounding fluid is shown in Figure 7.1 (b).

7.2 Experimental

The quartz crystal microbalance was purchased from Q-sense (Gotenborg, Sweden) with 4 flow cell modules (Figure 7.2). The gold plated quartz crystals had a typical thickness of 0.3 mm with a diameter of 14 mm. The volume above the sensor was 40 μl with a total volume from inlet to outlet of about 150 μl. A 4 channel ismatec IPC-N pump was used with a constant flow of 50μl/min.

Prior to use QCM crystals were cleaned in a 5:1:1 mixture of NH_3 + H_2O + H_2O_2 at 70°C for 10 minutes. Next they were thoroughly rinsed with

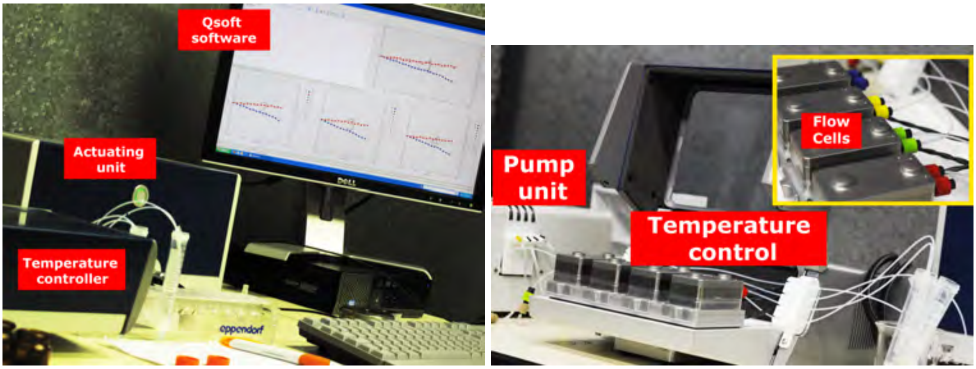

(a) (b)

Figure 7.2: Photographs of the Q-sense quartz crystal microbalance used in this chapter. The actual flow cells are shown in the inset of panel (b).

MilliQ water and dried under nitrogen. Afterwards a final cleaning was done for 15 minutes in uv-ozone. The nano-diamond enhancement of the surface was done by physisorption of a 0.05 g/ml UDD nanodiamond solution (Osawa, Japan). Buffer solutions were 1 × PBS at pH 7.4. All of the measurements were at 30 °C. The following protein solutions were used. The primary antibody (anti-CRP) and the antigen (CRP) were from Scipac (Kent, UK). A secondary anti-IgG antibody was used from Invitrogen (Gent, Belgium) as a control protein and BSA was purchased from Sigma-Aldrich (Merelbeke, Belgium).

7.3 Results

In the following subsections a step wise explanation starting from the surface enhancement with nano-particles to the immunosensing concept.

7.3.1 Surface enhancement

In Figure 7.3 The resonant frequency, $\Delta f(t)$ and the dissipation factor $\Delta D(t)$m are shown. The initial phase is started with a bare gold crystal in MilliQ water with the addition of 0.05 g/ml UDD diamond to the black channel and MilliQ to the red channel. Immediately after addition a fast initial frequency decrease (mass increase) followed by a slower decrease as the surface coverage saturates. As seen in Figure 7.3 (b) the D-shifts are positive, and display a kinetic similar behavior similar to the f-shifts. After rinsing no changes were observed indicating an irreversible adsorption at the surface.

7.3.2 Surface bio-functionalization

After seeding the surface 4 different measurements were conducted.

- 4 seeded surfaces from which 2 were incubated with receptor proteins and 2 blocked with BSA

- 2 seeded surfaces and 2 unseeded surfaces, all functionlized with receptor proteins.

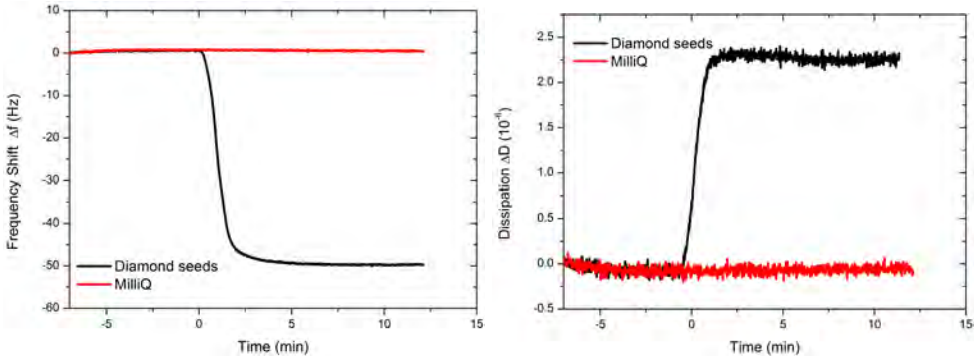

(a) (b)

Figure 7.3: Changes in frequency (a) and dissipation (b) as function of time during adsorption of nanodiamonds on the untreated gold surface. The seeds were introduced at (t=0) in a concentration of 0.05 g/ml in MilliQ.

To keep in mind that the surface area on these nano-particles is much higher, a larger antibody immobilization concentration was used compared to the diamond film substrates. Here, 1/500 dilutions were used. After immobilizaton of these proteins the surface was blocked with 6w% BSA to block all remaining binding sites.

In Figure 7.8 the gravimetric response can be seen from the protein adsorption on gold and the seeded surfaces. In panel (a) all of the surfaces were seeded but only 1 received the proteins whilst the other PBS. A significant result is obtained indicating proteins adsorbed at the surface. In panel (b) two substrates were seeded and 2 were bare gold. The proteins adsorbed only on the seeded surface proving that it its of utmost importance that anchorpoints are necessary. Also this is inrefutable proof that the nano-diamond enhanced surface is a suitable sensor substrate.

7.3.3 Immunosensing concept

7.4 Conclusion

Interesting outlooks and possibilities of these platforms are the testing of new immobilization metals that are commercially available. Also other

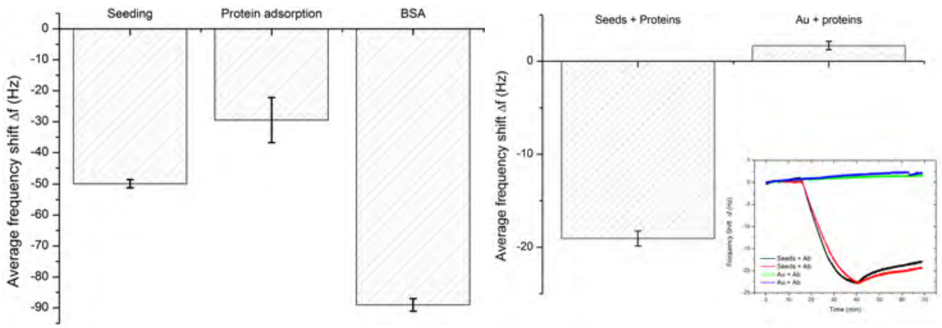

(a) (b)

Figure 7.4

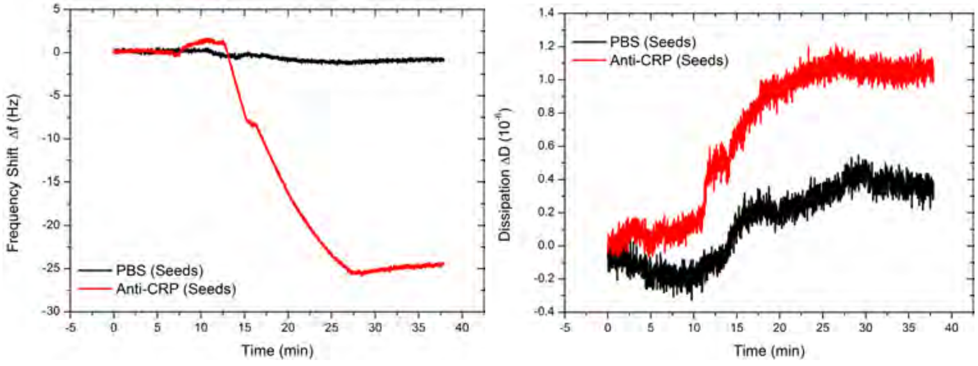

(a) (b)

Figure 7.5

functionalized diamond seeds could be tried. The use of short hydrogen plasmas to immobilize the seeds could allow regeneratable surfaces However these aspects were not studied in this research because it was the last experiment planned and the optimalization is not possible within the timeframe of this thesis.

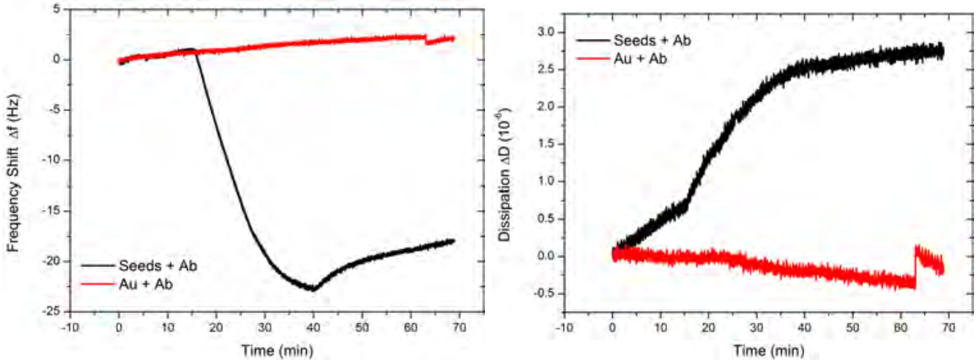

(a) (b)

Figure 7.6

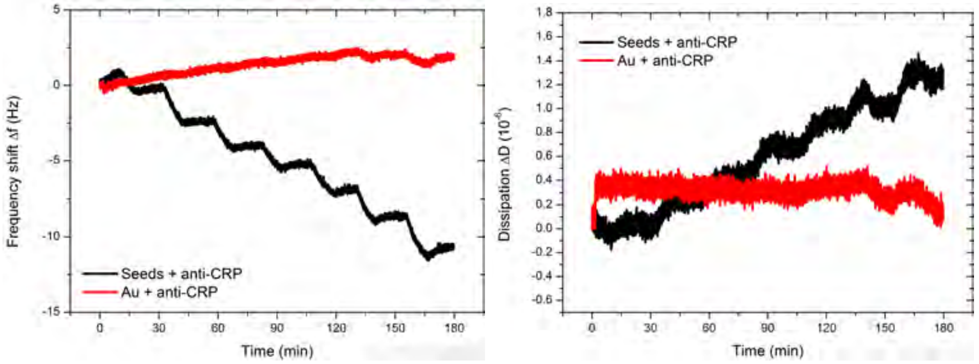

(a) (b)

Figure 7.7

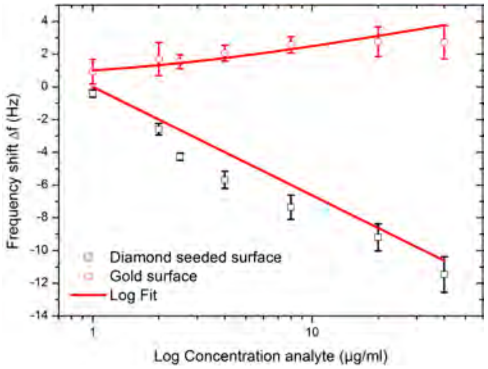

Figure 7.8

Bibliography

[1] L. J. Clark, Trans. Am. Soc. Artif. Intern. Organs. **2** (1956).

[2] L. Tiefenauer and C. Padeste, Chimia **53**(3) (1999).

[3] D. Leech and K. O. Feerick, ELECTROANALYSIS **12**(16), 1339–1342 (2000).

[4] D. R. ThÃ©venot, K. Toth, R. A. Durst, and G. S. Wilson, Biosensors and Bioelectronics **16**(1-2), 121–131 (2001).

[5] K. R. Rogers, J. Y. Becker, and J. Cembrano, Electrochemica Acta **45**(25-26), 4373–4379 (2000).

[6] D. Thompson, M. B. Pepys, and S. P. Wood, Structure (London, England : 1993) **7**(2) (1999).

[7] M. B. Pepys and G. M. Hirschfield, The Journal of Clinical Investigation **111**(12), 1805–1812 (2003), 10.1172/JCI18921.

[8] http://c reactive protein crp.blogspot.com/.

[9] D. C. W. Lau, B. Dhillon, H. Yan, P. E. Szmitko, and S. Verma, American Journal of Physiology - Heart and Circulatory Physiology **288**(5), 2031–2041 (2005).

[10] F. C. de Beer, C. R. Hind, K. M. Fox, R. M. Allan, A. Maseri, and M. B. Pepys, British heart journal **47**(3) (1982).

[11] f. t. M. R. Group, L. H. Kuller, R. P. Tracy, J. Shaten, and E. N. Meilahn, American Journal of Epidemiology **144**(6) (1996).

[12] P. M. Ridker, C. H. Hennekens, J. E. Buring, and N. Rifai, New England Journal of Medicine **342**(12) (2000).

[13] P. M. Ridker, M. Cushman, M. J. Stampfer, R. P. Tracy, and C. H. Hennekens, New England Journal of Medicine **336**(14) (1997).

[14] D. M. Lloyd-Jones, K. Liu, L. Tian, and P. Greenland, Annals of Internal Medicine **145**(1) (2006).

[15] I. Roitt, J. Brostoff, and D. Male, Immunology, 6 edition (Mosby, New York, 2001).

[16] J. Berg, J. Tymoczko, and L. Stryer, Biochemistry, 5 edition (Freeman and company, New York, 2002).

[17] R. Nairn and M. Helbert, Immunology for medical students (Mosby, New York, 2002).

[18] R. Glockshuber, M. Malia, I. Pfitzinger, and A. Pluckthun, Biochemistry **29**(6), 1362–1367 (1990).

[19] http://visualscience.ru/en/illustrations/visualization/IgG/.

[20] http://upload.wikimedia.org/wikipedia/commons/f/f8/Eight Allotropes of Carbon.png.

[21] http://upload.wikimedia.org/wikipedia/commons/f/f1/Silicon unit cell 3D-balls.png.

[22] A. K. Geim and K. S. Novoselov, Nat Mater **6**(3), 183–191 (2007), 10.1038/nmat1849.

[23] C. Kittel, Introduction to Solid State Physics (John Wiley & Sons, New York, 1996).

[24] http://ibandc.be.

[25] M. A. Prelas, G. Popovici, and L. K. Bigelow, Handbook of Industrial Diamonds and Diamond Films (Marcel Dekker, New York, 1998).

[26] P. Ascarelli and S. Fontana, Appl. Surf. Sci. **64**, 307 (1993).

[27] S. Iijima, Y. Aikawa, and K. Baba, Appl. Phys. Lett. **57**, 2646 (1990).

[28] S. Yugo, T. Kimura, and T. Muto, Vacuum **41**, 1364 (1990).

[29] J. Robertson, Diamond Relat. Mater. **4**, 549 (1995).

[30] O. A. Williams, O. Douheret, M. Daenen, K. Haenen, E. Osawa, and M. Takahashi, Chemical Physics Letters **445**(4-6), 255–258 (2007).

[31] S. D. Janssens, Morphological and electronic properties of strongly boron-doped diamond films prepared by chemical vapor deposition, PhD thesis, 2011.

[32] P.K. Bachmann and U. Linz, Advanced Materials **3**(1), 64–66 (1991).

[33] J. A. Garrido, Biofunctionalization of Diamond Surfaces: Fundamentals and Applications, (John Wiley & Sons, 2009).

[34] H. B. Martin, A. Argoitia, J. C. Angus, and U. Landau, Journal of The Electrochemical Society **146**(8) (1999).

[35] M. Nesladek, D. Tromson, C. Mer, P. Bergonzo, P. Hubik, and J. J. Mares, Applied Physics Letters **88**(23) (2006).

[36] Y. Show, M. A. Witek, P. Sonthalia, and G. M. Swain, Chemistry of Materials **15**(4) (2003).

[37] G. Swain, Advanced Materials **6**(5) (1994).

[38] J. A. Bennett, J. Wang, Y. Show, and G. M. Swain, Journal of The Electrochemical Society **151**(9) (2004).

[39] A. E. Fischer, Y. Show, and G. M. Swain, Analytical Chemistry **76**(9) (2004).

[40] D. M. Gruen, Annual Review of Materials Science **29**(1) (1999).

[41] H. Young and R. Freedman, Univeristy Physics with modern physics, 10 edition (Addison-Wesly publishing company, New York, 2000).

[42] V. Vermeeren, N. Bijnens, S. Wenmackers, M. Daenen, K. Haenen, O. A. Williams, M. Ameloot, M. vandeVen, P. Wagner, and L. Michiels, Langmuir **23**(26) (2007).

[43] A. HÃ¤rtl, E. Schmich, J. A. Garrido, J. Hernando, S. C. R. Catharino, S. Walter, P. Feulner, A. Kromka, D. Steinmuller, and M. Stutzmann, Nat Mater **3**(10), 736–742 (2004).

[44] F. Maier, M. Riedel, B. Mantel, J. Ristein, and L. Ley, Physical Review Letters **87**(20), 209706 (2001).

[45] F. Maier, J. Ristein, and L. Ley, PHYSICAL REVIEW B **64**(16) (2001).

[46] S. J. Sque, R. Jones, and P. R. Briddon, Physical review B **73**(8), 085313 (2006).

[47] V. Chakrapani, S. C. Eaton, A. B. Anderson, M. Tabib-Azar, and J. C. Angus, Electrochemical and Solid-State Letters **8**(1), E4–E8 (2005).

[48] J. A. Garrido, S. Nowy, A. HÃ¤rtl, and M. Stutzmann, Langmuir **24**(8) (2008).

[49] Q. Cao, H. Zhao, Y. Yang, Y. He, N. Ding, J. Wang, Z. Wu, K. Xiang, and G. Wang, Biosensors and Bioelectronics **26**(8), 3469–3474 (2011).

[50] G. Liu, J. Liu, T. P. Davis, and J. J. Gooding, Biosensors and Bioelectronics **26**(8), 3660–3665 (2011).

[51] W. Liang, W. Yi, S. Li, R. Yuan, A. Chen, S. Chen, G. Xiang, and C. Hu, Clinical Biochemistry **42**(15), 1524–1530 (2009).

[52] M. d. S. Castilho, T. Laube, H. Yamanaka, S. Alegret, and M. I. Pividori, Analytical Chemistry **83**(14), 5570–5577 (2011).

[53] C. K. Kim, J. I. Rhee, and O. J. Sohn, Proceedings of SPIE **7908**(1), 79080W–79080W–10 (2011).

[54] S. C. Hong, H. Chen, J. Lee, H. K. Park, Y. S. Kim, H. C. Shin, C. M. Kim, T. J. Park, S. J. Lee, K. Koh, H. J. Kim, C. L. Chang, and J. Lee, Sensors and Actuators B: Chemical **156**(1), 271–275 (2011).

[55] F. Kheiri, R. E. Sabzi, E. Jannatdoust, E. Shojaeefar, and H. Sedghi, Biosensors and Bioelectronics **26**(11), 4457–4463 (2011).

[56] L. Campanella, S. Eremin, D. Lelo, E. Martini, and M. Tomassetti, Sensors and Actuators B: Chemical **156**(1), 50–62 (2011).

[57] K. Liu, J. J. Zhang, C. Wang, and J. J. Zhu, Biosensors and Bioelectronics **26**(8), 3627–3632 (2011).

[58] Rajesh, V. Sharma, V. K. Tanwar, S. K. Mishra, and A. M. Biradar, Thin Solid Films **519**(3), 1167–1170 (2010).

[59] Y. W. Li, K. Xia, R. Z. Wang, J. H. Jiang, and L. T. Xiao, Analytical and Bioanalytical Chemistry(Preprints), 1–6 (2011).

[60] R. I. Stefan and R. G. Bokretsion, Journal of Immunoassay and Immunochemistry **24**(3), 319–324 (2003).

[61] S. Suwansa-ard, P. Kanatharana, P. Asawatreratanakul, B. Wongkittisuksa, C. Limsakul, and P. Thavarungkul, Biosensors and Bioelectronics **24**(12), 3436–3441 (2009).

[62] Y. C. Kwon, M. G. Kim, E. M. Kim, Y. B. Shin, S. K. Lee, S. Lee, M. J. Cho, and H. S. Ro, Biotechnology Letters **33**(5), 921–927 (2011).

[63] B. J. Yakes, J. Deeds, K. White, and S. L. DeGrasse, Journal of Agricultural and Food Chemistry **59**(3), 839–846 (2011).

[64] M. Frasconi, M. Mazzarino, F. BotrÃ¨, and F. Mazzei, Analytical and Bioanalytical Chemistry(Preprints), 1–9 (2011).

[65] T. M. P. Hewa, G. A. Tannock, D. E. Mainwaring, S. Harrison, and J. V. Fecondo, Journal of Virological Methods **162**(1-2), 14–21 (2009).

[66] S. Kurosawa, J. W. Park, H. Aizawa, S. I. Wakida, H. Tao, and K. Ishihara, Biosensors and Bioelectronics **22**(4), 473–481 (2006).

[67] S. L. Zeng, H. K. Zhou, N. Gan, and Y. T. Cao, Applied Mechanics and Materials **80**(1), 452–456 (2011).

[68] N. Kim, D. K. Kim, and Y. J. Cho, Sensors and Actuators B: Chemical **143**(1), 444–448 (2009).

[69] Y. S. Sohn and Y. T. Kim, Electronics Letters **44**(16), 955–956 (2008).

[70] M. H. F. Meyer, M. Hartmann, and M. Keusgen, Biosensors and Bioelectronics **21**(10), 1987–1990 (2006).

[71] P. M. H. Heegaard, H. G. Pedersen, A. L. Jensen, and U. Boas, Journal of Immunological Methods **343**(2), 112–118 (2009).

[72] S. W. Oh, J. D. Moon, S. Y. Park, H. J. Jang, J. H. Kim, K. B. Nahm, and E. Y. Choi, Clinica Chimica Acta **356**(1-2), 172–177 (2005).

[73] B. K. De, L. G. Smith, W. E. Owen, and W. L. Roberts, Clinica Chimica Acta **323**(1-2), 151–155 (2002).

[74] H. Y. Tsai, C. F. Hsu, I. W. Chiu, and C. B. Fuh, Analytical Chemistry **79**(21), 8416–8419 (2007).

[75] V. Vermeeren, L. Grieten, N. Vanden Bon, N. Bijnens, S. Wenmackers, S. D. Janssens, K. Haenen, P. Wagner, and L. Michiels, Sensors and Actuators B: Chemical **157**(1) (2011).

[76] L. C. L. Correia, J. C. Lima, G. Gerstenblith, L. P. Magalhaes, A. Moreira, O. Barbosa Jr., J. Dumet, L. C. S. Passos, A. D'Oliveira Junior, and J. P. Esteves, Arquivos Brasileiros de Cardiologia **81**, 133–136 (2003).

[77] E. G. Shafrin and W. A. Zisman, The Journal of Physical Chemistry **64**(5) (1960).

[78] Lakowicz, Principles of Fluorescence Spectroscopy (Plenum Press, New York, 1983).

[79] A. Jablonski, Z. Phys. **94**(38) (1935).

[80] J. R. Macdonald, Annals of Biomedical Engineering **20** (1992).

[81] B. Conings, L. Baeten, H. G. Boyen, D. Spoltore, J. D'Haen, L. Grieten, P. Wagner, M. K. Van Bael, and J. V. Manca, The Journal of Physical Chemistry C (2011).

[82] M. Naumowicz, A. D. Petelska, and Z. A. Figaszewski, Electrochimica Acta **54**(3) (2009).

[83] Y. V. Pleskov, A. Y. Sakharova, M. D. Krotova, L. L. Bouilov, and B. V. Spitsyn, Journal of Electroanalytical Chemistry **228**(1-2) (1987).

[84] A. Kraft, International Journal of Electrochemical Science **2**(5) (2007).

[85] M. C. Granger, J. Xu, J. W. Strojek, and G. M. Swain, Analytica Chimica Acta **397**(1-3) (1999).

[86] R. Hoffmann, A. Kriele, H. Obloh, J. Hees, M. Wolfer, W. Smirnov, N. Yang, and C. E. Nebel, Applied Physics Letters **97**(5), 052103–052103–3 (2010).

[87] S. D. Janssens, P. Pobedinskas, J. Vacik, V. Petrakova, B. Ruttens, J. D'Haen, M. Nesladek, K. Haenen, and P. Wagner, New Journal of Physics **13**(8), 083008 (2011).

[88] E. Mahe, D. Devilliers, and C. Comninellis, Electrochimica Acta **50**(11), 2263–2277 (2005).

[89] R. Ramesham, Sensors and Actuators B: Chemical **50**(2), 131–139 (1998).

[90] J. van de Lagemaat, D. Vanmaekelbergh, and J. J. Kelly, Journal of Electroanalytical Chemistry **475**(2), 139–151 (1999).

[91] M. C. Granger and G. M. Swain, Journal of The Electrochemical Society **146**(12), 4551–4558 (1999).

[92] M. C. Granger, M. Witek, J. Xu, J. Wang, M. Hupert, A. Hanks, M. D. Koppang, J. E. Butler, G. Lucazeau, M. Mermoux, J. W. Strojek, and G. M. Swain, Analytical Chemistry **72**(16), 3793–3804 (2000).

[93] H. Kuzmany, R. Pfeiffer, N. Salk, and B. GÃ¼nther, Carbon **42**(5-6), 911–917 (2004).

[94] A. J. S. Fernandes, M. A. Neto, F. A. Almeida, R. F. Silva, and F. M. Costa, Diamond and Related Materials **16**(4-7), 757–761.

[95] F. A.C. and R. J., Physical Review b **63**(12), 1214051–1214054 (2001).

[96] L. Ostrovskaya, V. Perevertailo, V. Ralchenko, A. Saveliev, and V. Zhuravlev, Diamond and Related Materials **16**(12), 2109–2113 (2007).

[97] J. J. Sakon, G. J. Ribeill, J. M. Garguilo, J. Perkins, K. R. Weninger, and R. J. Nemanich, Diamond and Related Materials **18**(1), 82–87 (2009).

[98] M. Naumowicz, A. D. Petelska, and Z. A. Figaszewski, Electrochemica Acta **54**(3), 1089–1094 (2009).

[99] B. Rezek, M. Kratka, A. Kromka, and M. Kalbacova, Biosensors and Bioelectronics **26**(4), 1307–1312 (2010).

[100] B. Rezek, L. Michalikova, E. Ukraintsev, A. Kromka, and M. Kalbacova, Sensors **9**(5), 3549–3562 (2009).

[101] B. Rezek, E. Ukraintsev, L. Michalikova, A. Kromka, J. Zemek, and M. Kalbacova, Diamond and Related Materials **18**(5-8), 918–922 (2009).

[102] R. Hoffmann, A. Kriele, S. Kopta, W. Smirnov, N. Yang, and C. Nebel, physica status solidi (a) **207**(9), 2073–2077 (2010).

[103] J. Niedziolka-Jonsson, S. Boland, R. LeechD.and Boukherroub., and S. Szunerits, Electrochimica Acta **55**(3), 959–964 (2010).

[104] V. Petrak, L. Grieten, A. Taylor, F. Fendrych, M. Ledvina, S. D. Janssens, M. Nesladek, K. Haenen, and P. Wagner, physica status solidi (a) pp. n/a–n/a (2011).

[105] L. Baeten, B. Conings, H. G. Boyen, J. D'Haen, A. Hardy, M. D'Olieslaeger, J. V. Manca, and M. K. Van Bael, Advanced Materials **23**(25) (2011).

[106] B. van Grinsven, N. V. Bon, L. Grieten, M. Murib, S. D. Janssens, K. Haenen, E. Schneider, S. Ingebrandt, M. J. Schoning, V. Vermeeren, M. Ameloot, L. Michiels, R. Thoelen, W. De Ceuninck, and P. Wagner, Lab on a Chip **11**(9) (2011).

Publications and conference contributions

Publications

Publications in international journals with ‘peer-review’

1. N. Bijnens, V. Vermeeren, M. Daenen, **L.Grieten**, K. Haenen, S. Wenmackers, O.A. Williams, M. Ameloot, M. vandeVen, L. Michiels, P. Wagner, ’Synthetic diamond films as a platform material for label-free protein sensors’, Physica Status Solidi A 20/3, 520-526 (2009).

2. B. van Grinsven, N. Vanden Bon,**L.Grieten**, M. Murib, S.D. Janssens, K. Haenen, E. Schneider, S. Ingebrandt, M.J. Schoning, V. Vermeeren, M. Ameloot, L. Michiels, R. Thoelen, W. De Ceuninck, P. Wagner, ‘Rapid assessment of the stability of DNA duplexes by impedimetric real-time monitoring of chemically induced denaturation’, Lab on a Chip 11, 1656-1663 (2011).

3. V. Vermeeren, **L.Grieten**, N. Vanden Bon, N. Bijnens, S. Wenmackers, S.D. Janssens, K. Haenen, P. Wagner, L. Michiels, ‘Real-time impedimetric detection of C-Reactive Protein with a diamond-based immunosensor’, Sensors & Actuators B-Chemical In Press (2011).

4. B. Conings, L. Baeten, H-G. Boyen, D. Spoltore, J. D’Haen,**L.Grieten**, P. Wagner, M. van Bael, J. Manca, ’Influence of interface morphology

on the photovoltaic properties of nanopatterned ZnO/Poly(3-heylthiophene) Hybrid Cells. An impedance spectroscopy study', The Journal of Physical Chemistry C, In Press (2011)

5. D. Tran, V. Vermeeren, **L.Grieten**, S. Wenmackers, P. Wagner, J. Pollet, K. Janssen, L. Michiels, J. Lammertyn, 'Nanocrystalline diamond impedimetric aptasensor for the label-free detection of human IgE', Biosensors & Bioelectronics 26(6), 2987-2993 (2011)

6. B. van Grinsven, T. Vandenryt, S. Duchateau, A. Gaulke,**L.Grieten**, R. Thoelen, S. Ingebrandt, W. De Ceuninck, P. Wagner, Physica Status Solidi A 207 (2010).

7. **L.Grieten**, S.D. Janssens, A. Ethirajan, N. VandenBon, L. Michiels, K. Haenen, M. Ameloot, P. Wagner, Real-time study of protein adsorption on thin nanocrystalline diamond, Physica Status Solidi, Accepted (2011)

8. V. Petrak, **L.Grieten**, A. Taylor, F. Fendrych, M. Ledvina, S.D. Janssens, M. Nesladek, K. Haenen, P. Wagner, 'Monitoring of peptide induced disruption of artificial lipid membrane constructed on boron-doped nanocrystalline diamond by electrochemical impedance spectroscopy', Physica Status Solidi (A), (2011) DOI: 10.1002/pssa.201100036

Conference contributions

Abstracts of oral presentations

1. *S.Wenmackers*, V. Vermeeren, **L.Grieten**, S. Janssens, L. Michiels, K. Haenen, S.D. Pop, K. Hinrichs, N. Esser, P. Wagner, 'Covalent coupling of nucleic acids and antibodies to semiconductors: enabling techniques for label-free real-time biosensors', Prague Congress Centre, European and International Forum on Nanotechnology-EuroNanoForum 2009 'Nanotechnology for Sustainable Economy', Prague, Czech Re-

public, June 2-5, 2009.

2. Invited presentation: *S.Wenmackers*, V. Vermeeren, S.D. Pop, A. Riskin, R. Vansweevelt,**L.Grieten**, S.D. Janssens, A. Hardy, M.K. Van Bael, C. Cobet, N. Esser, M. Ameloot, L. Michiels, K. Haenen, P. Wagner, 'Biosensors on diamond, silicon and carbon-nanowalls', MRS 2009 Fall Meeting, Hynes Convention Center & Sheraton Boston Hotel, Boston, MA, USA, November 30-December 4, 2009.

3. **L.Grieten**, S.D. Janssens, N. Vanden Bon, J. Bex, B. van Grinsven, V. Vermeeren, W. De Ceuninck, K. Haenen, M. Ameloot, L. Michiels, P. Wagner, 'Coplanar diamond electrodes for the label-free detection of proteins', Engineering of Functional Interfaces 2010 (EnFI 2010), Philipps Universitat Marburg, Marburg, Germany, July 15-16, 2010.

4. V. Vermeeren,**L.Grieten**, N. Bijnens, S. Wenmackers, N. Vanden Bon, K. Haenen, P. Wagner, L. Michiels, 'Diamond-based Biosensors with an impedimetric and label-free read-out', Anaheim convention centre, Anaheim, Los Angeles, USA, 21-25 June 2010

5. *V.Petrak*, **L.Grieten**, A. Taylor, F. Fendrych, M. Ledvina, S.D. Janssens, M. Nesladek, K. Haenen, P. Wagner, 'Peptide induced disruption of artificial lipid membranes constructed on boron doped nanocrystalline diamond - in situ impedimetric study', SBDD XVI, 21-23 February 2011, Hasselt (Belgium)

6. **L.Grieten**, S.D. Janssens, N. Vanden Bon, K. Haenen, M. Ameloot, L. Michiels, P. Wagner, 'Do diamond an proteins like each other? A in-situ impedance study on protein adsorption., Engineering of Functional Interfaces 2011 (EnFI 2010), Johannes Keppler UniverstÃ¤t, Linz, Austria, July17-19, 2011.

Abstracts of poster presentations

1. E. Bongaers, **L.Grieten**, J. Alenus, P. Wagner, F. Troost, R.-J. Brummer, ’Development of a Biosensor for the Detection of Histamine and Tryptase’, Joint General Scientific Meeting of the Belgian Physical Society and Belgian Biophysical Society, 30 May 2007, Antwerpen (Belgium)

2. **L.Grieten**, V. Vermeeren, N. Bijnens, S. D. Janssens, K. Haenen, L. Michiels and P. Wagner, ’Impedimetric, diamond based immunosensors for the detection of C-Reactive Protein in physiological concentrations’, Belgian Physics Society General scientific meeting, 1th April 2009, Hasselt (Belgium)

3. **L.Grieten**, S.D. Janssens, N. Vanden Bon, J. Bex, V. Vermeeren, W. De Ceuninck, K. Haenen, M. Ameloot, L. Michiels and P. Wagner, ’Label-free detection of disease markers in human serum and development of miniaturized all-diamond electrodes’ Hasselt Diamond Workshop (SBDD XV), 22-24 February 2010, Hasselt (Belgium)

4. H. Yin, L. Shan, S. Wenmackers, **L.Grieten**, V. Vermeeren, M. Ameloot, L. Michiels, M . D’Olieslaeger, P. Wagner, H.-G Boyen, ’Cubic boron nitride thin films as a new platform for biosensor applications’, Hasselt Diamond Workshop (SBDD XV), 22-24 February 2010, Hasselt (Belgium)

5. **L.Grieten**, V. Vermeeren, N. Bijnens, S. D. Janssens, K. Haenen, L. Michiels and P. Wagner, ’Impedimetric, diamond based immunosensors for the detection of C-Reactive Protein in physiological concentrations’, Belgian Physics Society, General scientific meeting, 1th April 2010, Utrecht (Netherlands)

6. **L.Grieten**, N. Vandenbon, V. Vermeeren, N. Bijnens, S. D. Janssens, K. Haenen, L. Michiels and P. Wagner, ’Label-free and real time detection of CRP with a NCD based impedimetric sensor’, World Congres of

Biosensors 2010, 22-24 may 2010, Glasgow (United Kingdom)

7. **L.Grieten**, S.D. Janssens, N. Vanden Bon, J. Bex, B. van Grinsven, V. Vermeeren, W. De Ceuninck, K. Haenen, M. Ameloot, L. Michiels, P. Wagner, ‘Coplanar diamond electrodes for the label-free detection of proteins’, Engineering of Functional Interfaces 2010 (EnFI 2010), Philipps Universitat Marburg, July 15-16 2010, Marburg (Germany)

8. V. Petrak, **L.Grieten**, M. Nesladek, K. Haenen, A.Taylor, F. Fendrych, M. Hof, M. Ledvina, P. Wagner, ’Formation and biosensing properties of supported lipid bilayer on boron doped nanocrystalline diamond films’ 21st European Conference on Diamond, Diamond-like Materials, 5-9 September 2010, Budapest (Hungary)

9. V. Petrak, **L.Grieten**, A. Taylor, F. Fendrych, M. Ledvina, P. Wagner, M. Nesladek, ’Detection of Mellitin induced disruptions of supported lipid bilayers on boron doped nanocrystalline diamond films’, MRS Fall meeting, 29 November - 2 December 2010, Boston, Massachusetts (USA)

10. **L.Grieten**, S.D. Janssens, M. Saitner, B. Conings, R. Thoelen, H. G. Boyen, K. Haenen, P. Wagner, ’Probing the electrochemical properties in function of grain-sizes in diamond films’, (SBDD XVI), 20-23 February 2011, Hasselt (Belgium)

11. **L.Grieten**, S. D. Janssens, V. Vermeeren, N. Vanden Bon, W. De Ceuninck, M. Ameloot, K. Haenen, L. Michiels, P. Wagner, ‘Immunosensing based on patterned B-doped NCD electrodes’, MRS Spring Meeting, San Francisco, 2011.

12. **L.Grieten**, S. D. Janssens, T. Vandenryt, N. Vanden Bon, V. Vermeeren, K. Haenen, M. Ameloot, L. Michiels, P. Wagner, ‘Do diamond an proteins like each other?’, Biomedica 2011, Eindhoven (Netherlands), .

13. H. Yin, L. Shan, M. Saitner, **L.Grieten**, S. Wenmackers, V. Vermeeren, F. Wilbers, M. Ameloot, L. Michiels, M. D' Olieslaeger, P. Wagner, H.-G Boyen, 'Bio-functionlization of nanocrystalline cubic boron nitride thin films', Belgian Physics Society, General scientific meeting, April 2011, Namur (Belgium)

14. H. Yin, **L.Grieten**, A. Ethirajan, F. Wilbers, M. Ameloot, M. D'Olieslaeger, P. Wagner, H.-G. Boyen, 'Surface functionalization of nanocrystalline cubic boron nitride thin films'

15. M. Saitner, **L.Grieten**, S.D. Janssens, N. Vanden Bon, L. Michiels, H. Yin, J. D'Haen, K. Haenen, P. Wagner, M. D'Olieslaeger and H.-G. Boyen. 'Functionalization of CVD Diamond Films for Biosensor Applications - A photoemission study,

16. T. Vandenreyt, L. Grieten

17. T. Vandenreyt, L. Grieten

18. B. vanGrinsven,

List of Figures

List of Tables